Title

Making and Breaking a Bloch Wave Interferometer: High-order Sideband Polarimetry in Bulk Gallium Arsenide

Permalink

https://escholarship.org/uc/item/6pr7d7b9

Author

Costello, Joseph

Publication Date

2023

University of California
Santa Barbara

Making and Breaking a Bloch Wave Interferometer: High-order Sideband Polarimetry in Bulk Gallium Arsenide

A dissertation submitted in partial satisfaction
of the requirements for the degree

Doctor of Philosophy
in
Physics

by

Joseph Blair Costello

Committee in charge:

Professor Mark Sherwin, Chair
Professor Ania Bleszynski Jayich
Professor Matthew Fisher

June 2023

The Dissertation of Joseph Blair Costello is approved.

Professor Ania Bleszynski Jayich

Professor Matthew Fisher

Professor Mark Sherwin, Committee Chair

June 2023

Making and Breaking a Bloch Wave Interferometer: High-order Sideband Polarimetry
in Bulk Gallium Arsenide

by

Joseph Blair Costello

Acknowledgements

Having reached the end of this six year journey, it is fitting that I have no shortage of people to thank. Indeed any achievements that I have accomplished were only made possible by the support and collective action of others. To paraphrase Newton, if I have seen far it is because I stand on the shoulders of giants. I mean this both scientifically and emotionally. To complete a PhD is a difficult and arduous task in both senses.

In the modern field of physics, scientists specialize in ever more specific fields with progress characterized more by the slow but steady accumulation of knowledge than the great leaps forward of individual geniuses. This can make the day to day practice of science exhausting, and has sometimes led me to wonder if at the end of the day anyone is actually listening. But in another sense this mass production of science provides a fullfillment of its own. A refinement of Newton's sentiment for the modern day should be, if I have seen far it is because I stand on the shoulders of millions. So my first thanks goes to all scientists, who have joined me as comrades in this great effort to understand nature. I have drawn great solace from my place in this collective.

My second thanks goes out to the community of Santa Barbara, both in the university and more broadly. As I have matured, I have treasured developing my interests beyond the lab and the people of Santa Barbara have presented a welcoming community that I am proud to have been a part of. A scientist is still a person, and I would not have had the fortitude to finish this work if I did not feel a part of this community.

Of course, many more specific thanks are in order. I would like to thank my advisor Mark Sherwin for his unwavering support. He took me under his wing as a 21 year old kid with little in the way of practical skills and supported me intellectually and financially at every step along the way. He always made me feel like he cared about me, as a scientist and a person. I have never felt more excited about science than after our sideband meetings, even if they stretched for more than two hours. Many thanks as well to my lab partner Seamus O'Hara, who has been my brother in optics at every step along the way. Seamus' dedication, discipline, and belief in our abilities has been an invaluable asset while wrangling the FEL, dealing with computer communication problems, and muddling through confusing data. We have very nearly spent every day of our PhD's working together from introductory classes to thesis defences, and I am honored to have done this side by side with Seamus. I would like to thank our theory collaborator Qile Wu for his incredibly impressive work in untangling the knot of sideband generation. His success in developing concrete predictions from our data is, in my opinion, the most impressive piece of work I have been involved in. I would like to thank Darren Valovcin for introducing Seamus and I to sideband generation. His code and experimental appartus remain key parts of our experiments, and everything I've learned is due to his mentorship. Special thanks for teaching me how to tune the FEL. Thank you to Moonsuk Jang for helping with experiments, and for being a dedicated pupil. The future of sidebands is bright with Moon.

I would like to thank all the other members of the Sherwin group that I have had the good fortune to share a workplace with. Lab has been a welcoming place, full of friendships, companionship, and good coffee. Thanks to Blake Wilson and Changyun Yoo for welcoming me to the group, showing me the ropes and being wonderful role models as grad students. Thanks to Marzieh, Cocoa, and Tonda for all the fun in lab and all the adventures outside of it. Thanks to Nick, Dave, and Jerry for keeping the FEL in working order and all the other pieces of wisdom you've imparted to me. Thanks to Cameron, Alex, Courtney, and Audri for being great undergrads that were eager to learn. And of course, thanks to Brad Price and Mathilde Papillon for the great friends you have been and the countless hours we have spent together in various types of nonsense.

I am lucky to have a wonderful set of supportive friends in this department without whom I would not have had a chance of achieving anything as a graduate student. Thanks to Aleksei Khindanov and Sergio Hernandez-Cuenca for being dream roommates, even in a tiny termite infested apartment. Long live 7-11. Thanks to Zhitao/Tom Chen for being a great first year office mate and even better friend and gym partner. Thanks to Yaodong for your unwavering friendship, biting wit, and in general being the guy. Thanks to Noah Swimmer, Sarah Steiger, Josh Straub, and Will Schultz for the board game nights, camping trips, thought provoking conversations, home brew, and great vibes. Thanks to Aaron Kennon for tea time, creative conversation, joy, and impeccable fashion sense. Thanks to Molly Kaplan and Megan Newsome for movie nights, wine drinking, and dog adventures. Thanks to Molly Wolfson for coffee time and spirited movie debates.

For all the friends outside of the Physics department, I would like to thank you for bringing variety and color to my life. Thank you to Demi, Katie O., Anet, Alex M., Iman, Linda, and Ethan for trivia, drinks, food, sports, and irreplaceable companionship. Thanks to Olivia for the music shows and baseball talk. Thank you to Rob, Griffin, Amy, Uma, Caela, Eddie, Mars, Isabella, Alex, Cody, and Jackson for being inspirations and giving me hope that the future can be a better place if we work for it. Thanks to Danny, Chris, Ramsey, Mac, and Rachael for being such wonderful friends even after years spent apart and for the New Years celebrations.

Thank you to my family, for being the ultimate bedrock upon which I can always lean back on for support. I want to thank my grandparents for being the foundations upon which the family is based, especially my Grandpa Greene for nurturing my love of science from the day I was born. Special thanks to my brother Dan for our farmers market lunches. I am so lucky to have had this opportunity to grow close with my brother as an adult 400 miles from home. Even more special thanks are due to my parents, who have made me who I am today.

Finally a heartfelt thanks to Kailey who has supported me through the writing of this dissertation, and who has been a vital fountain of care.

Curriculum Vitæ

Joseph Blair Costello

Education

2023	Ph.D. in Physics, University of California, Santa Barbara.
2020	M.A. in Physics, University of California, Santa Barbara.
2017	B.A. in Physics, University of California, Berkeley.
2013	Ponderosa High School, Shingle Springs, California.

Publications

"Experimental Reconstruction of Bloch wavefunctions of holes in a semiconductor", J.B. Costello, S.D. O'Hara. Q. Wu, D.C. Valovcin, L.N. Pfeiffer, K.W. West, and M.S. Sherwin. *Nature* **599**, 57-61 (2021)

"Visualization and Control of Single-Electron Charging in Bilayer Graphene Quantum Dots", Jair Velasco Jr, Juwon Lee, Dillon Wong, Salman Kahn, Hsin-Zon Tsai, Joseph Costello, Torben Umeda, Takashi Taniguchi, Kenji Watanabe, Alex Zettl, Feng Wang, and Micahel F Crommie. *Nano Lett.* **18, 8,** 5104-5110 (2018)

Abstract

Making and Breaking a Bloch Wave Interferometer: High-order Sideband Polarimetry
in Bulk Gallium Arsenide

by

Joseph Blair Costello

For centuries, the understanding of waves has gone hand in hand with the development of interferometry, the study of interference. Interference occurs when multiple waves are combined which can result in enhancement or destruction of wave intensity. The patterns produced by interference can contain information about the wave which is otherwise difficult to measure.

In the solid state, many properties are explained by considering the wavefunctions of electrons in periodic crystals, called Bloch wavefunctions. However, interferometry experiments in driven condensed matter systems are difficult due to the large amount of interactions in real materials that cause dephasing on sub-picosecond timescales.

This work develops polarimetry of high-order sidebands as a promising method that measures the interference of electron-hole pairs in materials. These sidebands are created through high-order sideband generation (HSG) where a weak near-infrared laser (NIR) and a strong terahertz (THz) laser are coincident on a semiconductor. The NIR excites electron-hole pairs that are accelerated by the THz. When the electrons and holes collide, they annihilate and release light at a higher energy, called a sideband. Multiple types of electron-hole pair can contribute to the sideband, resulting in an interference that is caused by the accumulation of phases during acceleration and imprinted on the polarization of the sideband.

In gallium arsenide we have extracted information about Bloch waves from sideband polarimetry. By studying the dependence of polarization on crystal angle, we measure Hamiltonian parameters and reconstruct the Bloch waves that take part in HSG.

Here we also study the effect of dephasing on HSG, especially with regards to temperature dependence. We report polarimetry experiments that are robust to increases of temperature up to 200 K, and from this data we are able to extract the dephasing coefficients associated with phonon interactions for different Bloch waves.

Current experiments have focused on understanding the role of the dynamical phase in sideband polarimetry, but we discuss how strain can introduce geometric phases in gallium arsenide and how this could be probed in future experiments.

Sideband polarimetry has been developed as a Bloch wave interferometer in gallium arsenide, but this method could be applied to many semiconductors to access a wide range of wavefunction phases in materials.

Contents

Chapter 1

Introduction

In the opening years of the nineteenth century, Thomas Young demonstrated that darkness could be produced by a combination of two light rays. This property, called interference, was used by Young to argue in favor of the wave theory of light. Debates over the nature of light, particle or wave, had been ongoing since the seventeenth century. Huyghens had proposed that light was propagated via longitudinal waves, but this theory was opposed by Newton who argued in favor of light as a particle. Young's theory was not immediately accepted, and it was not until Fresnel's improved treatment of interference and diffraction in 1818 that the wave nature of light began to be generally accepted. This insight was key to the development of electromagnetic theory, and represents the birth of interferometry [1].

A century later in 1905, Einstein revisited the controversy by proposing that light could be divided into a quantized number of photons that simultaneously possessed wave and corpuscular properties. Louis de Broglie was inspired by this theory to generalize the concept to all particles, including matter, in 1924 [2, 3]. This theory of matter waves provided one of the most startling predictions of the emerging field of quantum mechanics; that all matter possessed wave properties. Experiments by Thomson and

Reid in 1927 and Davisson and Germer in 1928 reported the diffraction of matter in the form of electrons [4, 5]. These results demonstrated the interference of electrons with themselves, proving the wave nature of the electron and strengthening the evidence for quantum mechanics.

The rest of the twentieth century saw the immense success of quantum mechanics, and the first quantum theories of condensed matter. The foundations of the field were laid by Felix Bloch in 1929, when he specified the form of wavefunctions in periodic systems like crystalline matter. Interferometry advanced along with condensed matter physics, and interference has been observed in a variety of solid state systems. Such systems include metal surfaces [6, 7, 8, 9], chiral edge states of quantum wells [10], and materials driven by intense lasers [11, 12, 13, 14, 15].

As technology has advanced there has been a great deal of interest in taking advantage of the wave nature of quasiparticles in materials. To build such a quantum device, it is necessary to have accurate knowledge of the form and coherence of the relevant wavefunction as well as experimental access to the phases of these wavefunctions. Interferometry in these systems provides an answer to all of these concerns, but performing interferometry in the solid state remains difficult despite significant progress in some systems.

This dissertation details the development of high-order sideband polarimetry as a method of Bloch wavefunction interferometry in gallium arsenide (GaAs). Chapter two shows how Bloch wavefunction interference can be measured through probing the polarization of light created by a method called high-order sideband generation. Chapter three explores the temperature dependence of sideband polarimetry as a probe of the coherence of this interference process. Chapter four describes how strain influences sideband polarimetry and proposes future experiments that could extract interesting information from highly strained GaAs samples. This chapter will provide basic introductions interferometry, both in general and specifically applied to condensed matter systems. It will also discuss the physics of GaAs, the material studied by the experiments discussed here.

1.1 Principles of Interferometry and Classical Waves

Waves are a class of phenomena that propagate through time and space according to the wave equation,

$$\frac{\partial^2}{\partial t^2}\psi(\boldsymbol{x},t) = c^2\nabla^2\psi(\boldsymbol{x},t) \tag{1.1}$$

where c is a constant and ψ is the wave defined in time t and space $\boldsymbol{x}$. There are many different functions that satisfy this equation, but it is helpful to focus on a simple set of functions called plane waves. Plane waves describe waves that propagate in one direction, extend infinitely in the plane perpendicular to the direction of propagation, and are constant in directions other than the direction of propagation. Mathematically this can be expressed as,

$$\psi(\boldsymbol{x},t) = Ae^{i(kz-\omega t+\phi_0)} \tag{1.2}$$

where k is the wavenumber, or spatial frequency, z is the direction of propagation, ω is the temporal frequency, A is the magnitude, and ϕ_0 is the initial phase of the wave which can vary 0 to 2π. It is straightforward to confirm that Eq. 1.2 satisfies Eq. 1.1. The use of a complex exponential simplifies algebra, and can be used even for waves that describe purely real phenomena as long as one takes only the real component at the end of a given calculation.

1.1.1 Interference of Light

A key result from electromagnetism is that light is an electromagnetic wave. That is to say, light propagates as electric and magnetic fields that satisfy the wave equation.

In this case, c from Eq. 1.1 is the speed of light and relates k and ω by the equation $\omega = c/k$. In this work I will focus on the electric field. In practice, electromagnetic plane waves are not physical since light beams are not infinite and have multiple frequencies. However, as long as the extent of the beam is much larger than the wavelength and the frequency distribution is small, it is usually sufficient to approximate light as plane waves. Mathematically we can express the electric field as a plane wave,

$$E(\boldsymbol{x}, t) = E_0 e^{i(kz - \omega t + \phi_0)}. \tag{1.3}$$

Electric fields add linearly, so if we imagine two sources of light called 1 and 2 that are coincident at the same point $\boldsymbol{x}_0$ then the total electric field will be,

$$E_{tot}(\boldsymbol{x}_0, t) = E_1(\boldsymbol{x}_0, t) + E_2(\boldsymbol{x}_0, t) \tag{1.4}$$

where E_{tot} is the total electric field, and E_1 and E_2 is the electric field of source 1 and 2 respectively. Let us imagine a simple case where both sources have the same amplitude E_0 and frequency ω. This implies they have the same k as well. We further restrict our focus to a single point in time and space, such that the beams are identical except for an overall phase factor φ, which contains all the phase parameters. In this case, the total electric field is

$$E_{tot} = E_0(1 + e^{i\varphi}). \tag{1.5}$$

Here we have chosen to work with phases such that at this point E_1 has no phase. The overall phase of the electric field is arbitrary in these calculations. If we were to look at this point, however, the brightness we would see is not arbitrary. This is because what we see is the intensity of light, not the direct field. The intensity is related to the magnitude squared of the field,

$$|E_{tot}|^2 = E_{tot}E_{tot}^* = E_0^2(2 + 2\cos\varphi). \tag{1.6}$$

Fig. 1.1 shows three different examples of interference, showing E_1, E_2 and E_{tot} for three different values of φ. We see that in the case of $\varphi = 0$, the fields are in phase, and act as one field with magnitude $2E_0$ and intensity $4E_0^2$. This is called constructive interference, and is shown in the top row of Fig. 1.1. In the case of $\varphi = \pm\pi$, the fields are totally out of phase and it appears that there is no field and thus no intensity. The point looks dark. This is called destructive interference and is demonstrated in the middle row of Fig. 1.1. Intermediate values of φ provide intermediate interference, as shown by the bottom row of Fig. 1.1. The magnitude of E_{tot} smoothly increases or decreases with φ so measuring the total intensity gives information about the specific φ. Since the dependence on φ is periodic, constructive interference will occur when $\varphi = 2n\pi$ and destructive interference will occur when $\varphi = (2n + 1)\pi$, where n is an integer.

In principle the phase difference φ can come a variety of sources. A famous example is given by Young's interference experiment. We will consider the simplest version of this experiment, where we have two identical monochromatic point sources that radiate in phase, but are separated by some distance. Suppose that a screen is placed relatively far away from the slits and we view the intensity on the screen that is at some point d on the screen. Let r_1 be the distance from source 1 and d, and r_2 the distance from source 2 and d. We define $r = r_2 - r_1$, the difference in path length between the sources. In this case, $\varphi = kr$. k is related to the wavelength as $k = 2/pi/\lambda$, so the total phase difference between the sources is

$$\varphi = 2\pi\frac{r}{\lambda} \tag{1.7}$$

which leads to constructive interference at $r = n\lambda$ and destructive interference at $r = (n + 1/2)\lambda$. Fig. 1.2 schematically shows how different spots on the screen experience

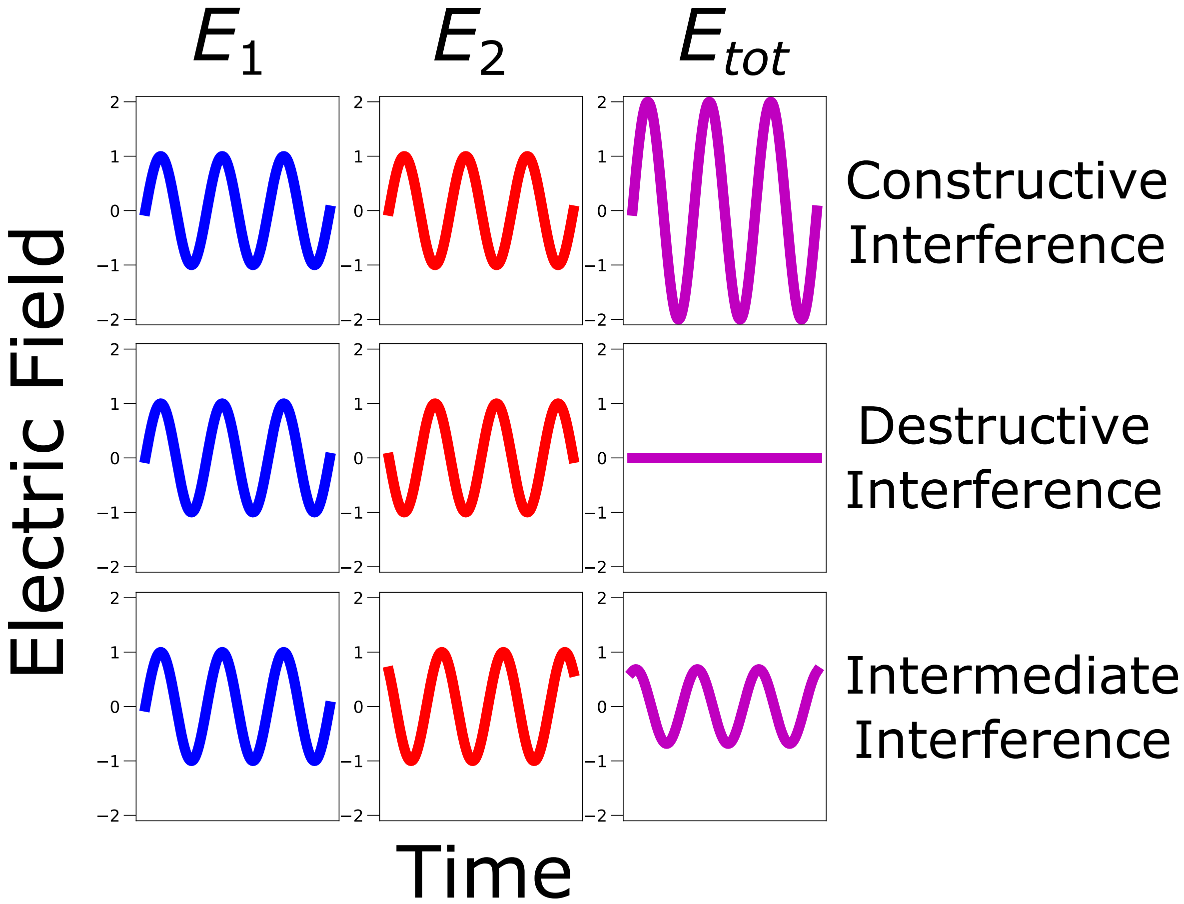

Figure 1.1: **Interference of Electric Fields.** Three examples of the interference of electric fields. The electric field from source 1 (E_1, left, blue) interferes with the electric field from source 2 (E_2, center, red) resulting in the wave E_{tot} (right, purple). Constructive interference (top) occurs when E_1 and E_2 are totally in phase ($\varphi = 0$) and results in a field with a larger amplitude. Destructive interference (middle) occurs when E_1 and E_2 are totally out of phase ($\varphi = \pm\pi$) and results in no field at all. To the observer this appears as a dark spot. If φ is at an intermediate value, then the interference produces a wave of intermediate amplitude. The bottom row demonstrates the interference when $\varphi = 140°$.

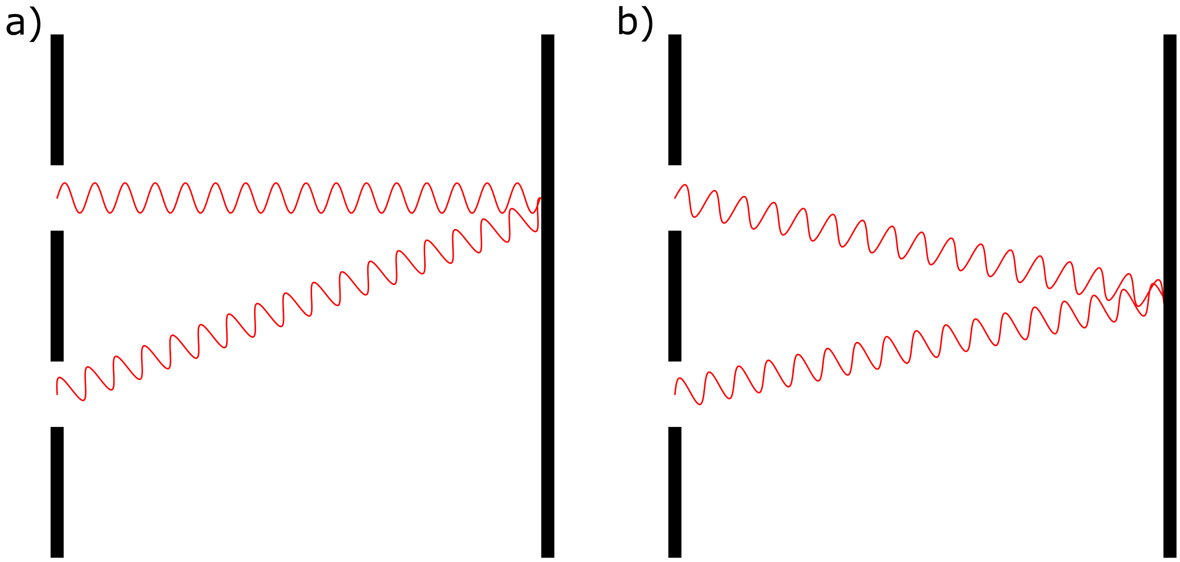

Figure 1.2: **Young's two slit interference.** Two examples of interference resulting from coherent light incident on two slits. **a)** (left) and **b)** (right) show interference at two different locations on the viewing screen. As the path difference r changes the interference will change, leading to spots of constructive and destructive interference. This appears to the observer as a series of bright spots, where $r = n\lambda$, alternating with dark ones, where $r = (n + 1/2)\lambda$.

different interference. As we move up and down the screen, the relative distance between the two sources changes, which leads to a series of light spots where the sources constructively interfere and dark spots destructively interfere. If the sources are rectangular, the interference pattern becomes a series of bars.

This process is called two slit interference, but interference can also occur from one source. We imagine a plane wave incident on a slit of length b. For sufficiently small values of b, the slit acts as an extended source of the light, with each point along the slit acting as a point source. These sources all interfere with each other, which gives rise to an interference pattern sensitive to the wavelength of light. Diffraction patterns also occur due to networks of openings, called diffraction gratings, which are used to separate different wavelengths of light.

Interferometry with light can be extremely sensitive since changes on the order of the wavelength of light can cause phase accumulation sufficient to change intensity peaks to troughs or vice-versa. A common application of this sensitivity is the Michelson interferometer. This device consists of a source incident on a beam splitter, which transmits half of the beam and reflects the other half. The reflected half travels a distance r_1 to a mirror, while the transmitted half travels a distance r_2 to another mirror. The reflected beams travel back to the beam splitter where they combine and are detected. If $r = r_2 - r_1$ then the total path difference is $2r$, causing constructive interference at $r = n(\lambda/2)$ and destructive interference at $r = \lambda/2(n + 1/2)$. By carefully moving the second mirror, r_2 can be slightly changed, and the interference can be carefully detected. Michelson interferometers are capable of making extremely sensitive measurements of quantities like strain or the isotropy of the speed of light. Such measurements are accurate to within 1 part in 10^{-21} in the most exact cases [16, 17].

For additional discussions on the development and fundamentals of interferometry, see Hariharan's *Optical Interferometry* [1].

1.1.2 Polarization of Light

Interfering light can be extremely useful, but not all light will interfere in the way we have just discussed. This is due to a property called polarization, which we will now develop. Electric fields are three dimensional vectors. Light is a transverse wave, which is to say that the z component of both the electric and magnetic fields are zero. This leaves 2 directions for the electric field to oscillate in. The direction that the electric field oscillates is called the polarization of light, and can be represented by a 2 dimensional vector. The electric field can then be represented as

$$\boldsymbol{E} = E_0 \begin{pmatrix} E_x \\ E_y \end{pmatrix} e^{i(kz-\omega t+\phi_0)} \tag{1.8}$$

where E_x is the component of the electric field in the x direction, and E_y is the component in the y direction. In the case where the polarization vector is normalized, E_0 is the magnitude of the electric field. Because the electric field is a real quantity, it is necessary to take the real component of Eq. 1.8 to get the physical electric field. In the case that $E_x = 1$ and $E_y = 0$, this is called horizontal polarization. Assuming $\phi_0 = 0$, the physical electric field will oscillate in time as $\cos(\omega t)$, but the field will always point along the x, or horizontal, direction. If $E_x = 0$ and $E_y = 1$, the polarization is called vertical for similar reasons. In the case where neither E_x nor E_y is zero the polarization will lie on a straight line in the $x - y$ plane. As an example, consider the case where $E_x = E_y$. In this case the polarization will lie along a diagonal line 45° between the x and y axes.

With one angle we are able to describe every polarization where the x and y components of the electric field oscillate together. However, it is possible for these components to oscillate out of phase. In this case Eq. 1.8 becomes

$$\boldsymbol{E} = E_0 \begin{pmatrix} \tilde{E}_x \\ \tilde{E}_y \end{pmatrix} = E_0 \begin{pmatrix} E_x \\ E_y e^{i\delta} \end{pmatrix} e^{i(kz-\omega t+\phi_0)} \tag{1.9}$$

where δ is the phase delay between the x and y components and $\tilde{E}_{x(y)}$ is the time dependent electric field in the $x(y)$ direction. When $\delta \neq 0$, the maxima of the x and y components will occur at different times. Physically this manifests as the electric field rotating in the $x - y$ plane. This is mathematically represented by the complex phase δ, which changes the time that the real part of the y component is maximized. In the case where $\delta = \pm\pi/2$, the phase factor is $\pm i$ and the x and y components are maximally out of phase. If this is true and $|E_x| = |E_y|$, then the electric field vector will rotate along a circle in the $x - y$ plane. This polarization state is called circular polarization and can be right handed or left handed depending on the sign of $e^{i\delta}$. If δ is not 0, $\pi/2$, or $-\pi/2$, then the electric field vector will trace out an ellipse in the $x - y$ plane. This set of polarization states is called elliptical polarization. It is impossible to describe either circular or elliptical polarization only with one parameter.

To fully describe the polarization state, we consider the time dependence of the real parts of Eq. 1.9, which gives

$$\begin{aligned} \tilde{E_x} &= E_x \cos(\omega t) \\ \tilde{E_y} &= E_y(\cos(\omega t)\cos(\delta) - \sin(\omega t)\sin(\delta)). \end{aligned} \tag{1.10}$$

We can square and combine the equations to remove the time dependent terms to get

$$\sin^2(\delta) = \left(\frac{\tilde{E_x}}{E_x}\right)^2 + \left(\frac{\tilde{E_y}}{E_y}\right)^2 - 2\cos(\delta)\frac{\tilde{E_x}\tilde{E_y}}{E_x E_y}. \tag{1.11}$$

This equation is that of a rotated ellipse for $\tilde{E_x}$ and $\tilde{E_y}$, where all other values are constants that describe the polarization state. At any time, $\tilde{E_x}$ and $\tilde{E_y}$ must satisfy Eq. 1.11 and lie on the ellipse it describes. Since the $\cos(\delta)$ term tilts the ellipse, it is useful to introduce a new coordinate system which has principal axes aligned with the semi-major and semi-minor axes of the ellipse. This new coordinate system is rotated by an angle α, called the orientation angle. They are related to the old coordinates by

$$\begin{aligned} E'_x &= \cos(\alpha)\tilde{E_x} + \sin(\alpha)\tilde{E_y} \\ E'_y &= -\sin(\alpha)\tilde{E_x} + \cos(\alpha)\tilde{E_y}. \end{aligned} \tag{1.12}$$

Where $E'_{x(y)}$ are the time dependent components of the polarization vector in the new coordinate system. In this coordinate system, the polarization vector now lies on a standard ellipse at all times. We can parameterize the ellipse as

$$\begin{aligned} E'_x &= a\left(\cos(\omega t)\cos(\phi) - \sin(\omega t)\sin(\phi)\right) \\ E'_y &= b\left(\sin(\omega t)\cos(\phi) + \cos(\omega t)\sin(\phi)\right) \end{aligned} \tag{1.13}$$

where a is half of the ellipse width, b is half the ellipse height, and ϕ is an arbitrary parameter to parameterize the ellipse. Through algebraic manipulation of Eq. 1.10, Eq. 1.12, and Eq. 1.13, we can eliminate the time dependent parameters, and relate the elliptical parameters to the constants E_x, E_y, and δ which define the original polarization vector. Careful manipulation gives,

$$\begin{aligned} a\cos(\phi) &= E_x\cos(\alpha) + E_y\sin(\alpha)\cos(\delta) \\ a\sin(\phi) &= E_y\sin(\alpha)\sin(\delta) \\ b\sin(\phi) &= -E_x\sin(\alpha) + E_y\cos(\alpha)\cos(\delta) \\ b\cos(\phi) &= -E_y\cos(\alpha)\sin(\delta). \end{aligned} \tag{1.14}$$

From these equations, we can isolate the orientation angle α in terms of the original polarization parameters,

$$\tan(2\alpha) = 2\cos(\delta)\frac{E_xE_y}{E_x^2 - E_y^2}. \tag{1.15}$$

We define α such that $-90° < \alpha \leq 90°$. Because the electric field will oscillate over negative and positive directions, α is periodic over 180°. This means that $\alpha = -90°$ is equivalent to $\alpha = 90°$. Along with α, it is useful to have a parameter which measures how elliptical the polarization state is. For this purpose we introduce the ellipticity angle, γ

defined as

$$\tan(\gamma) = \frac{-b}{a}. \tag{1.16}$$

The minus sign sets which handedness of light corresponds to positive versus negative γ. Here, positive γ corresponds to right handed light. Geometrically, γ is the angle between the semi-major axis and the semi-minor axis, which is clear from the definition of Eq. 1.16. By construction $b \leq a$, which limits the domain of γ to $-45^\circ \leq \gamma \leq 45^\circ$. We can use Eq. 1.14 to write γ in terms of the original polarization parameters, and through some careful algebra get the result

$$\sin(2\gamma) = 2\frac{E_x E_y \sin(\delta)}{E_x^2 + E_y^2} \tag{1.17}$$

With α and γ it is possible to describe any monochromatic and fully polarized state. It is advantageous to use α and γ because they provide an intuitive, geometrical sense of the electric field polarization. An alternative way to write the polarization vector using these parameters is

$$\boldsymbol{E} = E_0 \begin{pmatrix} E_x \\ E_y e^{i\delta} \end{pmatrix} = E_0 \begin{pmatrix} \cos\alpha & -\sin\alpha \\ \sin\alpha & \cos\alpha \end{pmatrix} \begin{pmatrix} \cos\gamma \\ i\sin\gamma \end{pmatrix}. \tag{1.18}$$

Fig 1.3 shows the geometric definitions of α and γ defined in relation to the E_x direction. Four examples of different polarization states with the appropriate α and γ angles are shown in Fig. 1.4. The polarization states shown are horizontal ($\alpha = 0^\circ$, $\gamma = 0^\circ$), diagonal ($\alpha = 45^\circ$, $\gamma = 0^\circ$), elliptical ($\alpha = -64^\circ$, $\gamma = 17^\circ$), and circular (α undefined, $\gamma = 45^\circ$).

There are, however, downsides to both the $\alpha,\ \gamma$ description of polarization and the $E_x,\ E_y,\ \delta$ description. Both are primarily descriptions of the electric field itself, which

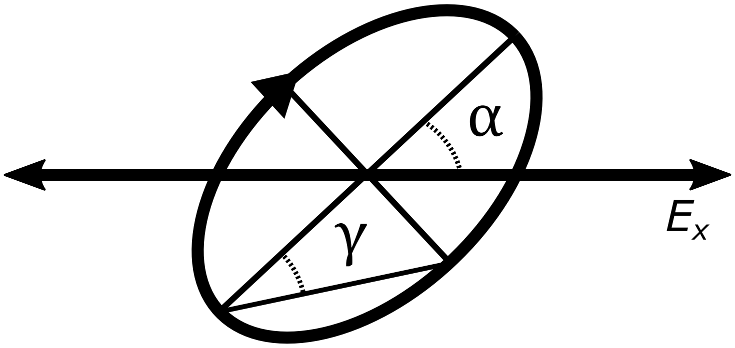

Figure 1.3: **The polarization ellipse.** The ellipse that can be used to describe any fully polarized state of light. The orientation angle α describes the angle between the semimajor axis of the ellipse and the x direction. The domain of α is $-90° < \alpha \leq 90°$, where $\alpha = 90°$ is equivalent to $\alpha = -90°$. The ellipticity angle γ is the angle between the semimajor and semiminor axes of the ellipse. The domain of γ is $-45° \leq \gamma \leq 45°$, with $\gamma = -45°$ corresponding to left handed circularly polarized light and $\gamma = 45°$ corresponding to right handed circularly polarized light. If $\gamma = 0°$ then the polarization state is linear and the ellipse is a line.

is extremely difficult to measure directly. Even with direct measurements of the field, it would be difficult to observe the polarization ellipse described by α and γ since the field oscillates at such a high frequency. For example, infrared light roughly oscillates 10^{14} times per second. Finally, neither formalism is well suited to describe unpolarized or partially polarized light.

In practice, most measurements of light in the laboratory measure intensities, which scales as the square of the field. Furthermore, since the time scale of oscillation is so fast, most measurements should be understood as a time average measurement. If we apply a time average to Eq. 1.11 we get,

$$\sin^2(\delta) = \frac{\left\langle {\tilde{E}_x}^2(t) \right\rangle}{E_x^2} + \frac{\left\langle {\tilde{E}_y}^2(t) \right\rangle}{E_y^2} - 2\cos(\delta)\frac{\left\langle \tilde{E}_x \tilde{E}_y \right\rangle}{E_x E_y} \tag{1.19}$$

where angle brackets denote time average. The time averages can be calculated as integrals using the explicit time dependence in Eq. 1.10. Plugging this into Eq. 1.19 and

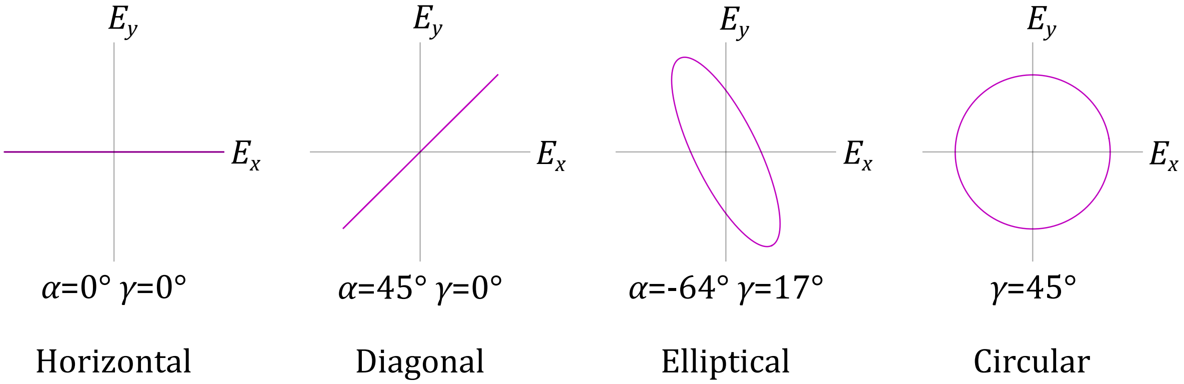

Figure 1.4: **Polarization states**. Four polarization states, with the corresponding α and γ angles. From left to right the states are horizontal, diagonal, elliptical, and circular. The purple lines represent the path in the $x-y$ plane that the electric field oscillates along. For linear polarizations like horizontal or diagonal, the path is a flat line. However, when the x and y components of the electric field oscillate out of phase, the polarization becomes elliptical. In the case where there are equal amounts of E_x and E_y and these components are 90° out of phase the polarization becomes a circle. For circular polarizations, α is undefined.

performing some algebraic manipulation yields,

$$\left(E_x^2+E_y^2\right)^2=\left(E_x^2-E_y^2\right)^2+\left(2E_xE_y\cos\delta\right)^2+\left(2E_xE_y\sin\delta\right)^2. \tag{1.20}$$

We call the four terms in this equation the Stokes parameters, specifically

$$\begin{aligned} S_0 &= E_x^2+E_y^2 \\ S_1 &= E_x^2-E_y^2 \\ S_2 &= 2E_xE_y\cos\delta \\ S_3 &= 2E_xE_y\sin\delta. \end{aligned} \tag{1.21}$$

These four parameters are real intensities of the electric field that are fairly straightforward to measure. S_0 is the magnitude of the polarization vector, and the overall intensity of the light in question. S_1 describes the amount of light polarzed in the horizontal or vertical linear directions. S_2 similarly is linked to the amount of light polarized linearly along the diagonal ($\alpha = 45°$) and anti-diagonal ($\alpha = -45°$) directions. S_3 is the amount of light polarized in the right hand circular and left hand circular directions. S_0 is a real, non-negative quantity and the other Stokes parameters are constrained as $-S_0 \leq S_i \leq S_0$ for $i = 1, 2, 3$. In fact, one can think of the Stokes parameters as the intensity of light along one basis direction minus the intensity of light in the orthogonal direction. Mathematically, this can be written as

$$\begin{aligned} S_1 &= E_H^2 - E_V^2 \\ S_2 &= E_D^2 - E_A^2 \\ S_3 &= E_R^2 - E_L^2 \end{aligned} \tag{1.22}$$

where H represents the intensity of light along the horizontal or x direction, V represents the intensity along the vertical (y) direction, D the intensity along the diagonal direction, A the intensity along the anti-diagonal direction, R the intensity of right handed light, and L the intensity of left handed light. If the light is polarized along one of these directions, say anti-diagonally, then the particular Stokes parameter will be equal to $\pm S_0$ (in this case $S_2 = -S_0$), and the other parameters will be equal to 0 (in this case $S_1 = S_3 = 0$). These interpretations of the Stokes parameters are very closely linked to experimental observables. E_H^2 can be measured as the intensity of light after a horizontal polarizer for example and the other terms of Eq. 1.22 can be measured by similar means.

It is straightforward to write α and γ in terms of the Stokes parameters by comparing Eq. 1.15 and 1.17 with Eq. 1.21. This yields,

$$\begin{aligned} \tan(2\alpha) &= \frac{S_2}{S_1} \\ \sin(2\gamma) &= \frac{S_3}{S_0}. \end{aligned} \tag{1.23}$$

Intuitively, α is related to the orientation of light in the $x-y$ plane and γ is related to the ellipticity of the light.

It is worth mentioning that the α, γ formalism has 2 free parameters. In comparison, the original polarization parameters (E_x, E_y, δ) has three free parameters. This is because the α, γ description has no sense of intensity, only polarization. If we constrain the original polarization parameters to be normalized then there are two degrees of freedom. In contrast to both of these descriptions, there are four Stokes parameters. This is due to the fact that the Stokes description is capable of describing light that is not perfectly polarized. One can see that following Eq. 1.21,

$$S_0^2 = S_1^2 + S_2^2 + S_3^2. \tag{1.24}$$

In the case of light that is not polarized, the total intensity S_0 will be greater than the intensity of the polarized portions represented by S_1, S_2, and S_3. Therefore,

$$S_0^2 \geq S_1^2 + S_2^2 + S_3^2. \tag{1.25}$$

We can define a parameter called the degree of polarization, P. It is defined as the ratio of polarized intensity to total intensity. In terms of Stokes parameters,

$$P = \frac{\sqrt{S_1^2 + S_2^2 + S_3^2}}{S_0}. \tag{1.26}$$

Note that $0 \leq P \leq 1$. $P = 0$ corresponds to completely unpolarized light, $P = 1$ corresponds to perfectly polarized light, and $0 < P < 1$ corresponds to partial polarization. Physically, we can understand partial polarization as an incoherent ensemble effect. We consider a light beam as an ensemble of photons, a fundamental quantum of light, that each carry their own polarization. If these photons are all coherently added, then the overall polarization changes. For example, equal amounts of horizontally polarized and vertically polarized light coherently added in phase will yield diagonally polarized light. If these photons are incoherently added, then the resultant light will be only partially polarized. In an extreme case, if every photon has a random polarization and there is no correlation with the polarization of other photons, then the light will be totally unpolarized.

Light polarization has several connections with the intensity interference described in the previous section. Intensity interference is caused by phase differences for coherent light polarized in the same direction. In contrast, polarization changes are due to phase differences for coherent light polarized in different directions. Both types of interference are sensitive to relative phases of light waves, and have similar applications.

For more details on deriving these expressions, see Goldstein's *Polarized Light* [18].

1.2 Quantum Mechanical Waves and Phases

In classical physics there is a distinction between two types of phenomena, waves and particles. Waves follow the wave equation, as we have discussed, and are spread out over time and space. Particles, in contrast, have definite positions and momenta. This description intuitively follows from human experience with the natural world. However, experiments in the 20th century showed that this understanding is conclusively wrong. Davisson and Thomson demonstrated that electrons display the same diffraction behavior as light does [5, 4]. Even when the electron beam is slowed to the point that only one electron is diffracted at a time, the interference pattern persists. This means that the electron is fundamentally a wave, and is described by a wavefunction. Indeed, all matter is described by wavefunctions.

We call this wavefunction $\Psi(\boldsymbol{x}, t)$. Unlike the light waves we have discussed $\Psi(\boldsymbol{x}, t)$ is a truly complex function. The magnitude of the function, $|\Psi(\boldsymbol{x},t)|^2$, can be interpreted as the probability density of measuring a given particle at position $\boldsymbol{x}$ and time t. The quantum wavefunction does not follow the same wave equation as classical waves, it instead evolves according to the Schrödinger equation,

$$i\hbar\frac{\partial}{\partial t}\Psi(\boldsymbol{x},t) = \left(-\frac{\hbar^2}{2m}\nabla^2 + V(\boldsymbol{x})\right)\Psi(\boldsymbol{x},t) = \hat{H}\Psi(\boldsymbol{x},t) \tag{1.27}$$

where ∇^2 is the Laplacian, $V(\boldsymbol{x})$ is the potential, and $\hat{H}$ is called the Hamiltonian. The Hamiltonian is an operator which consists of the sum of the kinetic energy operator (the Laplacian term) and the potential operator. A key feature of the Schrödinger equation is that it is linear in $\Psi(\boldsymbol{x},t)$. This linearity leads directly to interference phenomena like diffraction.

It can be useful to consider the eigenstates of the Hamiltonian, which we call ψ_n, and satisfy

$$\hat{H}\psi_n = \varepsilon_n\psi_n \tag{1.28}$$

where ε_n is the energy associated with ψ_n. Intuitively, the eigenvalues of the Hamiltonian are energies. Depending on the system of interest, there may be finitely many Ψ_n (with corresponding energies) or an infinite number. Taking this result with Eq. 1.27 yields

$$\Psi_n(\boldsymbol{x},t) = e^{-i\varepsilon_n t/\hbar}\psi_n(\boldsymbol{x}). \tag{1.29}$$

These eigenfunctions are constant in time, up to a phase which oscillates at a frequency linearly related to the energy of the state,

$$\varepsilon = \hbar\omega. \tag{1.30}$$

Because these states are sationary in time, we usually drop the time dependence and refer to only the time independent part, letting $\psi_n(\boldsymbol{x}) = \Psi(\boldsymbol{x}, 0)$. This allows us to write the time independent Schrödinger equation,

$$\hat{H}\psi_n = \varepsilon_n \psi_n. \tag{1.31}$$

Because the energy is a measurable quantity, it must be a real number. This constraint leads us to suspect that the Hamiltonian is Hermitian, or self-adjoint. Indeed, in quantum mechanics all measureable quantities are represented by Hermitian operators that act on the state or wavefunction. An important result from mathematics is that the eigenfunctions of Hermitian operators are orthogonal, meaning that their inner product is zero. We define the inner product of two functions $\psi_n(\boldsymbol{x})$ and $\psi_m(\boldsymbol{x})$ as

$$\int d\boldsymbol{x}\psi_n^*(\boldsymbol{x})\psi_m(\boldsymbol{x}). \tag{1.32}$$

Here, we are integrating over the entire domain of $\boldsymbol{x}$, usually $-\infty$ to ∞ in all spatial dimensions. In the case that $n = m$, we require that the inner product be 1, so

$$\int d\boldsymbol{x}\psi_n^*(\boldsymbol{x})\psi_n(\boldsymbol{x}) = \int d\boldsymbol{x}|\psi_n(\boldsymbol{x})|^2 = 1. \tag{1.33}$$

This is because $|\psi_n(\boldsymbol{x})|^2$ is the probability density of finding the particle at a particular point $\boldsymbol{x}$. If you sum the probability density of finding the particle over all possibilities, then the total must be 1. This is called the normalization condition. Taken together, we can state that the energy eigenstates form an orthonormal basis,

$$\int d\boldsymbol{x}\psi_n^*(\boldsymbol{x})\psi_m(\boldsymbol{x}) = \delta_{n,m} \tag{1.34}$$

where $\delta_{n,m}$ is the Kronecker delta, equal to 0 when $n \neq m$ and 1 when $n = m$. This is all reminiscent of linear algebra, and indeed the function $\psi_n(\boldsymbol{x})$ can be thought of as projection of a vector $|\psi_n\rangle$. The two are related by the inner product of $|\psi_n\rangle$ with the position eigenstate $|\boldsymbol{x}\rangle$,

$$\langle \boldsymbol{x} | \psi_n \rangle = \psi_n(\boldsymbol{x}) \tag{1.35}$$

The vector $|\psi_n\rangle$ is the representation of a particular state, called a ket. The inner product between two vectors is written as $\langle \psi_n | \psi_m \rangle$. The object $\langle \psi_n|$ is called a bra and is the conjugate transpose of $|\psi_n\rangle$. For example, kets are column vectors and bras are row vectors. Operators like the Hamiltonian can be represented as matrices, with the energy eigenstates forming an orthornormal set of basis vectors that span the system described by the Hamiltonian. This implies that any pure quantum state $|\varphi\rangle$ can be described by a superposition of Hamiltonian eigenstates,

$$|\varphi\rangle = \sum_n c_n \, |\psi_n\rangle \tag{1.36}$$

where c_n are complex constants. Here we have chosen $|\psi_n\rangle$ to satisfy

$$\hat{H} \, |\psi_n\rangle = \varepsilon_n \, |\psi_n\rangle \tag{1.37}$$

but in principle we can choose any set of basis vectors that span the relevant vector space. In this matrix formalism, the expectation value of any observable $\hat{A}$ is given by

$$\langle \hat{A} \rangle = \langle \psi_n | \, \hat{A} \, | \psi_n \rangle \tag{1.38}$$

It is worth noting that the act of measurement will yield one of the eigenvalues of $\hat{A}$, and collapse the state to one of the eigenstates of $\hat{A}$. This discussion was adapted from the treatment of the basics of quantum mechanics in the books of Shankar [19] and Schwabl [20].

1.2.1 Adiabatic Phases

So far we have discussed quantum systems described by Hamiltonians that are constant in time. We will turn our attention to a special subset of time varying Hamiltonians that change very slowly in time, following the work of Berry [21] and the treatment by Littlejohn [22]. We start in an arbitrary state $|\psi\rangle$, but because the Hamiltonian is changing the state will have some time dependence $|\psi(t)\rangle$. This time evolution is governed by the Schrödinger equation,

$$\hat{H}(t)\,|\psi(t)\rangle = i\hbar\frac{\partial}{\partial t}\,|\psi(t)\rangle\,. \tag{1.39}$$

At any moment of time the Hamiltonian can be diagonalized into its eigenstates. We will call these eigenstates $|n(t)\rangle$, and they carry the same slow time dependence as the Hamiltonian and satisfy

$$\hat{H}(t)\,|n(t)\rangle = \varepsilon(t)\,|n(t)\rangle\,. \tag{1.40}$$

We can decompose our general state $|\psi(t)\rangle$ into the $|n(t\rangle$ at any time,

$$|\psi(t)\rangle = \sum_n c_n(t)\,|n(t)\rangle\,. \tag{1.41}$$

Then, using this with Eq. 1.39 and Eq. 1.40 we can solve for the constants $c_n(t)$. This results in the differential equation,

$$\dot{c}_n(t) = -\frac{i}{\hbar}\varepsilon_n(t)c_n(t) - \sum_m c_m\,\langle n(t)|\,\frac{\partial}{\partial t}\,|m(t)\rangle\,. \tag{1.42}$$

In the case where the time evolution of the Hamiltonian, and thus the states, is very slow, the derivative in the second term is very small compared to the first term. If we neglect this term and solve for the constants we get

$$c_n(t) = e^{iA_n(t)} c_n(0) \tag{1.43}$$

where $A_n(t)$ is called the dynamical phase and is defined as

$$A_n(t) = -\frac{1}{\hbar} \int_0^t dt' \varepsilon_n(t'). \tag{1.44}$$

Since the dynamical phase is purely real, the $c_n(t)$ are at all times related to $c_n(0)$ by a phase factor, so the probability of finding $|\phi\rangle$ at any state is constant in time. In the special case that $|\psi(t)\rangle = |n(t)\rangle$, then we can say that the quantum number n is conserved. Notably, the states themselves and the associated energies will change, but the quantum number will not. This is called the adiabatic theorem, that if the Hamiltonian of a system is changed sufficiently slowly then the quantum number is conserved.

As an example, consider a particle in an infinite box, with length L, and energy $\varepsilon_n = \frac{n^2\pi^2\hbar^2}{2mL^2}$, shown in Fig. 1.5. We start with the particle in the $n = 1$ state and slowly expand the box to a new length $2L$. If the expansion is sufficiently slow, as in Fig. 1.5a), the particle will stay in the $n = 1$ state, even as the energy changes. Indeed, at the end of the process, the particle will have energy $\varepsilon_1 = \frac{\pi^2\hbar^2}{8mL^2}$ and the wavefunction will have accumulated a dynamical phase. If the process is not slow, then the particle can tunnel into states with different quantum number, such as in Fig. 1.5b).

If we do not neglect the second term of Eq. 1.42, then we can write Eq. 1.43 as

$$c_n(t) = e^{iA_n(t)} b_n(t). \tag{1.45}$$

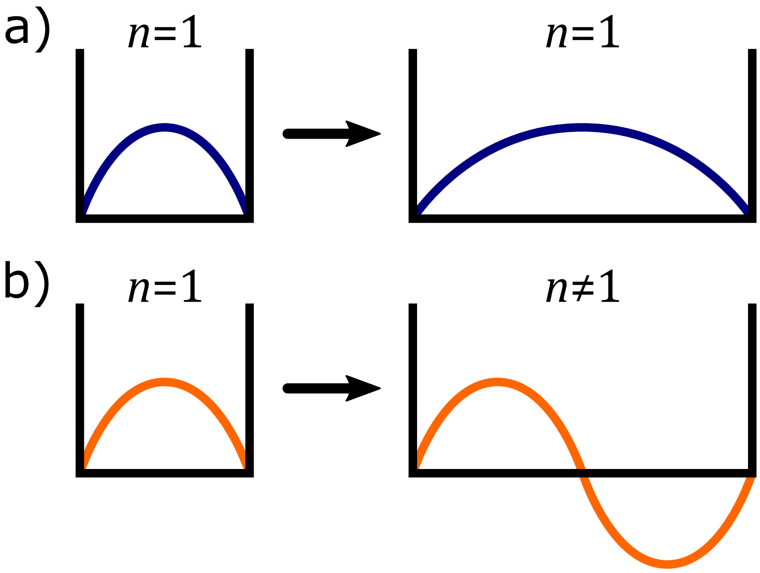

Figure 1.5: **Conservation of quantum number.** Cartoon of two evolution processes of a quantum particle in box beginning with the particle in the $n = 1$ state. In each process, the length of the box is increased. In **a)** the process is adiabatic, meaning that the expansion happens sufficiently slowly that the particle remains in the $n = 1$ state. In **b)** the evolution is not adiabatic, and the particle tunnels to a different state.

Plugging this into Eq. 1.42 yields

$$\dot{b}_n(t) = -\sum_m b_m \langle n(t)| \frac{\partial}{\partial t} |m(t)\rangle \, e^{i(A_m(t)-A_n(t))}. \tag{1.46}$$

We will for now neglect the off-diagonal ($m \neq n$) terms, since they have an oscillating term $e^{i(A_m(t)-A_n(t)}$ that can prevent them from accumulating over time. In this case, we integrate Eq. 1.46 and combine with Eq. 1.45 which yields

$$c_n(t) = e^{i(A_n(t)+\gamma_n(t))} c_n(0) \tag{1.47}$$

where $\gamma_n(t)$ is defined as

$$\gamma_n(t) = i \int_0^t dt' \, \langle n(t')| \frac{\partial}{\partial t'} |n(t')\rangle \tag{1.48}$$

and called the geometric, or Berry, phase. To see why this is called the geometric phase, we will consider a Hamiltonian $\hat{H}(\boldsymbol{P})$ that relies on some parameters $\boldsymbol{P} = \{P_1, P_2, ...\}$. These parameters can then have some time dependence $\boldsymbol{P}(t)$, and we again emphasize that this time dependence is slow. The eigenstates and energies of the Hamiltonian can then be written as

$$\hat{H}(\boldsymbol{P}) \left|n(\boldsymbol{P})\right\rangle = \varepsilon_n(\boldsymbol{P}) \left|n(\boldsymbol{P})\right\rangle . \tag{1.49}$$

The evolution of the system can be described as a trajectory in $\boldsymbol{P}$, beginning at some point $\boldsymbol{P}_0$ and ending at some point $\boldsymbol{P}_f$. The geometric phase can now be written as

$$\gamma_n = i \int_0^t dt' \left\langle n\right| \frac{\partial}{\partial \boldsymbol{P}} \left|n\right\rangle \cdot \frac{\partial \boldsymbol{P}}{\partial t'} = i \int_{\boldsymbol{P}_0}^{\boldsymbol{P}_f} \left\langle n\right| \frac{\partial}{\partial \boldsymbol{P}} \left|n\right\rangle \cdot d\boldsymbol{P}. \tag{1.50}$$

Notably, the geometric phase does not depend on the time evolution at all, only on the geometry of the trajectory through $\boldsymbol{P}$ and how the wavefunctions change through this trajectory. This is why the phase is called geometric. In the final result of Eq. 1.50, the integral becomes a line integral of a vector field. This vector field, defined as

$$\boldsymbol{\mathcal{A}}_n(\boldsymbol{P}) = i \left\langle n(\boldsymbol{P})\right| \frac{\partial}{\partial \boldsymbol{P}} \left|n(\boldsymbol{P})\right\rangle \tag{1.51}$$

is a vector potential, also called a connection. This quantity is called the Berry connection, and is analogous to the vector potential of electromagnetism. Just like in electromagnetism, the Berry connection has a gauge dependence. That is to say, if we transform the eigenstates of the Hamiltonian as

$$\left|n(\boldsymbol{P})\right\rangle \rightarrow \left|n'(\boldsymbol{P})\right\rangle = e^{if(\boldsymbol{P})} \left|n(\boldsymbol{P})\right\rangle \tag{1.52}$$

the Berry connection will transform as

$$\boldsymbol{\mathcal{A}}_n(\boldsymbol{P}) \to \boldsymbol{\mathcal{A}}'_n(\boldsymbol{P}) = \boldsymbol{\mathcal{A}}_n(\boldsymbol{P}) - \frac{\partial f(\boldsymbol{P})}{\partial \boldsymbol{P}}. \tag{1.53}$$

The overall phase of any quantum state is not physical, no observable will be affected by the transformation in Eq. 1.52. The fact that the connection is affected by the gauge transformation shows that it is also not directly measurable. In fact, this gauge dependence can extend even to the geometric phase,

$$\gamma(t)_n \to \gamma'(t)_n = \gamma(t)_n + f(\boldsymbol{P}(0)) - f(\boldsymbol{P}(t)). \tag{1.54}$$

which lead to it generally being disregarded until Michael Berry developed the theory of geometric phases in 1984. The geometric phase does have parts which are nonphysical and gauge dependent, but also contains physical elements which cannot be transformed away. To see this consider a closed trajectory through $\boldsymbol{P}$, meaning that it returns to the beginning point, shown schematically in Fig. 1.6. In this case, the gauge dependent terms in Eq. 1.54 cancel out and no gauge change can eliminate the geometric phase. It can be useful to define a gauge independent quantity $\boldsymbol{\Omega}(\boldsymbol{P})$, called the Berry curvature. In three dimensions the Berry curvature is defined as

$$\boldsymbol{\Omega}_n(\boldsymbol{P}) = \nabla_{\boldsymbol{P}} \times \boldsymbol{\mathcal{A}}_n(\boldsymbol{P}) \tag{1.55}$$

where $\nabla_{\boldsymbol{P}}$ is the vector of partial derivatives in $\boldsymbol{P}$. This definition continues our analogy with electromagnetism, with the Berry curvature analogous to the magnetic field. Then, if we consider the case where the trajectory in $\boldsymbol{P}$ is a closed loop, then we can use Stokes'

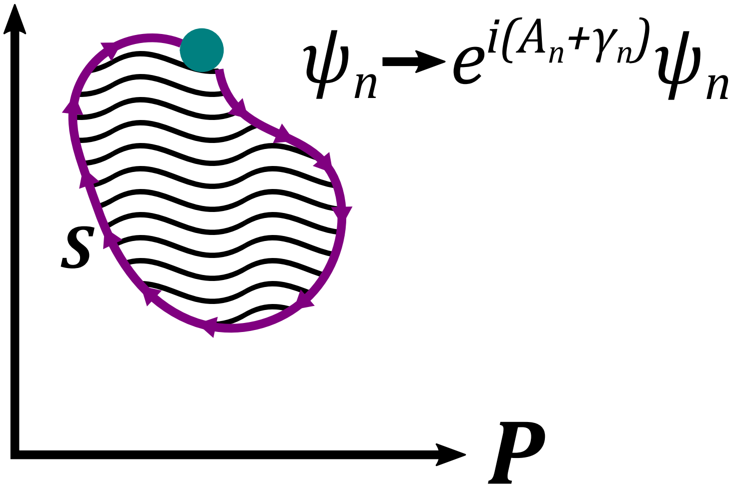

Figure 1.6: **Adiabatic accumulation of phases.** A particle in the state ψ_n is adiabatically evolved through $\boldsymbol{P}$ space. The trajectory is closed, and the surface enclosed is called S (black wiggly lines). At each point in $\boldsymbol{P}$ the energy eigenvalues and wavefunctions are different. The particle accumulates both a dynamical phase A_n due to the changing energies across the trajectory and a geometric phase γ_n due to changes in the wavefunction as a function of $\boldsymbol{P}$. The geometric phase is equal to the line integral of the Berry connection $\boldsymbol{\mathcal{A}}_n$ across the trajectory or the surface integral of the Berry curvature $\boldsymbol{\Omega}_n$ across the surface S. The geometric phase can be thought of as the flux of Berry curvature through S.

theorem to write the geometric phase as

$$\gamma_n = \oint \boldsymbol{\mathcal{A}}_n(\boldsymbol{P}) \cdot d\boldsymbol{P} = \int_S \boldsymbol{\Omega}_n(\boldsymbol{P}) \cdot d\boldsymbol{S} \tag{1.56}$$

where S is the surface bounded by the closed loop in $\boldsymbol{P}$ space. The geometric phase can also be viewed as the flux through the surface S, analogous to the magnetic flux. Fig. 1.6 shows an example trajectory with S being enclosed by the trajectory. The geometric phase γ_n is set by the flux of Berry curvature through this surface.

This formalism depends on ignoring the off-diagonal terms in Eq. 1.46, which in turn depends on the assumption that the $A_m - A_n$ term in the exponential will cause oscillations that prevents accumulation. This assumption is valid as long as the energies of the m and n states are different enough compared to the rate of change. If the different states are degenerate or otherwise close in energy, then the off-diagonal terms will persist, and cause coupling to other states. This quantity $\boldsymbol{\mathcal{A}}_{n,m}$ is called the non-Abelian Berry connection. In this case, the adiabatic theorem is not valid and the quantum number is not conserved. As a general rule, this can be avoided if the rate of Hamiltonian evolution, $\dot{H}$ is sufficiently slow compared to the energy separation of the states $\Delta\varepsilon$. Mathematically this comparison can be stated as

$$\frac{\dot{H}}{\hat{H}} \ll \frac{\Delta\varepsilon}{\hbar}. \tag{1.57}$$

As the process is slowed $\dot{H} \to 0$ and the approximation becomes more exact. Even when the energy scales are close, geometric phases are still physical, and can be very interesting.

Under slow evolution, we can understand wavefunctions as accumulating two different phases. The dynamical phase $A_n(t)$ is associated with the change in the eigenvalues of the Hamiltonian during evolution, while the geometric phase is associated with the evolution of the eigenfunctions of the Hamiltonian. Both phases can be experimentally accessed via interferometry for carefully designed experiments.

1.3 Interferometry and Quantum Mechanics in the Solid State

The quantum mechanics we have already discussed is designed around describing the states of single particles and the waves associated with these states. We now turn our attention to understanding the physics of solids. Because solids are made up of strongly interacting atoms, behavior very different from particles in vacuum can be observed. This has led to a great deal of interest in understanding and manipulating the quantum mechanical behavior of materials. One promising method is to probe the wave nature of particles in the solid state through interferometry.

We now consider the microscopic structure of condensed matter. We will focus on crystalline solids, where positively charged ionic cores are arranged in a periodic manner. Of course, no real crystal is perfectly periodic, but we will consider any defects as small perturbations to the periodic crystal. The electrons are then placed in this periodic environment and are free to interact both with the ions and external stimuli. We will largely ignore the motion of the ions and focus on the dynamics of the electron wavefunctions. This may appear to be an extreme approximation, but the electron dynamics turn out to be responsible for a huge field of interesting physics.

We will further confine our focus to single particle Hamiltonians in this dissertation. This approximation seems at first glance to be nonsensical, since there are of order 10^{23} atoms in macroscopic solids. The trick is to consider the vacuum to be the zero temperature equilibrium of the crystal. Because electrons are fermions, they will fill the available states starting at low energy. The energy level that separates occupied from unoccupied states at zero temperature is called the Fermi level, and the vast majority of dynamics takes place around this level. This is due to the fact that for electrons far from the Fermi level need much more energy to take part in the dynamics. We therefore will work with Hamiltonians that describe excitations from the equilibrium state of the crystal. These excitations are called quasiparticles, and in fact are made up of contributions from many different particles in the crystal. Quasiparticles can have properties that are very different from particles in vacuum. For example, the effective mass or spin of quasiparticles varies greatly. Quasiparticles can even take forms that do not mirror common fundamental particles. For example, the absensce of an electron can act as a quasiparticle called a hole.

Let us consider a periodic three dimensional crystal. We define vectors $\boldsymbol{a}_j$ such that if we move by $\boldsymbol{a}_j$ the crystal looks exactly the same. For example, if an atom is at $\boldsymbol{x} = 0$, then there will be other atoms at all positions $\boldsymbol{x} = \boldsymbol{a}_j$. The set of all points that see the same position and orientation of the crystal is called the Bravais lattice and satisfies the equation,

$$\boldsymbol{R} = n_1\boldsymbol{a}_1 + n_2\boldsymbol{a}_2 + n_3\boldsymbol{a}_3 \tag{1.58}$$

where n_j are integers. The fundamental unit of a Bravais lattice is called the unit cell, and the repeated unit cell makes up the crystal. Since the position of atoms is periodic, the potential of the system is also periodic $V(\boldsymbol{x}) = V(\boldsymbol{x} + \boldsymbol{a}_j)$. The Hamiltonian of this system is

$$\hat{H}(\boldsymbol{x}) = -\frac{\hbar^2}{2m}\nabla^2 + V(\boldsymbol{x}) = \hat{H}(\boldsymbol{x} + \boldsymbol{a}_j) \tag{1.59}$$

and has the same periodicity as the crystal. We define a translation operator $\mathcal{T}_j$ that operates as

$$\mathcal{T}_j f(\boldsymbol{x}) = f(\boldsymbol{x} + \boldsymbol{a}_j). \tag{1.60}$$

If we apply this to the Hamiltonian and a wavefunction, we get

$$\mathcal{T}_j(\hat{H}(\boldsymbol{x})\psi(\boldsymbol{x})) = \hat{H}(\boldsymbol{x} + \boldsymbol{a}_j)\psi(\boldsymbol{x} + \boldsymbol{a}_j) = \hat{H}(\boldsymbol{x})\mathcal{T}_j\psi(\boldsymbol{x}) \tag{1.61}$$

which shows that $\hat{H}$ and $\mathcal{T}_j$ commute. Matrices that commute share eigenfunctions, so the eigenfunctions ψ of $\hat{H}$ are also eigenfunctions of $\mathcal{T}_j$,

$$\mathcal{T}_j\psi(\boldsymbol{x}) = c(\boldsymbol{a}_j)\psi(\boldsymbol{x}). \tag{1.62}$$

Now let us imagine a translation operator $\mathcal{T}_{j'}$ that translates the system by a different vector that still satisfies $V(\boldsymbol{x}) = V(\boldsymbol{x} + \boldsymbol{a}_{j'})$. Applying both translations gives another translation operator $\mathcal{T}_{j+j'}$. The potential is still periodic under all of these translations, so argument about Hamiltonian commutation still holds and we can get the following eigenvalue relations for $\psi(\boldsymbol{x})$

$$\begin{aligned}\mathcal{T}_j\mathcal{T}_{j'}\psi(\boldsymbol{x}) &= c(\boldsymbol{a}_j)c(\boldsymbol{a}_{j'})\psi(\boldsymbol{x})\\ \mathcal{T}_j\mathcal{T}_{j'}\psi(\boldsymbol{x}) &= \mathcal{T}_{j+j'}\psi(\boldsymbol{x}) = c(\boldsymbol{a}_j+\boldsymbol{a}_{j'})\psi(\boldsymbol{x})\\ c(\boldsymbol{a}_j)c(\boldsymbol{a}_{j'}) &= c(\boldsymbol{a}_j+\boldsymbol{a}_{j'}).\end{aligned} \tag{1.63}$$

Since this must be true for any vector that satisfies Eq. 1.58, the last line in Eq. 1.63 implies that the c should take the form

$$c(\boldsymbol{R}) = e^{i\boldsymbol{k}\cdot\boldsymbol{R}} \tag{1.64}$$

and translating the wavefunction ψ by any vector $\boldsymbol{R}$ in the Bravais lattice gives,

$$\psi(\boldsymbol{x}+\boldsymbol{R}) = e^{i\boldsymbol{k}\cdot\boldsymbol{R}}\psi(\boldsymbol{x}). \tag{1.65}$$

We can restate this as Bloch's theorem [23], that the eigenfunctions of a Hamiltonian with a periodic potential can be chosen to take the form of a plane wave multiplied by a function that shares the periodicity of the Bravais lattice that makes up the potential,

$$\psi_{n,\boldsymbol{k}}(\boldsymbol{x}) = e^{i\boldsymbol{k}\cdot\boldsymbol{x}}u_{n,\boldsymbol{k}}(\boldsymbol{x}) \tag{1.66}$$

where $u_{n,\boldsymbol{k}}(\boldsymbol{x}+\boldsymbol{R}) = u_{n,\boldsymbol{k}}(\boldsymbol{x})$ and is called the cellular function. Bloch's theorem introduces $\boldsymbol{k}$, a vector called the wave vector which is the multidimensional analog to the wavenumber. $\boldsymbol{k}$ is also often called the crystal momentum or quasimomentum. Importantly, the periodicity of the crystal is also represented in the space of $\boldsymbol{k}$, called reciprocal space or momentum space. For every Bravais vector $\boldsymbol{R}$, there is a reciprocal vector $\boldsymbol{K}$

that satisfies

$$e^{i\boldsymbol{K}\cdot\boldsymbol{R}} = 1. \tag{1.67}$$

The set of these $\boldsymbol{K}$ is called the reciprocal lattice. It follows from Eq. 1.67 that if a wave vector $\boldsymbol{k}$ satisfies Eq. 1.66 any wave vector $\boldsymbol{k}'$ defined as $\boldsymbol{k} = \boldsymbol{k}' + \boldsymbol{K}$ will also satisfy Eq. 1.66. This implies that the wavefunction is periodic in $\boldsymbol{k}$, so

$$\psi_{n,\boldsymbol{k}+\boldsymbol{K}} = \psi_{n,\boldsymbol{k}}. \tag{1.68}$$

This in turn implies that the energies of the Hamiltonian are periodic in $\boldsymbol{k}$. This means we can restrict our attention to the fundamental unit of a given reciprocal lattice, called the Brillouin zone. All together, we have restricted the problem of a crystal to the Hamiltonian eigenvalue problem,

$$\hat{H}\psi_{n,\boldsymbol{k}}(\boldsymbol{x}) = \varepsilon_{n,\boldsymbol{k}}\psi_{n,\boldsymbol{k}}(\boldsymbol{x}) \tag{1.69}$$

where $\boldsymbol{k}$ is limited to the Brillouin zone in reciprocal space and $\boldsymbol{x}$ is limited to the unit cell of the Bravais lattice. Since we are dealing with a finite volume in real and reciprocal space, we should expect $\varepsilon_{n,\boldsymbol{k}}$ to give a discrete spectrum at each value of $\boldsymbol{k}$. These energies do vary continuously as a function of $\boldsymbol{k}$, but there are discrete bands labelled by the quantum number n. The relationship between $\varepsilon_{n,\boldsymbol{k}}$ and $\boldsymbol{k}$ is called the band structure.

We refer to the states with a given n as a band. Notably, not all energies have allowed bands. The relationship between these bands and the Fermi level is important. If the Fermi level is in the middle of the band, the material conducts electricity and is called a metal. If the Fermi level is between bands, then the material is an insulator. In the insulating case, the bands below the Fermi level are called valence bands and the bands above the Fermi level are called conduction bands. The energy gap between the highest valence band and the lowest conduction band is called the band gap. We are primarily concerned here with semiconductors, a special class of insulators that have small band gaps. Another feature to point out is that as $\boldsymbol{k}$ is varied, degeneracies in the various $\varepsilon_{n,\boldsymbol{k}}$ can be created and destroyed. For additional details on these derivations and other topics in general condensed matter phsycis, see *Solid State Physics* by Ashcroft and Mermin [24].

1.3.1 Adiabatic Evolution in Condensed Matter

It is often useful to think of condensed matter Hamiltonians as functions of $\boldsymbol{k}$. At each $\boldsymbol{k}$, we can diagonalize the Hamiltonian to find the wavefunctions $\psi_{n,\boldsymbol{k}}$ and energies $\varepsilon_{n,\boldsymbol{k}}$. Interactions with external stimuli, for example electric fields, can cause particles to move to different $\boldsymbol{k}$, which can in turn cause the accumulation of adiabatic phases. We can take the results of section 1.2.1, treating $\boldsymbol{k}$ as the parameter space through which we evolve the Hamiltonian. Suppose we have a closed trajectory $\boldsymbol{k}(t)$ and start in some state $\psi_{n,\boldsymbol{k}_0}$. Then after this trajectory has been traversed the state will be,

$$\psi_{n,\boldsymbol{k}_0} \rightarrow e^{i(A_n+\gamma_n)}\psi_{n,\boldsymbol{k_0}} \tag{1.70}$$

with the dynamical and geometric phases defined as before, except that the integrals which define γ_n are now over $\boldsymbol{k}$,

$$\gamma_n = \oint \boldsymbol{\mathcal{A}}_n(\boldsymbol{k})d\boldsymbol{k} = \int_S \boldsymbol{\Omega}_n(\boldsymbol{k}) \cdot dS_{\boldsymbol{k}} \tag{1.71}$$

where $S_{\boldsymbol{k}}$ is a surface in $\boldsymbol{k}$ space. However, as we have noted, degeneracies are not uncommon in solid state crystals and it is important to account for their effects. Notably the off-diagonal elements of the Berry connection can no longer be ignored, and the connection now becomes,

$$\boldsymbol{\mathcal{A}}_{n,m}(\boldsymbol{k}) = i \langle n| \nabla_{\boldsymbol{k}} |m\rangle . \tag{1.72}$$

The diagonal terms are exactly as before, but we can write the off-diagonal terms ($n \neq m$) of Eq. 1.72 as

$$\boldsymbol{\mathcal{A}}_{n,m}(\boldsymbol{k}) = i \frac{\langle n| \nabla_{\boldsymbol{k}} \hat{H} |m\rangle}{\varepsilon_m - \varepsilon_n} \tag{1.73}$$

and the Berry curvature can be written as

$$\boldsymbol{\Omega}_n(\boldsymbol{k}) = i \sum_{m \neq n} \frac{\langle n| \nabla_{\boldsymbol{k}} \hat{H} |m\rangle \times \langle m| \nabla_{\boldsymbol{k}} \hat{H} |n\rangle}{(\varepsilon_m - \varepsilon_n)^2}. \tag{1.74}$$

This provides justification for our earlier neglect of off-diagonal terms, since they become very small when the difference between ε_n and ε_m is large. However, when the energies are close or degenerate these terms can be quite large.

Now we consider two states $|0\rangle$ and $|1\rangle$ that are degenerate at some point $\boldsymbol{k}'$. We will constrict ourselves to the small part of $\boldsymbol{k}$ space near the degeneracy such that we can consider this subsystem to be described by a two level system. Any two level system can be described by the generic form

$$\hat{H} = \boldsymbol{h}(\boldsymbol{k}) \cdot \hat{\boldsymbol{\sigma}} \tag{1.75}$$

where $\boldsymbol{h}(\boldsymbol{k})$ is a three dimensional vector that is allowed to vary as a function of $\boldsymbol{k}$ and $\hat{\boldsymbol{\sigma}}$ is the vector of Pauli matrices. We can parameterize $\boldsymbol{h}$ along it's cartesian coordinates $\boldsymbol{h}(\boldsymbol{k}) = h(k_x, k_y, k_z)$. We require the k components to be normalized such that $|\boldsymbol{h}| = h$. In matrix form the Hamiltonian then takes the form

$$\hat{H} = h \begin{pmatrix} k_z & k_x - ik_y \\ k_x + ik_y & k_z \end{pmatrix} \tag{1.76}$$

with eigenvalues $\pm h$. Note that this Hamiltonian conveniently has the relation

$$\nabla_{\boldsymbol{k}} \hat{H} = \hat{\boldsymbol{\sigma}}. \tag{1.77}$$

We will work in a basis such that the $\boldsymbol{h}$ is aligned along the z axis. This results in the Hamiltonian eigenstates, which we call $|0\rangle$ and $|1\rangle$, being the same as the eigenstates of $\hat{\sigma}_z$. The elements of the Berry connection can now be calculated from Eq. 1.74 with elements

$$\begin{aligned}
\Omega_{1,x} &= i\frac{\langle 1|\,\hat{\sigma}_y\,|0\rangle\,\langle 0|\,\hat{\sigma}_z\,|1\rangle - \langle 1|\,\hat{\sigma}_z\,|0\rangle\,\langle 0|\,\hat{\sigma}_y\,|1\rangle}{4h^2} = 0 \\
\Omega_{1,y} &= i\frac{\langle 1|\,\hat{\sigma}_z\,|0\rangle\,\langle 0|\,\hat{\sigma}_x\,|1\rangle - \langle 1|\,\hat{\sigma}_x\,|0\rangle\,\langle 0|\,\hat{\sigma}_z\,|1\rangle}{4h^2} = 0 \\
\Omega_{1,z} &= i\frac{\langle 1|\,\hat{\sigma}_x\,|0\rangle\,\langle 0|\,\hat{\sigma}_y\,|1\rangle - \langle 1|\,\hat{\sigma}_y\,|0\rangle\,\langle 0|\,\hat{\sigma}_x\,|1\rangle}{4h^2} = -\frac{1}{2h^2}
\end{aligned} \tag{1.78}$$

for $\boldsymbol{\Omega}_1$. We note that $\boldsymbol{\Omega}_0 = -\boldsymbol{\Omega}_1$ because of the cross product in Eq. 1.74 This result is obtained when $\boldsymbol{h}$ is aligned along z, but we can rotate this result to any coordinate axis which yields the result

$$\boldsymbol{\Omega}_{0(1)} = +(-)\frac{\boldsymbol{h}}{2h^3} \tag{1.79}$$

which is the equation for a monopole. Therefore, degeneracies in band energies cause monopoles of Berry curvature [21, 25]. The geometric phase acquired during evolution over a closed trajectory is the flux through the enclosed surface from this monopole. For further discussions of the effects of Berry curvature in materials, see the review by Xiao, Chang, and Niu [25].

1.3.2 Dephasing and Interactions

We have so far focused on pure crystals, that is to say perfectly periodic groups of atoms, and the Bloch wavefunctions that arise because of this periodicity. Usually, we will further limit our focus to the subset of Bloch wavefunctions that are relevant to a particular problem or experiment. However, real materials are not perfect, and the model Hamiltonians that we use to understand Bloch wavefunctions do not account for a wide variety of phenomena. Such phenomena include crystal imperfections or impurities, lattice vibrations, or coupling to external stimuli such as light. All of these processes can destroy the coherence of Bloch wavefunctions. In fact there are so many of these processes that most wavefunctions will lose coherence in a picosecond or less.

In order to understand a more realistic picture, it is helpful to introduce a quantity called dephasing [26]. To understand how dephasing arises, it is useful to divide the universe into two subsystems, the system of interest and the environment. We can then write the Hamiltonian as a sum of three terms. The first term is the system Hamiltonian, which describes the behavior of perfect crystals and is limited to the states of interest. The second term is the Hamiltonian of the environment, and the third term governs interactions between the system and the environment. The interaction Hamiltonian governs the dephasing of the system. Off-diagonal terms govern population relaxation, where the particle ends in a different state than before the interaction. Radiative relaxation from coupling an excited electron to the electromagnetic field is an example of population relaxation. In contrast, the diagonal terms cause pure dephasing. This effect can be viewed as a time dependent perturbation to the energy of a given state, which can cause superpositions of states to become uncorrelated. This loss of correlation between the phases of different states is called dephasing.

Both the off-diagonal and diagonal terms lead to dephasing, causing parts of the wavefunction to lose coherence. These parts of the wavefunction are no longer well described by the system Hamiltonian due to interactions with the environment. We can describe this mathematically as decaying exponential causing the magnitude of the wavefunction to decrease over time. The rate at which this dephasing occurs is called the dephasing rate, Γ. This rate is often given in units of energy, which can be related to a rate by dividing by $\hbar$. The theory of dephasing in crystals has been studied in depth [26, 27, 28, 29].

Consider an adiabatic process through a trajectory where the Berry connection is zero, so the only effects we need to consider are the dynamical phase and dephasing. The state evolves as

$$|n(t)\rangle = e^{iA_n(t) - \mathcal{G}_n(t)} |n(0)\rangle \tag{1.80}$$

where $A_n(t)$ is the dynamical phase and $\mathcal{G}_n(t)$ is the total dephasing. This factor is defined as

$$\mathcal{G}_n(t) = \frac{1}{\hbar} \int_{t_0}^{t} dt' \; \Gamma_n(\boldsymbol{k}(t')) \tag{1.81}$$

where the dephasing rate can vary as a function of $\boldsymbol{k}$ or time. Since Γ is non-negative the dephasing will act as a decaying exponential on $|n\rangle$. The actual mechanisms of dephasing are numerous and can be quite complex. In this dissertation we will usually assume that the dephasing rate is constant for a given process. In this case Eq. 1.80 simplifies to

$$|n(t)\rangle = e^{iA_n(t) - (t - t_0)\Gamma_n/\hbar} |n(0)\rangle \, . \tag{1.82}$$

This approximation loses much of the detail associated with dephasing, but it can still be useful. The way to view this constant Γ_n is as the mean dephasing rate experienced by the state $|n\rangle$ over the process of interest.

Understanding the dephasing in a material is key to designing interference experiments. The relatively high dephasing in materials, when compared to atomic or photonic systems, is the main hurdle in measuring interference of Bloch wavefunctions. However, the sensitivity of interference experiments to dephasing can be beneficial as it can provide insight into the dephasing mechanisms of a given interferometry system [30, 31].

1.4 Gallium Arsenide and the Luttinger Hamiltonian

The experiments of this dissertation have all been performed on gallium arsenide (GaAs). GaAs is an extremely well understood semiconductor that is common in many electronic devices. This makes GaAs advantageous to work with since there are high quality samples available and robust technologies for working with it. It is a direct bandgap semiconductor, which means it is easy to optically excite electrons across the bandgap.

In this dissertation we will be focusing on the physics very near the band gap and use an approximation method called the $\boldsymbol{k}\cdot\boldsymbol{p}$ method. We begin by considering a Bloch wavefunction in a periodic Hamiltonian,

$$\left(\frac{\hat{p}^2}{2m}+\hat{V}\right)e^{i\boldsymbol{k}\cdot\boldsymbol{x}}u_{n,\boldsymbol{k}}=\varepsilon_{n,\boldsymbol{k}}e^{i\boldsymbol{k}\cdot\boldsymbol{x}}u_{n,\boldsymbol{k}} \tag{1.83}$$

where $\hat{p}=-i\hbar\nabla$ is the momentum operator. We can remove the plane wave part to focus on the cellular function and get

$$\left(\frac{\hat{p}^2}{2m}+\frac{\hbar}{m}\boldsymbol{k}\cdot\boldsymbol{p}+\frac{\hbar^2k^2}{2m}+\hat{V}\right)u_{n,\boldsymbol{k}}=\varepsilon_{n,\boldsymbol{k}}u_{n,\boldsymbol{k}}. \tag{1.84}$$

The terms of the original Hamiltonian are still present, so we can view the $\boldsymbol{k}\cdot\boldsymbol{p}$ term as a perturbation. We expand the perturbation to second order around a band extremum, yielding the results,

$$\begin{aligned} u_{n,\boldsymbol{k}} &= u_{n,\mathbf{0}} + \frac{\hbar}{m} \sum_{m \neq n} \frac{\langle u_{n,\mathbf{0}} | \, \boldsymbol{k} \cdot \boldsymbol{p} \, | u_{m,\mathbf{0}} \rangle}{\varepsilon_{n,\mathbf{0}} - \varepsilon_{m,\mathbf{0}}} u_{m,\mathbf{0}} \\ \varepsilon_{n,\boldsymbol{k}} &= \varepsilon_{n,\mathbf{0}} + \frac{\hbar^2 k^2}{2m} + \frac{\hbar^2}{m^2} \sum_{m \neq n} \frac{| \langle u_{n,\mathbf{0}} | \, \boldsymbol{k} \cdot \boldsymbol{p} \, | u_{m,\mathbf{0}} \rangle |^2}{\varepsilon_{n,\mathbf{0}} - \varepsilon_{m,\mathbf{0}}} \end{aligned} \tag{1.85}$$

where $u_{n,\mathbf{0}}$ is the cellular function at the band edge and $\varepsilon_{n,\mathbf{0}}$ is the energy at the band edge. It is useful to define an effective mass for each band,

$$\frac{1}{m_n^*} = \frac{1}{m} + \frac{2}{m^2 k^2} \sum_{m \neq n} \frac{| \langle u_{n,\mathbf{0}} | \, \boldsymbol{k} \cdot \boldsymbol{p} \, | u_{m,\mathbf{0}} \rangle |^2}{\varepsilon_{n,\mathbf{0}} - \varepsilon_{m,\mathbf{0}}} \tag{1.86}$$

which can then be used to write the band energy as

$$\varepsilon_{n,\boldsymbol{k}} = \varepsilon_{n,\mathbf{0}} + \frac{\hbar^2 k^2}{2 m_n^*}. \tag{1.87}$$

This is the energy of a free particle of mass m_n^* offset by the band edge. It is important to note that the coupling terms in Eq. 1.86 can make the effective mass negative. In GaAs the valence bands have negative effective mass, so it is useful to describe their excitations as holes with positive mass. However, the gallium and arsenic atoms that make up GaAs are quite massive which leads to an important spin-orbit coupling. The spin-orbit interaction is described by the Hamiltonian,

$$\hat{H}_{SO} = \lambda \hat{\boldsymbol{l}} \cdot \hat{\boldsymbol{s}} \tag{1.88}$$

where λ is the spin-orbit coupling, $\hat{\boldsymbol{l}}$ is the orbital angular momentum operator, and $\hat{\boldsymbol{s}}$ is the spin operator. We can limit the states we consider by using group theory to take advantage of the translational and rotational symmetries of GaAs. GaAs is a zinc-blende crystal, and has cubic symmetry. Group theory then gives us the result that the angular momentum states of the Bloch wavefunctions must be s-like ($l = 0$) or p-like ($l = 1$). These states are split by the spin orbit interaction, so we will focus our attention on the lowest energy conduction band (s-like) and the highest energy valence band (p-like). There is only one $l = 0$ state, but there are three degenerate $l = 1$ states. We will label these states by the magnetic quantum number $m_l = -1, 0, 1$ which corresponds to the eigenvalues of $\hat{l}_z$. However the eigenstates of Eq. 1.88 are not eigenstates of orbital angular momentum or spin, they are eigenstates of the total angular momentum operator $\hat{\boldsymbol{J}} = \hat{\boldsymbol{l}} + \hat{\boldsymbol{s}}$. The eigenvalues of $\hat{J}_z$ are called m_J and can range from $-J$ to J in steps of 1. We label the total angular momentum eigenstates as $|J, m_J\rangle$. For s-like bands, there are two states corresponding to spin up $|\uparrow\rangle$ and spin down $|\downarrow\rangle$. We use the arrows to distinguish them from the p-like states. The six $l = 1$ states are

$$\begin{gathered} |3/2, 3/2\rangle \\ |3/2, 1/2\rangle \\ |3/2, -1/2\rangle \\ |3/2, -3/2\rangle \\ |1/2, 1/2\rangle \\ |1/2, -1/2\rangle \,. \end{gathered} \tag{1.89}$$

However, due to the spin-orbit interaction, the $J = 1/2$ states are much lower energy than the $J = 3/2$ states. They make up what is called the split off band and are sufficiently far from the physics of interest so we can safely ignore their contributions to this work. This leaves us with a 2 dimensional Hamiltonian for the conduction band electrons and a 4 dimensional Hamiltonian for the valence band holes. The conduction band Hamiltonian

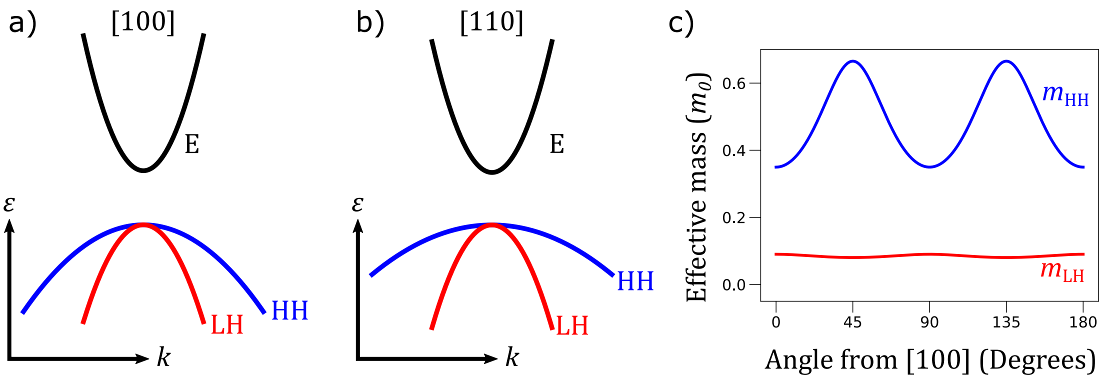

Figure 1.7: **Band structure of the Luttinger Hamiltonian.** **a)** The Luttinger Hamiltonian model of gallium arsenide (GaAs) band structure along the [100] crystal direction. The gap is shrunk by several orders of magnitude for visibility purposes. The conduction band (E) is in black, the heavy hole band (HH) is in blue and the light hole band (LH) is in red. The bands are parabolic. **b)** The band structure in the [110] direction, with the colors the same as in **a)**. The HH is noticably heavier, demonstrating the dependence of the effective masses on crystal direction. **c)** The effective masses of the HH and LH as a function of crystal angle in the $k_z = 0$ plane.

must be isotropic since the s-like states are isotropic, so it is simply

$$\hat{H}_c(\boldsymbol{k}) = E_g + \frac{\hbar^2 k^2}{2m_c} \tag{1.90}$$

where E_g is the energy of the band gap, $m_c = 0.063 m_0$ is the effective mass of the conduction band, and m_0 is the mass of a free electron. In contrast, the valence band must obey the GaAs crystal symmetries and is more complicated. The derivation of this Hamiltonian was done by Luttinger and Kohn [32], and can be accomplished by carefully applying group theory and expanding the $\boldsymbol{k} \cdot \boldsymbol{p}$ Hamiltonian. The details of this calculation are beyond the scope of this work but we will cite the result,

$$\hat{H}_V(\boldsymbol{k}) = -\frac{\hbar^2}{2m}\left[(\gamma_1 + \frac{5}{2}\gamma_2)k^2 - 2\gamma_3(\boldsymbol{k} \cdot \hat{\boldsymbol{J}})^2 + 2(\gamma_3 - \gamma_2)(k_x^2 \hat{J}_x{}^2 + k_y^2 \hat{J}_y{}^2 + k_z^2 \hat{J}_z{}^2)\right] \tag{1.91}$$

which is called the Luttinger Hamiltonian. The parameters γ_1, γ_2, and γ_3 are scalar constants called Luttinger parameters that vary based on material. The $\hat{J}_{x,y,z}$ are the $J = 3/2$ total angular momentum matrices and $\hat{\boldsymbol{J}}$ is the vector of these matrices. In the J_z basis these matrices are

$$\hat{J}_x = \begin{pmatrix} 0 & \sqrt{3}/2 & 0 & 0 \\ \sqrt{3}/2 & 0 & 1 & 0 \\ 0 & 1 & 0 & \sqrt{3}/2 \\ 0 & 0 & \sqrt{3}/2 & 0 \end{pmatrix} \tag{1.92}$$

$$\hat{J}_y = \begin{pmatrix} 0 & -i\sqrt{3}/2 & 0 & 0 \\ i\sqrt{3}/2 & 0 & -i & 0 \\ 0 & i & 0 & -i\sqrt{3}/2 \\ 0 & 0 & i\sqrt{3}/2 & 0 \end{pmatrix} \tag{1.93}$$

$$\hat{J}_z = \begin{pmatrix} 3/2 & 0 & 0 & 0 \\ 0 & 1/2 & 0 & 0 \\ 0 & 0 & -1/2 & 0 \\ 0 & 0 & 0 & -3/2 \end{pmatrix}. \tag{1.94}$$

The Luttinger Hamiltonian is 4 dimensional and thus we have four eigenstates. The system is symmetric under time reversal so we expect a pseudo-spin degeneracy. This leaves us with two bands that are each doubly degenerate. We call these bands the heavy hole (HH) and the light hole (HH) because of the differences between their effective masses. The energies of these states are

$$\varepsilon_{HH,LH}(\boldsymbol{k}) = \gamma_1 k^2 \pm 2\sqrt{\gamma_2^2 k^4 - \gamma_2^2(k_x^2 k_y^2 + k_x^2 k_z^2 + k_y^2 k_z^2) + 3\gamma_3^2(k_x^2 k_y^2 + k_x^2 k_z^2 + k_y^2 k_z^2)} \tag{1.95}$$

where the heavy hole corresponds to the plus sign of the square root term and the

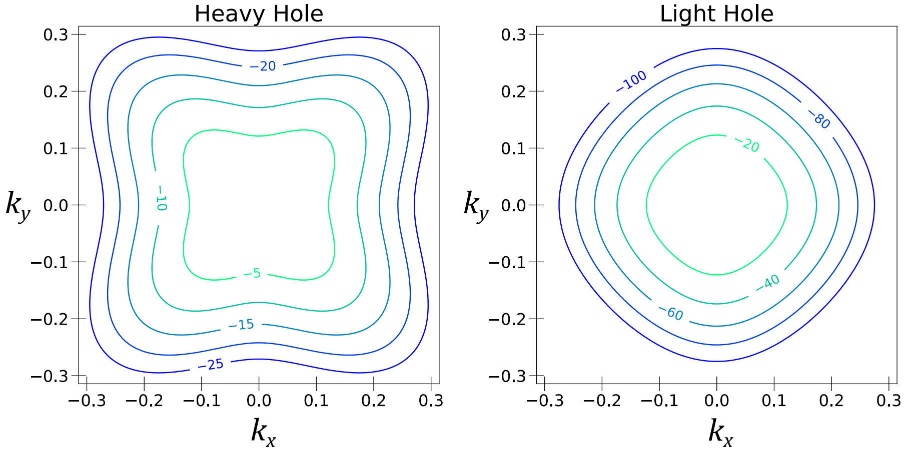

Figure 1.8: **Energy contours of the Luttinger hamiltonian**. Energy contours of the heavy hole (left) and the light hole (right) bands in the $k_z = 0$ plane. The four fold rotational symmetry of GaAs is evident in the contours. Energies are given in meV. Note that the contours of the heavy hole are given in steps of 5 meV and the contours of the light hole are given in steps of 20 meV. k_x and k_y are given in units of inverse GaAs lattice constant $1/a_{\mathrm{GaAs}}$.

light hole corresponds to the minus sign. Fig 1.7 a)-b) shows the band structure of the Luttinger Hamiltonian along two different directions. Along straight trajectories through $\boldsymbol{k} = 0$ the energies are parabolic, and thus we can define an effective mass. However this effective mass changes based on the orientation of the trajectory and the heavy hole is always heavier than the light hole. Fig. 1.7 c) shows the effective masses for the heavy hole and light hole as a function of crystal angle. The constant energy surfaces of these bands look like spheres that are modified to fit the 90° rotation symmetry of GaAs. Some of these constant energy surfaces for the $k_z = 0$ plane is shown in Fig. 1.8. The light hole goes to lower energies much more quickly.

We can understand the first term of the Luttinger Hamiltonian to be a normal kinetic term quadratic in the magnitude of the wave vector which arises from the form of Bloch wavefunctions. The second term is a statement of the $\boldsymbol{k} \cdot \boldsymbol{p}$ expansion with the effects of spin-orbit coupling. The third term enforces the cubic symmetry of the GaAs crystal.

The Luttinger parameters control the precise shape of the bands and the associated wavefunctions. A schematic understanding of what the Luttinger parameters do is that γ_1 is an overall mass factor, γ_2 controls how different the heavy hole and light hole masses are from each other, and γ_3 controls the strength of the anisotropy. In the case where $\gamma_3 = \gamma_2$, the anisotropy vanishes and continuous rotational symmetry is restored. For further details about the $\boldsymbol{k} \cdot \boldsymbol{p}$ method and the Luttinger Hamiltonian, see Lew Yan Voon and Willatzen's *The $k \cdot p$ Method* [33] and Yu and Cardona's *Fundamentals of Semiconductors* [34].

Chapter 2

High Order Sideband Polarimetry as a Bloch Wave Interferometer

Interferometry is a powerful tool that takes advantage of wave interference to make precise measurements. In optical interferometry, path length differences on the order of 10^{-21} have been detected [17]. Matter wave interferometry can detect extremely small differences in forces like gravity using atomic systems [35, 36]. In condensed matter, the phases developed in section 1.3.1 contain a great deal of interesting physics. The dynamical phase contains information about the electronic band structure and Hamiltonian parameters that affect this structure. The geometric phase contains information about the wavefunctions themselves, and the underlying topology and geometry of the crystal. The wide variety of wavefunctions that can exist in condensed matter make the possible applications of interferometry in the solid state broad as well. However, the reality is that in materials wavefunctions are much more susceptible to interactions and therefore dephasing than in photonic or atomic systems. Indeed, in most condensed matter systems the wavefunctions are only coherent for a picosecond or less, which makes building an interferometer extremely difficult.

However, there has been significant progress in observing interference phenomenon and building interferometers in materials. This can be accomplished by engineering systems that have extremely small numbers of interactions, such as chiral edge states of quantum wires [37, 38, 31, 10]. In these systems symmetry or topology protects the states from most interactions so the dephasing is kept low. Because of the strict experimental parameters required for this kind of work, there are relatively few systems that can host these types of interferometers. Another option is to focus on phenomena that happen over a very small amount of time or space. Scanning tunneling microscopy is sensitive to movements on sub-nanometer scale, and is able to observe interference of surface state wavefunctions [6, 7, 8, 9]. However, it is difficult to build a true interferometer in this sense because the scale is so small and the experimental readout is limited to surface states.

The development of strong lasers has opened the door to measuring interference processes that occur at extremely small time scales. A powerful experimental method that takes advantage of this is called high harmonic generation (HHG). In HHG a powerful laser at freqeuncy ω is incident on a material. This laser excites and drives charge carriers resulting in the release of harmonics at frequency

$$\omega_n = n\omega \tag{2.1}$$

where n is an integer. Although HHG can be observed in gases, we will focus on solid state HHG which has been observed in a variety of materials [39, 40, 13]. The underlying idea is to use the strong electric fields that make up the driving laser to accelerate quasiparticles throughout the Brillouin zone before they succumb to dephasing [11, 12, 13, 14, 15]. The harmonics can be measured relatively easily at a macroscopic scale using well established optical methods and in a wide variety of materials including bulk systems. Since the process is coherent, the harmonics can be the result of several different contributions which interfere to set the final intensity and polarization of the outgoing light. Furthermore, HHG will usually produce many orders with each order having a different amount of interference. Looking at the whole HHG spectra is then analogous to viewing an interferogram.

Because HHG relies on such high power lasers, harmonics can be created through a variety of interband and intraband processes. Similarly, depending on the material of interest, different intraband trajectories, multiple interband ionization pathways, or the presence of both intraband and interband contributions can lead to interference [12, 13, 15, 41, 42, 43]. This variety of interference mechanisms makes extracting information from the interference difficult, since a given behavior could be due to many microscopic processes.

In this work, we report on the development of a similar process to HHG called high-order sideband generation (HSG) [44]. In HSG a weak laser of frequency ω_{NIR} is tuned to the band gap of a semiconductor, which excites electrons across the gap and creates electron hole pairs. These electron hole pairs are then driven by an intense but low frequency laser called the terahertz (THz) of frequency ω_{THz}. The electron hole pairs are driven back together, where they annihilate and release sidebands at frequency

$$\omega_n = \omega_{\mathrm{NIR}} + n\omega_{\mathrm{THz}} \tag{2.2}$$

where n is an integer called the sideband order. In materials with inversion symmetry n must be even. In this work, we will only work in the inversion symmetric (001) plane, and so there will be no odd order sidebands. Notably, the drive laser photon energy must be much lower energy than the bandgap. This means that the acceleration dynamics can be viewed as adiabatic and we can use the results of sections 1.2.1 and 1.3.1. Essentially, the drive laser cannot drive any charge carriers across the band gap, so the charge carriers stay in the bands they start in, except in the case of non-Abelian Berry connection. This simplification allows for a much more straightforward attribution of interference behavior to microscopic processes and makes the extraction of information about the underlying physics much easier.

In this chapter we demonstrate how HSG is affected by quantum interference, and show that by measuring the polarization of sidebands we can extract information about the system. In particular we will show how Hamiltonian parameters can be extracted from sideband spectra which allows the reconstruction of Bloch wavefunctions in GaAs [45, 46].

2.1 High Order Sideband Generation: A 3 Step Process

Consider a semiconductor with two bands, a valence band and a conduction band seperated by a band gap of $\hbar\omega_{\mathrm{NIR}}$. The two bands are parabolic in energy, but have different effective masses, so the energies of these bands are,

$$\varepsilon_j(\boldsymbol{k}) = \pm\frac{\hbar^2 k^2}{2m_j} \tag{2.3}$$

where k is the magnitude of the wave vector, m_j is the effective mass of the electron or hole, ε_j is the energy of the electron or hole, the $\pm$ is $+$ for the electron band and $-$ for the hole band. It can be shown very generally [24] that the velocity of a particle in a band has velocity

$$\boldsymbol{v}_j(\boldsymbol{k}) = \frac{1}{\hbar}\nabla_{\boldsymbol{k}}\varepsilon_j(\boldsymbol{k}) = \frac{\hbar}{m_j}\boldsymbol{k} \tag{2.4}$$

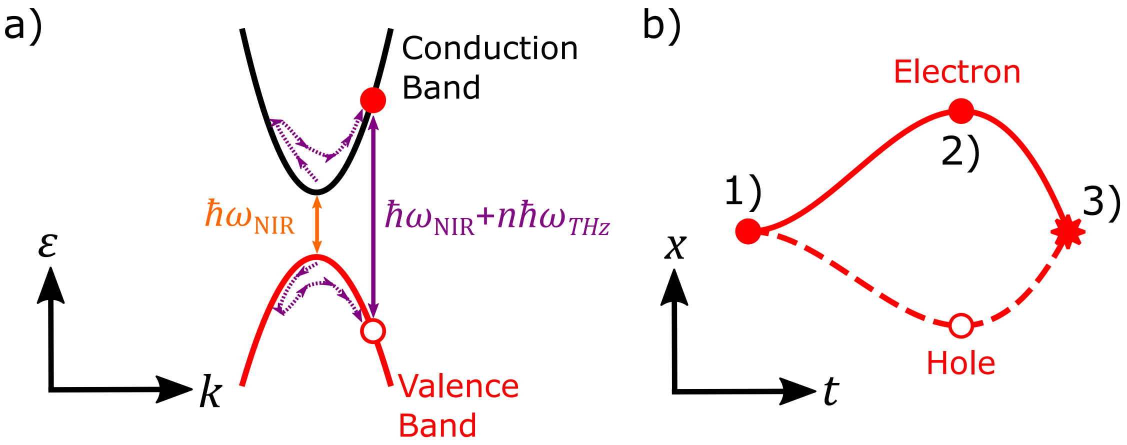

Figure 2.1: **High-order Sideband Generation (HSG). a)** The momentum space picture of HSG. A NIR laser excites an electron across the gap, leaving behind a hole in the valence band. Note that the band gap has been shrunk by several orders of magnitude for visualization purposes. Strong light at low frequency in the terahertz range (THz) adiabatically drives the electron and hole to higher momentum. Because the THz drive is sinusoidal it can accelerate the electron and hole back together, causing annihilation and release of a photon. Because the electron and hole now have additional energy from the THz drive, the released light has a higher frequency, satisfying equation 2.6. **b)** The real space trajectory during HSG. Step 1 corresponds to the creation of the electron-hole pair. Step 2 corresponds to the acceleration by the THz. Step 3 corresponds to recollision and release of a sideband photon. Different creation times will lead to different trajectories, and different orders of sideband corresponding to the energy the electrons and holes take from the THz. Higher order sidebands are accelerated for longer periods of time.

and we see that in the case of parabolic bands $\boldsymbol{k}$ acts like the momentum. We can shine a near-infrared laser (NIR) of frequency ω_{NIR} onto this semiconductor to excite electron-hole pairs. The NIR laser is sufficiently weak that the response is linear, and the electron-hole pairs do not feel any interactions from other pairs. Now imagine a strong terahertz (THz) laser of frequency ω_{THz} that is much lower frequency than the NIR. This laser cannot excite any electrons or holes to the other band, but is intense enough to act as a semiclassical electric field that accelerates the electrons and holes. In this case, the wave vector of the electrons and holes changes according to

$$\dot{\boldsymbol{k}}(t) = \frac{q}{\hbar}\boldsymbol{E}_{\text{THz}}(t) \tag{2.5}$$

where the dot denotes a time derivative, $\boldsymbol{E}_{\text{THz}}(t)$ is the electric field of the THz laser, and q is the charge of the electron or hole. For electrons $q = -e$ and for holes $q = +e$. As the electrons and holes gain $\boldsymbol{k}$ from the THz their velocity increases according to Eq. 2.4. However, the THz oscillates and in some cases the electrons and holes can be driven back together. During acceleration, the electron and hole can collide and annihilate with each other, releasing a photon. However, during this process both the electron and the hole have acquired nonzero $\boldsymbol{k}$ from the THz and therefore additional kinetic energy. When they annihilate, therefore, the photon is at higher energy and higher frequency than the NIR frequency. These photons at higher freqeuncies are called sidebands because they have energies of

$$\hbar\omega_n = \hbar\omega_{\text{NIR}} + n\hbar\omega_{\text{THz}} \tag{2.6}$$

where n is an integer called the sideband order. In systems with inversion symmetry, like the planes of GaAs probed by the experiments presented here, n must be even.

Not all electron-hole pairs created by the NIR recombine to create sidebands. Dephasing will cause some pairs to not produce sidebands, but pairs that are created at certain times with respect to the THz field will not recombine. Let the THz field be

$$\boldsymbol{E}_{\mathrm{THz}}(t) = \boldsymbol{F}\sin(\omega t) \tag{2.7}$$

where ω is the frequency of the THz and $\boldsymbol{F}$ is the polarization vector of the THz field with the magnitude of the maximum field strength. We have chosen a time convention such that the field evolves as a sin wave. Consider an electron-hole pair created at $t = 0$. The electron and hole will both be accelerated in one direction for a half THz period. The field will then switch sign and decelerate the particles. However, it will take the full half period of opposite field polarity to bring the particles to rest and they will never get closer to each other. In this situation, recombination and sideband production is impossible.

We require the electron and hole to start at position $\boldsymbol{x} = 0$ and velocity $\dot{\boldsymbol{x}} = 0$ The dynamics of electrons and holes in this electric field can be derived from the classical force equation for a charged particle,

$$\begin{aligned}
\ddot{\boldsymbol{x}} &= \frac{q\boldsymbol{F}}{m}\sin(\omega t)\\
\dot{\boldsymbol{x}} &= -\frac{q\boldsymbol{F}}{\omega m}\cos(\omega t) + \frac{q\boldsymbol{F}}{\omega m}\cos(\omega t_0)\\
\boldsymbol{x} &= -\frac{q\boldsymbol{F}}{\omega^2 m}\sin(\omega t) + \frac{q\boldsymbol{F}}{\omega m}\cos(\omega t_0)t + \frac{q\boldsymbol{F}}{\omega^2 m}\sin(\omega t_0)
\end{aligned} \tag{2.8}$$

where q is the charge of the particle, m is the mass of the particle, and t_0 is the creation time of the electron-hole pair.

In order to produce a sideband, a given electron-hole pair must satisfy two conditions. First, they must collide. Second the total kinetic energy of the pair must be equal to an allowed sideband energy from Eq. 2.6. It is convenient to work in the center of mass

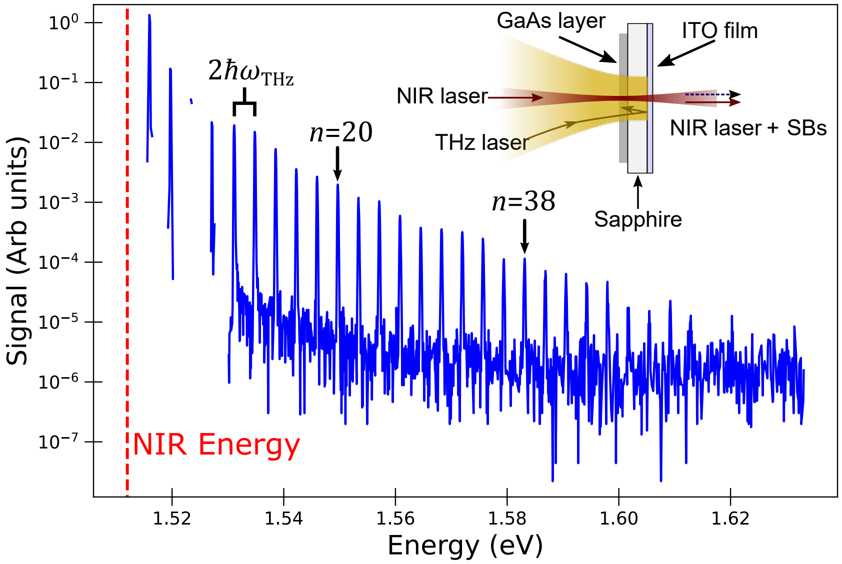

Figure 2.2: **High-order Sideband Spectrum in bulk GaAs.** A typical sideband spectrum, with sidebands from order $n = 2$ to $n = 54$ clearly visible. The energy of the NIR laser is demonstrated by the dotted red line. Sidebands are seperated by $2\hbar\omega_{\text{THz}}$ due to the inversion symmetry of the GaAs sample in the plane of THz acceleration. Sidebands decay with order due to the presence of dephasing, but only weakly. Inset, a demonstration of a typical sample in a GaAs HSG experiment. The NIR and THz lasers are coincident on the GaAs layer, which is mounted on a sapphire substrate. An indium tin oxide (ITO) film is grown on the backside of the sapphire substrate. ITO is transmissive to NIR, but reflective to THz. The NIR and sidebands transmit through the film, but the THz is reflected back. This creates an enhancement cavity for certain THz frequencies.

frame using the reduced mass of the electron-hole pair,

$$\frac{1}{\mu} = \frac{1}{m_c} + \frac{1}{m_h} \tag{2.9}$$

where μ is the reduced mass, m_c is the conduction band electron mass, and m_h is the hole mass. Replacing m_j with μ in Eq. 2.8 gives the separation distance. The first recombination condition requires that at the annihilation time t_f the separation is zero, so

$$\boldsymbol{x}(t_f) = -\frac{e\boldsymbol{F}}{\omega^2\mu}\sin(\omega t_f) + \frac{e\boldsymbol{F}}{\omega\mu}\cos(\omega t_0)t_f + \frac{e\boldsymbol{F}}{\omega^2\mu}\sin(\omega t_0) = 0. \tag{2.10}$$

We can equivalently state this that the integral of $\boldsymbol{k}$ over the lifetime is zero,

$$\int_{t_0}^{t_f} dt\boldsymbol{k}(t) = 0. \tag{2.11}$$

The kinetic energy of the electron-hole pair can be found by replacing the mass in Eq. 2.3 with the reduced mass. The energy condition is then

$$\frac{\hbar^2 k(t_f)^2}{2\mu} = n\hbar\omega \tag{2.12}$$

for a given sideband order n. Assuming that the reduced mass is known and that we have experimental control over the THz field strength and frequency, Eq. 2.12 and 2.10 give a system of two equations with two unknowns, t_0 and t_f. This means that there is one semiclassical trajectory that can produce a given sideband. This trajectory is shown in Fig. 2.1. Fig. 2.1 a) shows the momentum space trajectory, with the additional energy of the sideband shown by the difference in length of the NIR arrow (orange) and the final photon arrow (purple). The real space trajectory that can be obtained by solving Eq. 2.8 is shown in Fig. 2.1 b). In principle, there are additional trajectories that can take longer than one THz period, but the relatively strong dephasing heavily damps the contribution of these longer trajectories. Eq. 2.10 does not have an analytical solution, but the strong THz field strength used in experiments allows a linear treatment of the THz field to produce a good approximation of the creation time and annihilation time.

The process of sideband generation can be summarized as consisting of three steps, labelled in Fig. 2.1. First, the NIR excites an electron-hole pair. Second, the THz accelerates the electron and hole to higher energy. Third, the electron and hole recollide, annihilate, and produce a sideband.

Fig. 2.2 shows a typical sideband spectra with sidebands of order $n = 2$ to order $n = 54$ visible. The sideband peaks are spaced by $2\hbar\omega_{\mathrm{THz}}$. In HSG spectra like this there are many sidebands created, and the intensity of the sideband peaks decay weakly with order. Experiments in this work are usually limited to the 30th order, but in other works sidebands beyond order 120 have been observed [47] which is, to our knowledge the highest order nonlinear process in solids. This large number of peaks makes HSG a powerful probe of both real space and k space phenomena, with each order having its own trajectory through both spaces. The inset of Fig. 2.2 shows the macroscopic design of our samples. The GaAs layer is mounted on a sapphire substrate, with the NIR and THz lasers co-linearly focused on the GaAs.

2.2 The UCSB Free Electron Laser

Sideband generation is predicated on a strong source of THz radiation. The THz frequency range is ideal for HSG because the photon energy in the THz range is much less than 1 eV. The THz drive used in this work had a frequency of 450 GHz, which corresponds to a photon energy of 1.86 meV. These energies are much less than band gap of GaAs, which is about 1.51 eV at low temperature, which corresponds to 820 nm.

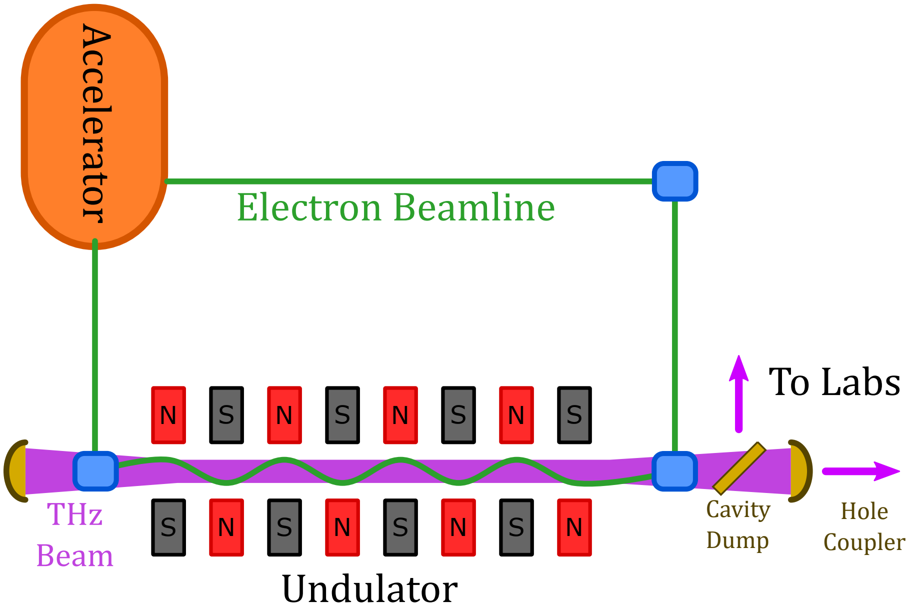

Figure 2.3: **The UCSB Free Electron Laser (FEL).** The FEL, which produces intense pulses of terahertz light. An electrostatic accelerator (orange) accelerates an electron beam with voltages up to 5 MV. The electron beam is steered around a beamline kept at ultra-high vacuum using electromagnetic components. The electron beam (green) is then focused in an undulator composed of aternating permanent magnets. These magnets cause the electrons to oscillate, releasing THz light (purple). The electrons are then steered back into the accelerator. Recirculation of the electron beam allows for longer electron pulses and therefore longer THz pulses. Two mirrors called end mirrors (gold) form the optical cavity from which the THz beam is excited. There are two modes that can be used in the FEL. The hole coupler features a small hole in one of the end mirrors which allows some of the THz to escape consistently over time. This produces long pulses of THz, up to several μs. The cavity dump features the insertion of a silicon wafer that is excited with an optical laser after lasing has been achieved in the cavity. Silicon is normally transparent to THz, but after being excited with green light it becomes reflective. This destroys the cavity but dumps all of the THz radiation in the cavity at once and produces a shorter pulse that has a very high peak intensity.

However, the THz range is high enough frequency to drive the electrons and holes quickly enough to avoid being completely lost to dephasing. This frequency range is necessary for HSG, but the THz must also be sufficiently intense to drive the electrons and holes. Achieving high intensity THz lasers is not an easy task as most laser technologies do not function well in the THz range. However, high intensity THz pulses can be created by using an instrument called a free electron laser (FEL).

The experiments in this work were performed at the University of California, Santa Barbara Free Electron Laser (UCSB FEL) [48, 47]. This instrument takes advantage of the fact that oscillating charge releases radiation. In materials, this can be used to produce low frequency radiation. However in materials it is difficult to oscillate charge above microwave frequencies. This difficulty is dealt with by oscillating free electrons, hence the name free electron laser. Maintaining a beam of free electrons requires ultra high vacuum for the beam line and very high voltage to accelerate the electron beam. The UCSB FEL can hold voltages up to 5 MV and can output frequencies from 200 GHz to 4.5 THz. The peak power of the UCSB FEL is around 100 kW.

During operation, a beam of electrons is accelerated to relativistic speeds by the accelerator at a repetition rate of 1.07 Hz. This beam is steered and shaped by electromagnets into an undulator, which is a group of alternating permanent magnets that cause the electrons to release radiation based on the spacing of the magnets. By changing the terminal voltage of the accelerator, the velocity of the electrons is changed and relativistic effects cause the effective spacing of the magnets to change, changing the frequency of light which is emitted. The undulator is placed in an optical cavity formed by two mirrors, and the light that is excited must be a multiple of the fundamental mode of the cavity. In our case, the fundamental mode is roughly 25 MHz. In practice, a small family of modes is excited by the oscillation of the electron beam but the linewidth of the beam is less than 1 GHz [47]. Shot to shot variation of the accelerator terminal voltage causes the center frequency of the beam to jump around, but this variation is on the order of 1 GHz. The experiments we performed here were done at 450 GHz, so this variation is quite small.

This narrow linewidth implies another strength of the FEL, which is long pulses. There are two methods of coupling out the light from the optical cavity, and they give different pulse lengths. The first is to use a hole coupler, where one of the end mirrors of the optical cavity has a small hole in it, which allows a small amount of light in the cavity to leave and be directed into the laboratory. The second method is to use a cavity dump system. In this system, a silicon wafer mounted at Brewster's angle is inserted into the optical cavity. Silicon is very nearly totally transparent to the THz so the radiation builds up until a green laser is used to excite carriers in the silicon. At this point the silicon becomes reflective, as the free carriers in the wafer act as a metal. This destroys the cavity, but dumps all the radiation out over 40 ns, the round trip time for light in the cavity. The hole coupler produces long pulses of several μs that can be lengthened by lengthening the electron pulse. The cavity dump always produces 40 ns of THz light, but the field strength is much higher. In our experiments, typical field strengths were 70 kV/cm. Fig. 2.3 shows a cartoon of the FEL.

2.3 Quantum Interference and Sideband Polarization

The three step process we have described in section 2.1 is a good description of HSG when there are two bands involved with sideband generation. However, as we described in section 1.4 in GaAs there are three relevant bands, the electron (E) conduction band, the heavy hole (HH) band, and the light hole (LH) band. In this case, both E-HH and

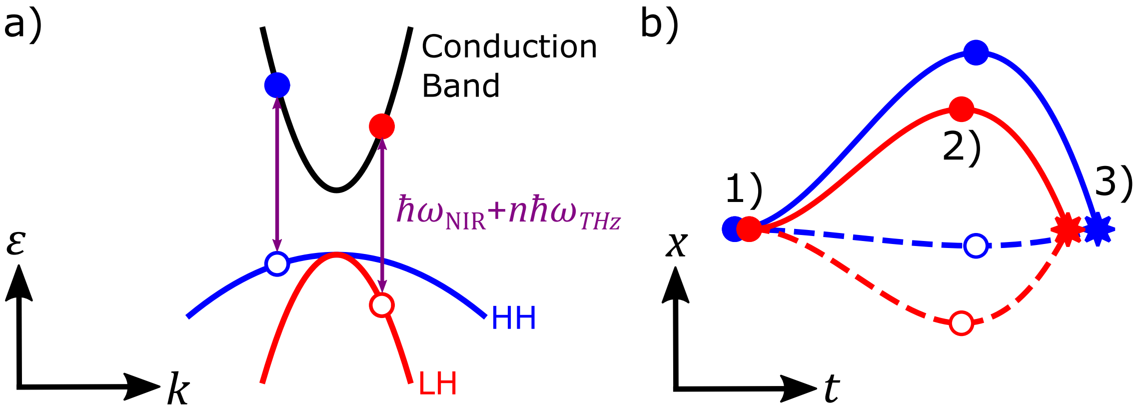

Figure 2.4: **Quantum Interference in HSG. a)** The band structure of GaAs during HSG. Since GaAs has two valence bands that are degenerate at the gap, two types of electron-hole pair can be formed, an electron-heavy hole pair (E-HH) and an electron–light hole pair (E-LH). Electrons are shown with solid circles and holes are shown as circles with an empty center. Both of these electron-hole pairs can contribute to the same sideband order, but have different trajectories. In $\boldsymbol{k}$ space, the different pairs can collide at different points, but have the same energy. This is shown by the purple arrows which are the same length for the E-HH and E-LH pairs. **b)** The real space trajectories of the two electron-hole pairs that can contribute to the same sideband. Each step of HSG is different for the E-HH pair (blue) and E-LH pair (red). The two pairs are created at different times, experience different real space trajectories due to the difference in reduced mass, and recollide at different times. This difference leads to different dynamical phases being accumulated during acceleration, which interfere when the two contributions combine to form the final sideband.

E-LH pairs can contribute to a given sideband. Fig. 2.4 a) shows the Luttinger band structure with both an E-HH pair and an E-LH pair producing sidebands of the same energy. However, the dynamics of these pairs are different due to the difference between the effective mass of the heavy and light holes.

Consider two electron-hole pairs, one E-LH and one E-HH. Due to the difference in reduced mass, the solutions to Eq. 2.10 and 2.12 will be different and the pairs will be created and destroyed at different times. The different real space trajectories, including different creation and recombination times is shown in Fig. 2.4 b). These differences combined with the different dispersion relations means that the dynamical phase acquired by these different pairs is different. Assuming that the bands are quadratic, the dynamical phase is,

$$A_j = \int_{t_{0,j}}^{t_{f,j}} \varepsilon_j(t)dt = \int_{t_{0,j}}^{t_{f,j}} \frac{\hbar^2 k(t)^2}{2\mu}dt \tag{2.13}$$

where j refers to either E-HH or E-LH pairs. Therefore, after both pairs have annihilated to create a sideband the two contributions interfere because of the difference between the phases they have accumulated. However, this does not manifest as an interference of intensity because the different hole states have different angular momenta. The total angular momentum of an electron-hole pair that annihilates to create a photon is reflected in the polarization state of that photon [45, 46].

We will work in a circular basis for light, with the state σ_+ corresponding to right handed circular light and angular momentum +1 and the state σ_- corresponding to left handed circular light and angular momentum -1. The electron can be either spin up $|\uparrow\rangle$ or spin down $|\downarrow\rangle$. The HH and LH states are superpositions of the $J = 3/2$ states in Eq. 1.89. Because all of these states have $J = 3/2$, we label the basis of hole states only with

m_J and the four relevant states are

$$\begin{aligned} &\left|+3/2\right\rangle \\ &\left|+1/2\right\rangle \\ &\left|-1/2\right\rangle \\ &\left|-3/2\right\rangle . \end{aligned} \tag{2.14}$$

Let us consider a single photon in the σ_+ state. This photon can excite either a $|\uparrow\rangle$ electron and a hole in the $|+1/2\rangle$ state or a $|\downarrow\rangle$ electron and a hole in the $|+3/2\rangle$ state. For a σ_- photon the possibilities are a $|\uparrow\rangle$ electron and a hole in the $|-3/2\rangle$ state or a $|\downarrow\rangle$ electron and a hole in the $|-1/2\rangle$ state. These possibilities have opposite angular momentum, which corresponds to the time reversal symmetry of the system. The HH and LH states are not angular momentum eigenstates and so the holes are excited into superpositions of both heavy and light holes. During acceleration the holes acquire a relative phase between them and after recombination the light will no longer be σ_+. For different sideband orders the phase difference is different and thus the final polarization state will depend on sideband order. Therefore, the polarization state of the sideband is set by a quantum interference of the E-HH and E-LH pairs.

Fig. 2.5 demonstrates how sideband polarization changes based on sideband order. Four linear ($\gamma = 0°$ NIR polarizations were used to produce sidebands, $\alpha = 90°$ (red diamonds), $\alpha = 45°$ (yellow triangles), $\alpha = 0°$ (blue circles), and $\alpha = -45°$ (green squares). Both α and γ vary as a function of sideband order and none of the sidebands have the same polarization as the NIR lasers. Instead the polarization state evolves as a function of sideband order as the phase differences between the E-HH pair and E-LH pair increase. The change in polarization is more pronounced for polarizations that are not parallel or perpendicular to the THz polarization.

Since σ_+ and σ_- form a complete basis, any input polarization state can be described as a linear combination of these two states. Therefore, if we understand sideband gen-

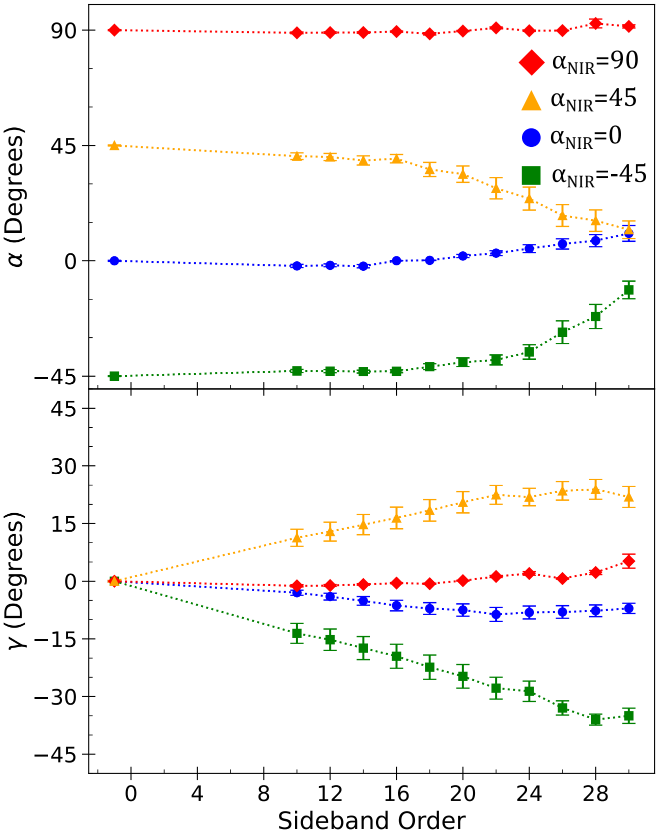

Figure 2.5: **Sideband Polarization.** The polarization states of sidebands of order $n = 10$ to order $n = 30$ for four starting NIR polarizations ($n = 0$). Both the linear orientation angle α (upper) and the ellipticity angle γ (lower) are shown. The four NIR polarizations are all linear ($\gamma = 0°$), with $\alpha = 90°$ (red diamonds), $\alpha = 45°$ (yellow triangles), $\alpha = 0°$ (blue circles), and $\alpha = -45°$ (green squares). $\alpha = 0°$ corresponds to the THz polarization direction. The sideband polarization depends on both the NIR polarization and the sideband order. This data was taken with $\omega_{\mathrm{THz}} = 449 \pm 1$ GHz, $\lambda_{\mathrm{NIR}} = 820$ nm and THz field strength of 65 ± 3 kV/cm.

eration when the NIR laser is polarized with σ_+, and σ_-, we can understand sidebands made by any NIR polarization by treating that process as a linear combination of sideband generation from σ_+ and σ_-.

By measuring the polarization of the sidebands, we detect the interference of the E-HH and E-LH contributions. By changing experimental parameters such as field strength, $\boldsymbol{k}$ space trajectory, and effective mass we can attempt to extract information about the dynamical phase from the sideband spectra. In this way, polarimetry of high-order sidebands acts as a Bloch wave interferometer.

2.4 Stokes Polarimetry of Sidebands and Jones Calculus

In order to learn anything about the quantum interference occuring in HSG, it is necessary to measure the polarization of sidebands. It is not sufficient to simply measure the sidebands with a polarizer, because we want to know both the linear orientation angle α and the ellipticity γ in order to understand the interference between the E-HH and E-LH pairs.

We use a method called Stokes polarimetry to measure the sideband polarizations. This method consists of measuring the light of interest after a quarter wave plate (QWP) and a polarizer. The polarizer stays put while the QWP rotates. A QWP has a fast axis and a perpendicular slow axis. The light that is polarized along the slow axis gains a retardance of $\pi/2$ which corresponds to $\lambda/4$ hence the name quarter wave plate. For example consider incoming light that is polarized linearly with $\alpha = 45°$ and passes through a QWP with a fast axis that is horizontal ($\alpha = 0°$). The vertical component of the light will gain a $\pi/2$ phase delay compared with the horizontal component and

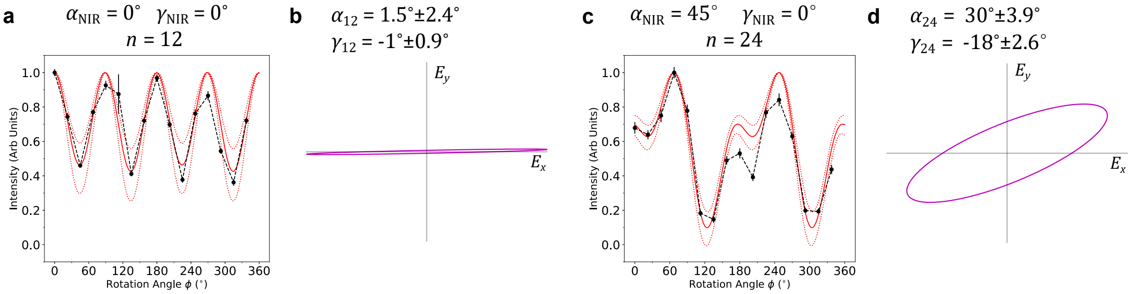

Figure 2.6: **Stokes Polarimetry.** **a)** Intensity as a function of quarter wave plate (QWP) angle. Block dots with dashed lines represent the measured intensity, with the solid line representing the extracted polarization state and the dotted red lines representing the range of uncertainty. This data is normalized to the highest measured sideband signal and comes from a $n = 12$ sideband with horizontally polarized NIR ($\alpha = 0°$). **b)** The extracted sideband state from **a)** using Eq. 2.17. **c)-d)** The same as **a)-b)** but with the NIR polarized diagonally ($\alpha = 45°$) and the data taken from the $n = 24$ sideband.

the light will change from diagonal to circularly polarized. The polarizer in the Stokes polarimeter stays fixed so we always measure the intensity along the horizontal direction. By changing the QWP angle and measuring the intensity after the polarizer we can extract the full polarization state.

Mathematically, we use the formalism of Stokes parameters. We use four dimensional matrices called Mueller matrices to calculate how the rotating QWP and polarizer change the incoming polarization [18]. Solving this equation gives the outgoing intensity as a function of the Stokes parameters of the incoming light beam,

$$S_{\mathrm{out}} = \frac{S_0}{2} + \frac{S_1}{4} - \frac{S_3}{2}\sin(2\phi) + \frac{S_1}{4}\cos(4\phi) + \frac{S_2}{4}\sin(4\phi) \tag{2.15}$$

where S_{out} is the intensity measured after the polarimeter, $S_{0,1,2,3}$ are the Stokes parameters of the incoming light beam, and ϕ is the angle betwen the QWP fast axis and the horizontal direction. The different sin and cos terms with different frequencies make Fourier analysis ideal for extracting the Stokes parameters. Consider the Fourier transform of S_{out},

$$\mathcal{F}_n = \int_0^{2\pi} S_{\text{out}}(\phi)\frac{e^{in\phi}}{2\pi}d\phi \tag{2.16}$$

where n is an integer. The Stokes parameters of the incoming light are then

$$\begin{aligned} S_0 &= 2\mathcal{F}_0 - 4\text{Re}(\mathcal{F}_4) \\ S_1 &= 8\text{Re}(\mathcal{F}_4) \\ S_2 &= -8\text{Im}(\mathcal{F}_4) \\ S_3 &= 4\text{Im}(\mathcal{F}_2) \end{aligned} \tag{2.17}$$

where $\text{Re}(\mathcal{F}_n)$ and $\text{Im}(\mathcal{F}_n)$ correspond to the real and imaginary part of $\mathcal{F}_n$. Once we have the Stokes parameters we can calculate the α and γ of each sideband from Eq. 1.23.

Experimentally, we use an Andor electron multiplying charged coupled device (EM-CCD or CCD). This detector can measure many wavelengths at once, and shows a total number of counts over a set integration time at each wavelength. This allows multiple sideband peaks to be measured simultaneously. We rotate the QWP in steps of 22.5° from $\phi = 0°$ to $\phi = 337.5°$ and take four CCD images at each rotator angle for uncertainty analysis. In theory, rotating the QWP by 180° gives the same polarization but we take more points as a further method to define errors and protect against data outliers.

Fig. 2.6 shows two example sets of Stokes polarimetry data. Fig. 2.6 a) and c) show the measured intensity of the relevant sideband as a function of QWP angle, ϕ, and the extracted polarization states of the sidebands are shown as purple ellipses in Fig. 2.6 b) and d). The intensity as a function of ϕ is called a polaragram. The black dots and dashed lines correspond to the measured data. The solid red line corresponds to the expected intensity of the extracted polarization state, while the dotted red lines correspond to the range of intensity expected within the confidence intervals stated in Fig. 2.6 b) and d). The different shapes of the polaragrams in Fig. 2.6 are caused by the differences in sideband polarization. The 180° symmetry of the QWP means polaragrams will always have an expected 180° rotational symmetry, but linear polarizations will have a 90° rotational symmetry as well. The data in Fig. 2.6 a) is very close to linear polarization and thus almost has the four-fold symmetry. Conversely, the data in Fig. 2.6 d) is much more elliptical and therefore the data clearly has no four-fold symmetry.

The CCD cannot be used to measure sidebands that are very close to the NIR laser line ($n < 6$) because the sidebands are significantly weaker than the laser line and the detector will be saturated before the sideband signal can be detected. For measuring the laser line or the low order sidebands, we use a photo-multiplier tube (PMT). The PMT is a time sensitive measurement, which can make it useful for alignment purposes, but each measurement is only of a very small frequency range. This makes sideband measurements very slow, as several measurements are necessary to detect one sideband. For this reason, we do not generally perform Stokes polarimetry with the PMT. When measuring sideband spectra where low orders we measure several sidebands with both detectors to stitch the two measurements together.

2.4.1 Jones Calculus

Using Stokes polarimetry we are able to measure the polarization of any sidebands we produce. It is important to note that the polarization state of the sidebands depends on sideband order, but also on the polarization of the NIR laser that creates the electron-hole pairs in the first place. Intuitively, the polarization changes more from the NIR state as sideband order increases. In order to characterize the quantum interference process independent of the NIR polarization, we employ a mathematical tool called the Jones calculus.

We recall from section 1.1.2 that the polarization state of light can be represented by a two dimensional complex vector. We now introduce a 2x2 complex matrix called a Jones matrix that can model any process that changes polarization. The process that produces the nth order sideband is modeled as a matrix $\mathcal{T}_n$ that satisfies the equation,

$$\boldsymbol{E}_n = \mathcal{T}_n \boldsymbol{E}_{\text{NIR}} \tag{2.18}$$

where $\boldsymbol{E}_n$ is the polarization vector of the nth sideband and $\boldsymbol{E}_{\text{NIR}}$ is the polarization vector of the NIR laser. These polarization vectors are called Jones vectors. The Jones matrix $\mathcal{T}_n$ is called the dynamical Jones matrix [45]. We work in a circular basis, so the matrix form of Eq. 2.18 is

$$\begin{pmatrix} E_+ \\ E_- \end{pmatrix}_n = \begin{pmatrix} T_{++} & T_{+-} \\ T_{-+} & T_{--} \end{pmatrix}_n \begin{pmatrix} E_+ \\ E_- \end{pmatrix}_{\text{NIR}} \tag{2.19}$$

where $E_{+(-)}$ is the amount of right handed (left handed) light. The elements of $\mathcal{T}_n$ are complex numbers so it in general has 8 free parameters. We work with normalized Jones vectors, so the dynamical Jones matrix is only defined up to an overall complex number. This means that we can always define our Jones matrix to satisfy the constraint $T_{++} = 1$ and the matrix can be completely defined by 6 parameters. In order to extract $\mathcal{T}_n$ we measure sideband polarizations for 4 different NIR polarizations, with each sideband measurement giving us 2 independent pieces of information, α and γ. We are able to freely set the NIR polarization incident on the sample using a QWP and a half wave plate (HWP). Since there are only 6 free parameters that define the Jones matrix we could measure $\mathcal{T}_n$ by measuring the sideband spectra produced by 3 different NIR polarizations, but we measure 4 polarizations to reduce error.

Once we have measusured the sideband polarization for 4 different NIR polarizations, we solve Eq. 2.18. With $\mathcal{T}_n$ we are able to predict the sideband polarization for any

NIR polarization. This means that all the information about the physics occuring in the material during HSG, including the quantum interference, is contained in the elements of $\mathcal{T}_n$. The next step is to connect these elements to quantities of interest in the material so we can extract information from our interferometer. It is important to note that experimental parameters such as THz field strength, THz frequency, and crystal orientation can change $\mathcal{T}_n$ since they change the sideband generation process, and we must always view the dynamical Jones matrix as being linked to a particular set of microscopic processes.

2.5 Reconstructing Bloch Wavefunctions via Sideband Polarimetry

In order to extract information from the Bloch wave interference present in HSG, it is helpful to design experiments in such a way as to simplify the underlying physics. We will consider experiments for bulk GaAs where the NIR and THz are incident normal to the (001) plane. If we are careful to excite at the band gap, which in GaAs is at the $\boldsymbol{k} = 0$ point, then both the NIR and THz will propagate along the k_z direction and the electron-hole pairs will be driven in the $k_x - k_y$ plane. In this case $k_z = 0$ for the entire acceleration process and the Luttinger Hamiltonian reduces to two block diagonal two dimensional Hamiltonians,

$$H_{\pm}(\boldsymbol{k}) = -\frac{\hbar^2 k^2}{2m_0}(\gamma_1 - 2\gamma_2 \boldsymbol{n}_{\pm} \cdot \boldsymbol{\tau}) \tag{2.20}$$

where $\boldsymbol{\tau}$ is the vector of spin 1/2 Pauli matrices and $\boldsymbol{n}_{\pm}$ is a three dimensional vector,

$$\boldsymbol{n}_{\pm} = \left(\frac{\sqrt{3}}{2} \sin(2\theta), \mp \frac{\sqrt{3}\gamma_3}{2\gamma_2} \cos(2\theta), -\frac{1}{2} \right) \tag{2.21}$$

where θ is the angle between the THz field and the [110] crystal direction. In matrix form, the Hamiltonian is

$$H_\pm(\boldsymbol{k}) = -\frac{\hbar^2 k^2}{2m_0} \begin{pmatrix} \gamma_1 + \gamma_2 & -\sqrt{3}(\gamma_2 \sin(2\theta) \pm i\gamma_3 \cos(2\theta)) \\ -\sqrt{3}(\gamma_2 \sin(2\theta) \mp i\gamma_3 \cos(2\theta)) & \gamma_1 - \gamma_2 \end{pmatrix}. \tag{2.22}$$

The H_- block couples together the $|+3/2\rangle$ and $|-1/2\rangle$ states and the H_+ block couples the $|+1/2\rangle$ and $|-3/2\rangle$ states. The eigenfunctions of each block correspond to one HH and one LH with the spin partnered state existing in the opposite block. The energies of each block are the same, with

$$\begin{aligned} \varepsilon_{HH}(\boldsymbol{k}) &= -\frac{\hbar^2 k^2}{2m_0}(\gamma_1 - 2\gamma_2|\boldsymbol{n}_\pm|) \\ \varepsilon_{LH}(\boldsymbol{k}) &= -\frac{\hbar^2 k^2}{2m_0}(\gamma_1 + 2\gamma_2|\boldsymbol{n}_\pm|). \end{aligned} \tag{2.23}$$

The magnitude $|\boldsymbol{n}_\pm|$ is the same for both the + and − term, since only the sign of the second component changes. From this, we can define the effective mass of the HH and LH as,

$$\begin{aligned} m_{\mathrm{HH}} &= \frac{m_0}{\gamma_1 - 2\gamma_2|\boldsymbol{n}_\pm|} \\ m_{\mathrm{LH}} &= \frac{m_0}{\gamma_1 + 2\gamma_2|\boldsymbol{n}_\pm|}. \end{aligned} \tag{2.24}$$

From this result, we see that the effective mass of the heavy and light holes depends on the Luttinger parameters, but also the crystal angle θ. It does not, however, depend on the magnitude of $\boldsymbol{k}$.

An important feature of Eq. 2.20 is that if we assume the THz is linearly polarized such that θ is constant for the acceleration process, then the Hamiltonian can be diagonalized if the value of γ_3/γ_2 is known. This is because the second term can be diagonalized if $\boldsymbol{n}_{\pm}$ is known and $\boldsymbol{n}_{\pm}$ is totally defined by θ and γ_3/γ_2. Since the first term is proportional to the identity matrix, if the second term is diagonalized, then the first term is also diagonalized. In this way, if we can extract γ_3/γ_2 from sideband spectra, then we can reconstruct the form of the Bloch wavefunctions.

2.5.1 Connecting Theory with Jones Matrices

In order to connect the experimentally extracted Jones matrices to theory, we need to connect the electric field of the NIR to the interband polarization vector $\mathbb{P}$. Since we are interested in the polarization of particular sidebands, we can take the Fourier transform of $\mathbb{P}$ at the frequency of a given sideband. This Fourier component $\mathbb{P}_n$ is

$$\mathbb{P}_n = \frac{1}{d^2} \sum_{s=\pm} \mathbb{D}_s^\dagger R_s \begin{pmatrix} \varsigma_{\mathrm{HH},n} & 0 \\ 0 & \varsigma_{\mathrm{LH},n} \end{pmatrix} R_s^\dagger \mathbb{D}_s \cdot \boldsymbol{E}_{\mathrm{NIR}} \tag{2.25}$$

where s is an index that iterates over the $+$ and $-$ terms of the Hamiltonian in Eq. 2.20, d is the dipole coupling coefficient of the system $d = -\langle s| e\hat{x} |X\rangle$, R_s is a rotation matrix that diagonalizes the Hamiltonian, $\boldsymbol{E}_{\mathrm{NIR}}$ is the electric field of the NIR without the oscillating term, $\varsigma_{\mathrm{HH(LH)},n}$ is the E-HH (E-LH) contribution to the sideband,and $\mathbb{D}_s = (D_1, D_2, ..., D_8)$ is the set of dipole vectors for the eight possible interband couplings

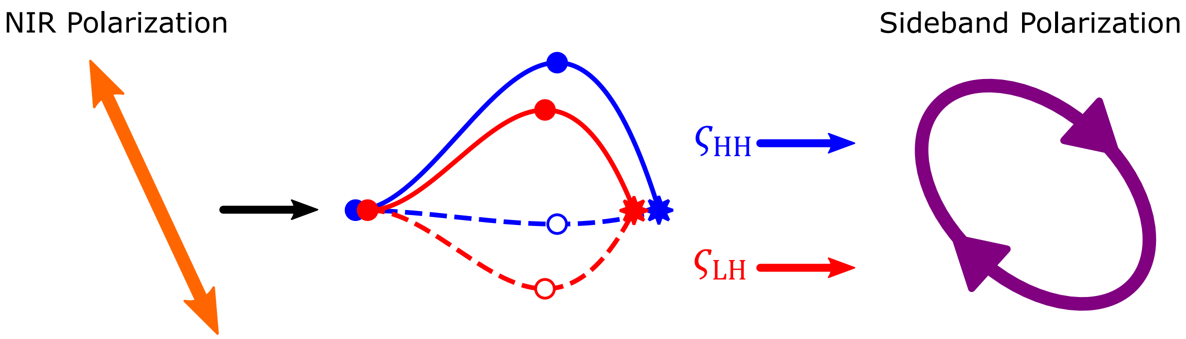

Figure 2.7: **Polarization change from quantum interference.** A NIR photon with linear polarization creates E-HH and E-LH pairs that are then accelerated by the THz, acquiring different dynamical phases. After recollision, the E-HH contributes ς_{HH} to the sideband and the E-LH contributes ς_{LH} to the sideband. These two contributions have different angular momenta, magnitudes, and relative phases which causes elliptical sideband polarization.

of electron and hole states [46]. These eight states and the dipole couplings are

$$\begin{aligned}
|u_1\rangle &= |\uparrow\rangle\,|+3/2\rangle \rightarrow D_1 = 0\\
|u_2\rangle &= |\downarrow\rangle\,|+3/2\rangle \rightarrow D_2 = -d\sigma_+\\
|u_3\rangle &= |\uparrow\rangle\,|+1/2\rangle \rightarrow D_3 = -d\sigma_+/\sqrt{3}\\
|u_4\rangle &= |\downarrow\rangle\,|+1/2\rangle \rightarrow D_4 = 0\\
|u_5\rangle &= |\uparrow\rangle\,|-1/2\rangle \rightarrow D_5 = 0\\
|u_6\rangle &= |\downarrow\rangle\,|-1/2\rangle \rightarrow D_6 = -d\sigma_-/\sqrt{3}\\
|u_7\rangle &= |\uparrow\rangle\,|-3/2\rangle \rightarrow D_7 = -d\sigma_-\\
|u_8\rangle &= |\downarrow\rangle\,|-3/2\rangle \rightarrow D_8 = 0
\end{aligned} \tag{2.26}$$

where states that have total angular momentum +1 are coupled by σ_+ photons and the states that have total angular momentum −1 are coupled by σ_- photons. States that have total angular momentum not equal to ±1 are not coupled by the NIR laser.

The $\mathbb{D}_s \cdot \boldsymbol{E}_{\mathrm{NIR}}$ part of Eq. 2.25 couples the NIR laser to electron-hole pairs that are angular momentum eigenstates ($|u_{1-8}\rangle$). These states are then rotated by $R_s^\dagger$ to the HH-LH basis. In this basis the holes have definite trajectories in $\boldsymbol{k}$ space and the $\varsigma_{\mathrm{HH(LH)},n}$ describe the evolution that occurs during acceleration. The R_s then converts the final collection of electrons and holes back to the angular momentum basis, and $\mathbb{D}_s^\dagger$ couples the electrons and holes to outgoing light which is now a sideband. The propagators $\varsigma_{\mathrm{HH,LH},n}$ are defined as

$$\varsigma_{j,n} = \frac{i\omega d^2}{2\pi V\hbar}\int_0^{2\pi/\omega} dt e^{i(\Omega+n\omega)t}\int_{-\infty}^{t} dt' e^{iA_j(t',t)-\mathcal{G}_j(t',t)}e^{-i\Omega t'} \tag{2.27}$$

where Ω is the frequency of the NIR laser, ω is the frequency of the THz, V is the volume of crystal involved with HSG, j is an index that can refer to HH or LH, $\mathcal{G}_j(t',t)$ is the dephasing accumulated for the E-HH or E-LH pair between t' and t (see Eq. 1.81), and $A_j(t',t)$ is the dynamical phase acquired between t' and t. In this case, the dynamical phase is

$$A_j(t',t) = -\frac{1}{\hbar}\int_{t'}^{t} dt'' \left[\varepsilon_c(\boldsymbol{k}(t'')) - \varepsilon_j(\boldsymbol{k}(t''))\right] \tag{2.28}$$

where $\varepsilon_c(\boldsymbol{k})$ is the energy of the conduction band electron and $\varepsilon_j(\boldsymbol{k})$ is the energy of the HH or LH. Since we have parabolic bands, we can write the energy of the electron-hole pair as

$$\varepsilon_c(\boldsymbol{k}) - \varepsilon_j(\boldsymbol{k}) = \frac{\hbar^2k^2}{2\mu_j(\boldsymbol{k})}. \tag{2.29}$$

The rightmost integral in Eq. 2.27 integrates the contributions of electron-hole pairs created at different times t'. The leftomost integral is the Fourier transformation which selects for the nth order sideband.

Fig. 2.7 shows schematically how the change in polarization of sidebands arises from Eq. 2.25. The NIR, polarized linearly, excites E-HH and E-LH pairs. During acceleration each pair accumulates different $A_j(t',t)$ which is encoded in $\varsigma_{j,n}$. After recollison, the contributions of the HH, corresponding to $\varsigma_{\mathrm{HH},n}$, and the contributions of the LH, corresponding to $\varsigma_{\mathrm{LH},n}$, combine to form the sideband. Because $\varsigma_{\mathrm{HH},n}$ and $\varsigma_{\mathrm{LH},n}$ interfere, their relative magnitude and phase determine the polarization of the sideband.

The matrix that we defined in Eq. 2.25 is in fact the Jones matrix, for the nth order sideband since it maps $\boldsymbol{E}_{\mathrm{NIR}}$ to the sideband polarization. From this, we can write the elements of the Jones matrix in terms we have defined here. Algebraic manipulation of Eq. 2.25 yields,

$$\begin{aligned} T_{++,n} &= \frac{2}{3}(\varsigma_{\mathrm{HH},n} + \varsigma_{\mathrm{LH},n}) + \frac{\tilde{n}_z}{3}(\varsigma_{\mathrm{HH},n} - \varsigma_{\mathrm{LH},n}) \\ T_{+-,n} &= \frac{\tilde{n}_x + i\tilde{n}_y}{3}(\varsigma_{\mathrm{HH},n} - \varsigma_{\mathrm{LH},n}) \\ T_{-+,n} &= \frac{\tilde{n}_x - i\tilde{n}_y}{3}(\varsigma_{\mathrm{HH},n} - \varsigma_{\mathrm{LH},n}) \\ T_{--,n} &= \frac{2}{3}(\varsigma_{\mathrm{HH},n} + \varsigma_{\mathrm{LH},n}) + \frac{\tilde{n}_z}{3}(\varsigma_{\mathrm{HH},n} - \varsigma_{\mathrm{LH},n}) \end{aligned} \tag{2.30}$$

where $\tilde{n}_{x,y,z}$ are the elements of the normalized vector $\tilde{\boldsymbol{n}} = \boldsymbol{n}_+/|\boldsymbol{n}_+| = (\tilde{n}_x, \tilde{n}_y, \tilde{n}_z)$. The precise values of the $\varsigma_{j,n}$ can be difficult to calculate since they depend on various constants that are not necessarily well known. To simplify the comparison between experiment and theory, we take ratios of the Jones matrix elements,

$$\begin{aligned} \frac{T_{++,n}}{T_{--,n}} &= 1 \equiv \xi_n(\theta) \\ \frac{T_{+-,n}}{T_{-+,n}} &= \frac{\tilde{n}_x + i\tilde{n}_y}{\tilde{n}_x - i\tilde{n}_y} = \frac{\gamma_2 \sin(2\theta) - i\gamma_3 \cos(2\theta)}{\gamma_2 \sin(2\theta) + \gamma_3 \cos(2\theta)} \equiv \chi_n(\theta). \end{aligned} \tag{2.31}$$

We note that these ratios are constant with respect to sideband order. The ratio of diagonal components $\xi_n(\theta)$ is one, which is a reflection of the time reversal symmetry of the system. For every process that starts with right handed circular light and ends with right handed circular light, there is an equivalent process that starts and ends with left handed circular light. In contrast, the ratio of off-diagonal components $\chi_n(\theta)$ depends on

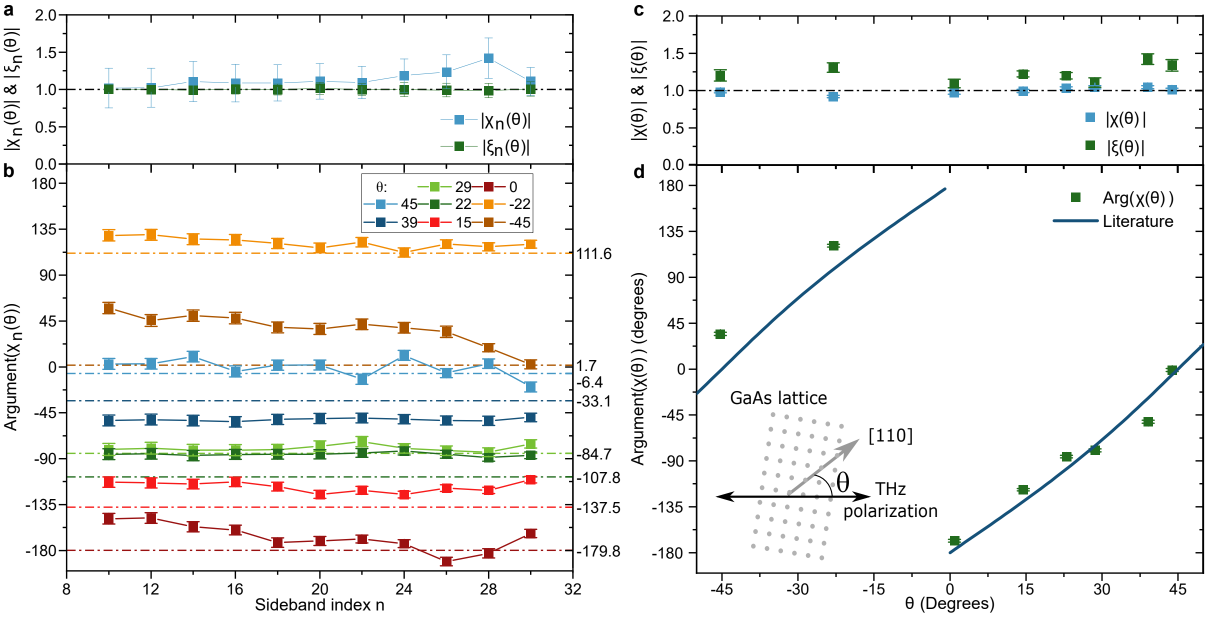

Figure 2.8: **Jones Matrix Ratios. a)** The magnitude of $\chi_n(\theta) = T_{++,n}/T_{--,n}$ and $\xi_n(\theta) = T_{+-,n}/T_{-+,n}$ as a function of sideband order for $\theta = 39°$. From Eq. 2.31 we expect the magnitude to be 1 for all sideband orders (dash dot lines). **b)** The argument of $\chi_n(\theta)$ as a function of sideband order for different θ. According to Eq. 2.31 we expect the argument of $\chi_n(\theta)$ to be constant in sideband order but vary for different θ. Dash dot lines correspond to the expected argument using literature values of γ_3/γ_2 [49]. The numerical value of this expected value is displayed on the right axis. **c)** The magnitude of $\chi_n(\theta)$ and $\xi_n(\theta)$ as a function of θ. These values are calculated by averaging the magnitude of $\chi_n(\theta)$ and $\xi_n(\theta)$ over n at each θ, with the errorbars corresponding to the standard deviation corresponding to this average. We again expect these magnitudes to be 1, which is marked with a dash dot line. **d)** The argument of $\chi_n(\theta)$ as a function of θ, averaged over n at each angle. The blue line shows the expected argument using the literature values of Luttinger parameters used in **b)**. At each θ, we can use the average value of $\text{Arg}(\chi_n(\theta))$ to extract γ_3/γ_2 using Eq. 2.31. Inset: the definition of θ, the angle between the THz polarization and the [100] direction of the GaAs crystal lattice.

the crystal angle and the ratio γ_3/γ_2. Because the numerator and denominator of $\chi_n(\theta)$ are complex conjugates of each other, the magnitude of $\chi_n(\theta)$ is 1 and the information about θ and γ_3/γ_2 is contained in the complex argument of $\chi_n(\theta)$.

Experimentally, we rotate the crystal and measure the polarization enough times to extract the dynamical Jones matrix at each crystal angle. We can accurately measure θ by taking photos of the GaAs sample. The sample has flat edges that correspond to known crystal directions which allow straightforward measurement. This means that the only unknown parameter of $\mathrm{Arg}(\chi_n(\theta))$ is γ_3/γ_2.

Fig. 2.8 shows the Jones matrix ratios $T_{++,n}/T_{--,n} = \xi_n(\theta)$ and $T_{+-,n}/T_{-+,n} = \chi_n(\theta)$ for 8 different values of θ. Fig. 2.8 a) shows the magnitude $|\xi_n(\theta)|$ and $|\chi_n(\theta)|$ for one value of θ. For all orders, these magnitudes are close to 1, as we expect. Fig. 2.8 b) shows the argument $\mathrm{Arg}(\chi_n(\theta))$ for 8 different values of θ. The dash dot lines correspond to the expected argument using literature values of $\gamma_3/\gamma_2 = 1.45$ [49]. At most angles, the measured argument does not change much with sideband order. Some angles are quite close to the literature expectation, but others do not seem to agree with the literature. At each angle, we average $\xi_n(\theta)$ and $\chi_n(\theta)$ over sideband order to get one value for the magnitude and argument of each ratio at each angle. Fig. 2.8 c) shows this averaged magnitude as a function of θ.The averaged values for both $|\xi_n(\theta)|$ and $|\chi_n(\theta)|$ are close to the expected value of 1. Fig. 2.8 d) shows the $\mathrm{Arg}(\chi_n(\theta))$ as a function of θ along with the literature expectation in blue. The data follows a similar shape to the literature prediction, but does not lie exactly on the curve. Following Eq. 2.31 we can extract a value of γ_3/γ_2 at each value of θ. We ignore data sets where $\sin(2\theta)$ or $\cos(2\theta)$ is equal to zero since these angles are not sensitive to γ_3/γ_2. Averaging over our data, we extract a value $\gamma_3/\gamma_2 = 1.47 \pm 0.48$ [46]. With this we are able to reconstruct the Bloch wavefunctions for the HH and LH states by diagonalizing Eq. 2.20.

Fig. 2.9 shows the reconstructed Bloch wavefunctions of the HH and LH states associated with the $\hat{H}_+$ block of the Hamiltonian in Eq. 2.20 on a Bloch sphere. These wavefunctions are superpositions of the $|-3/2\rangle$ state and the $|+1/2\rangle$ state. At each crystal angle, the HH and LH are described by one point on the Bloch sphere. The black lines correspond to all possible forms of the HH or LH wavefunction in the $k_z =$ 0 plane. Colored arrows point out particular forms of the wavefunction at particular values of θ corresponding to the Miller indices in the lower right. The orange band corresponds to the uncertainty in the wavefunction associated with the uncertainty in γ_3/γ_2. The wavefunctions for $\hat{H}_-$ are the same paths, reflected across the $x - z$ plane and are superpositions of the $|+3/2\rangle$ state and the $|-1/2\rangle$ state.

2.6 Conclusion

High-order sideband generation is promising as a way to overcome the inherent difficulties of building interferometers in solid crystals. Measuring the changing polarization of sidebands gives direct experimental access to the interference of different electron-hole pairs and the information contained in the phases of these wavefunctions.

Here, we have used the interference of the dynamical phase to extract γ_3/γ_2 and used this to reconstruct the Bloch wavefunctions. Previous methods to reconstruct the Bloch wavefunctions typically depend on parameters derived from fits of complex models [50, 49] to a few pieces of experimental data that are only sensitive to averages over a range of propagation directions [51]. Our results represent a significant advancement in the ability to experimentally probe Bloch wavefunctions, but more information can be extracted from these experiments. Once we know the form of the wavefunctions we can isolate the contributions from each species of electron-hole pair by using Eq. 2.30 to calculate $\varsigma_{\mathrm{HH},n}$ and $\varsigma_{\mathrm{LH},n}$. Examining the dependence of these quantities on various experimental parameters has led to insight on the nature of dephasing during HSG (see

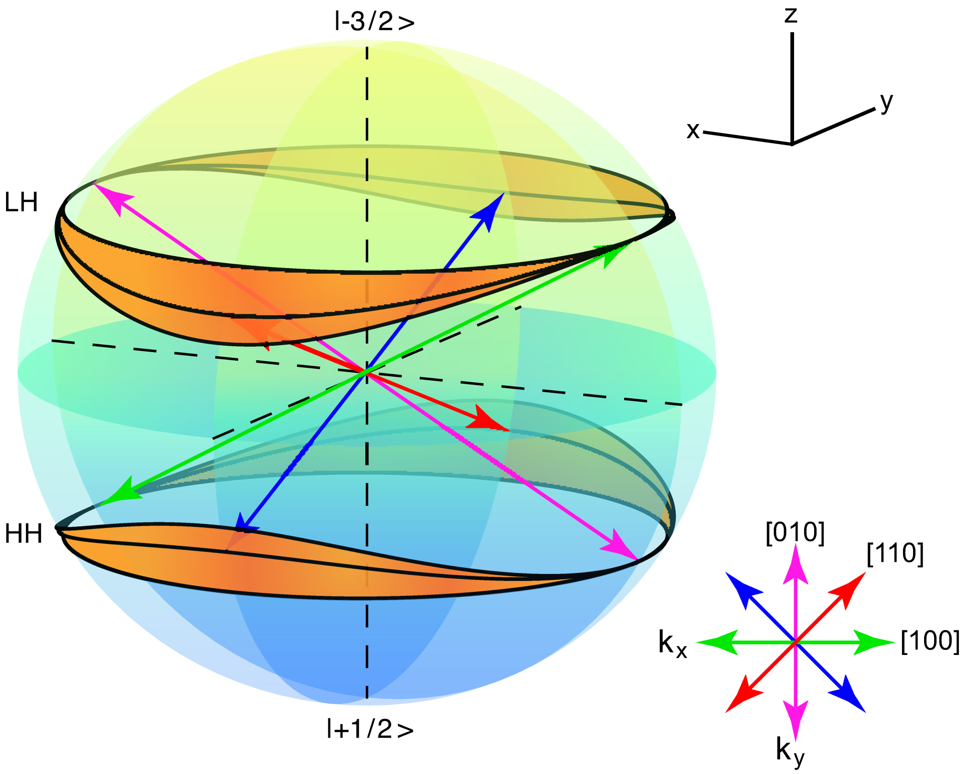

Figure 2.9: **Reconstruction of Bloch wavefunctions for holes of GaAs.** The Bloch wavefunctions of the HH and LH associated $\hat{H}_+$ in Eq. 2.20 are plotted on a Bloch sphere with black lines. The orange shaded area corresponds to the uncertainty in the form of the wavefunction from the standard deviation in our measurement of γ_3/γ_2. For a given θ, each wavefunction is represented by a single point on the Bloch sphere. The poles of the Bloch sphere correspond to the $|{-3/2}\rangle$ and $|{+1/2}\rangle$ states. The polar angle tells the relative magnitude of each pole state and the azimuthal angle corresponds to the relative phase between the polar states. The arrows within the Bloch sphere point to the LH and HH Bloch wavefunctions for the values of θ defined by the Miller indices in the inset. The wavefunctions for $\hat{H}_-$ are the same paths reflected across the $x-z$ plane on a Bloch sphere with $|{+3/2}\rangle$ and $|{-1/2}\rangle$ states as the poles.

Ch. 3) but there is in principle more information that can be extracted using this method [52]. THz field strength dependent measurements have been used to probe deeper into the role of the dynamical phase in HSG and provided closer experimental access to the phase itself using the analogy of a Michelson interferometer [53].

There has been interest in using HSG polarimetry to extract all of the Luttinger parameters. In practice, we have attempted to use a multidimensional fit to extract γ_1 and γ_2 from our data. These fits failed to give unique values for the Luttinger parameters and dependend sensitively on input parametrers such as the dephasing and detuning.

During this analysis, we have ignored detuning which is the difference between the NIR photon energy and the gap. Careful consideration of how the THz drive affects the gap and the effect of NIR wavelength on sideband polarimetry could lead to the extraction of the so-called dynamical gap and simplify attempts to extract the rest of the Luttinger parameters. This refined method could lead to the direct extraction of the relative dynamical phase between E-HH and E-LH pairs for example.

An exciting next step for Bloch wavefunction interferometry through sideband polarimetry is to expand the method to other materials. HSG has been demonstrated in several different materials [54, 55, 56, 57], but polarimetry has not been performed on all these systems. When considering candidate materials, it is important to keep several parameters in mind at once. First, the material must be a semiconductor for the ballistic model of sideband creation to work, and the gap must be within the frequency range of the laser available. Second, it is important to consider how many different bands will contribute to sideband generation. In GaAs we have three bands involved which produce two types of electron-hole pairs. If there is only one type of quasiparticle pair, then this type of experiment will not yield any interference data. If there are more types of quasiparticle pair then the method of disentangling the interference data becomes more complicated since all of the data must be coupled into sideband polarizations which are always two-dimensional. Third, couplings between bands must be taken into account. In pure GaAs this is not an important factor, but in GaAs/AlGaAs quantum wells there is significant band coupling that complicates attempts to extract information from polarimetry data [45]. Fourth, in order for experiments to yield any useful data the dephasing rate must be sufficiently low that significant amounts of quasiparticle pairs survive to annihilation and therefore sideband generation. Fifth and finally, it is important to consider the type of quasiparticle being excited. We have focused on electrons and holes, but condensed matter systems can host much more exotic types of quasiparticle, and as long as those quasiparticles have charge they can be accelerated by the THz drive.

Chapter 3

Temperature Dependent HSG Polarimetry as a Probe of Dephasing

Now that we have established high-order sideband polarimetry as an interferometer for Bloch waves in GaAs, it is important to understand the limits of the method. Perhaps the largest limiting factor in polarimetry experiments is how dephasing damps the generation of sidebands. Although there is a theoretical limit to how many sidebands can be produced by a given THz drive, the observed number of sidebands in experiments does not approach this limit because of dephasing processes that exponentially damp contributions from electron-hole pairs with long acceleration times.

In order for sideband polarimetry to be experimentally useful, the dephasing rate must be low enough that many orders of sidebands can be observed. This limit is part of the reason why past experiments in sideband polarimetry have focused on GaAs at low temperatures, which has a very low dephasing rate. Other materials with higher disorder and higher temperatures both lead to higher dephasing, making experiments more difficult.

A further complication is a lack of understanding of how the quantum interference which causes sideband polarization to change is affected by increased dephasing. Although sideband generation has been reported at high temperature in many materials [57, 58, 54], polarimetry of sidebands in GaAs has only been reported at low temperatures and minimal dephasing. Understanding how quantum interference is affected by dephasing is key to designing future experiments for sideband polarimetry both in GaAs and beyond. Temperature dependence provides an experimentally attractive method for understanding how dephasing affects HSG since it is relatively simple to control and measure temperature, and there is no need to fabricate new samples for different dephasing environments.

Careful control of the dephasing environment experienced by electron-hole pairs also allows the possibility of extracting information about interactions that occur during THz acceleration. Using the results of Ch. 2 we can separate the contributions of E-HH and E-LH pairs as a function of temperature. This allows us to extract the temperature dependent part of the dephasing for each type of hole independently, which is otherwise difficult due to the degeneracy of the bands. Furthermore, in GaAs the most common method of measuring dephasing is to examine the width of peaks in linear absorption or photoluminescence, which gives dephasing of electrons and holes near equilibrium [59, 60, 61, 62, 63, 64]. By studying the dephasing in HSG, we can study the dephasing during the very non-equilibrium process of acceleration by the THz field. These dephasing rates may be of interest when designing devices that rely on accelerating charge carriers away from equilibrium.

3.1 Dephasing in High-order Sideband Generation

Let us consider the role of dephasing in sideband generation. We return to Eq. 2.27 and note that the dephasing is a purely real decaying exponential for each $\varsigma_{j,n}$. The total dephasing is

$$\mathcal{G}_j(t',t) = \frac{1}{\hbar}\int_{t'}^{t} dt''\Gamma_j(\boldsymbol{k}(t'')) \tag{3.1}$$

where $\Gamma_j(\boldsymbol{k})$ is the momentum dependent dephasing rate for the relevant electron-hole pair. In the case of sufficiently strong dephasing, we need not consider $\boldsymbol{k}$ space trajectories other than the semiclassical trajectory. In this case the dephasing integral becomes the same as in Eq. 1.81. In this work, we will assume that the dephasing rate Γ_j is independent of $\boldsymbol{k}$. In this case, the constant Γ_j should be understood as the mean dephasing experienced by the electron-hole pair over the acceleration process. In this case, we can express the dephasing relationship as

$$\varsigma_{j,n} \propto e^{-\Gamma_j \tau_j(n)/\hbar} \tag{3.2}$$

where $\tau_j(n)$ is the acceleration time associated with the j electron-hole pair and sideband order n. This acceleration time is defined as the time between electron-hole creation t_0 and annihilation t_f,

$$\tau_{j,n} = t_{f,j,n} - t_{0,j,n}. \tag{3.3}$$

Note that Γ_j is independent of sideband order, so the decay as a function of order is mostly due to the increased acceleration time $\tau_{j,n}$.

3.2 Temperature Dependent Dephasing in Gallium Arsenide

Dephasing in GaAs can be attributed to many different mechanisms. One such source is based on defects in the crystal, which can cause scattering. This source of dephasing is largely temperature independent. In the case of high charge densities, Coulomb effects can be a significant source of dephasing. In our experiments, the NIR laser is sufficiently weak for us to ignore Coulomb effects. Larger charge densities would make our linear response formalism for the NIR insufficient and we could not use Jones matrices to accurately model polarization change.

The dominant source of dephasing in our experiments comes from interactions with phonons, which are quantized quasiparticles of lattice vibrations. Interactions with phonons can be caused by the emission of a phonon by an energized quasiparticle or the absorption of a pre-existing phonon. Phonon populations are closely tied to temperature. We will focus on two varieties of phonon which are relevant to our experiments in GaAs. Acoustic phonons have populations which are linearly related to temperature [65] and longitudinal-optical (LO) have populations which follow the Bose-Einstein distribution

$$n_{\mathrm{LO}} = \frac{1}{e^{\varepsilon_{\mathrm{LO}}/k_B T} - 1} \tag{3.4}$$

where n_{LO} is the LO phonon population, $\varepsilon_{\mathrm{LO}}$ is the energy of the LO phonon (in GaAs $\varepsilon_{\mathrm{LO}} = 36.6$ meV). Fig. 3.1 b) shows n_{LO} as a function of temperature. Notably, below around 100 K the occupation number is relatively small but above 100 K the occupation grows exponentially.

We are primarily interested in the temperature dependence of dephasing so we will model the dephasing according to

$$\Gamma_j(T) = \Gamma_{j,0} + \Gamma_{j,\mathrm{A}} T + \Gamma_{j,\mathrm{LO}} n_{\mathrm{LO}}(T) \tag{3.5}$$

where $\Gamma_{j,0}$ is the temperature independent part of the dephasing rate, $\Gamma_{j,\mathrm{A}}$ is the dephasing coefficient of the acoustic phonons, and $\Gamma_{j,\mathrm{LO}}$ is the dephasing coefficient of the LO phonons. $\Gamma_{j,0}$ contains contributions from many sources including phonon emission, which is not strongly correlated with temperature. At low temperatures $\Gamma_{j,0}$ can dominate the dephasing, but as temperature increases the LO contribution tends to dominate. The acoustic contribution is dominant for intermediate temperatures. Eq. 3.5 is commonly used to model the temperature dependent behavior of dephasing in GaAs [66].

It is important to note that all of the dephasing coefficients in Eq. 3.5 depend on the species of hole present in the electron-hole pair since the interactions which cause the dephasing depend on the nature of the hole.

3.3 Temperature Dependent Sideband Polarimetry

Our goal is to perform sideband polarimetry at different temperatures to see how the polarization is affected by the increased dephasing. There is an experimental complication to this, which is that the band gap of GaAs depends on temperature. It is important for our experiments that the NIR photon energy is equal to the gap energy, so it is important to measure the gap at each temperature.

We measure the gap using the using a technique called absorption. We use a halogen white light source that has an extremely broad frequency spectrum. We then measure this spectrum with and without the sample inserted. The ratio of measured counts with the sample to the measured counts without the sample is called the absorption. Technically, we do not account for reflected light so what we do is more properly called differential transmission, but this difference is small for our experiments so we call the method absorption. Fig. 3.1 a) shows absorption peaks measured at temperatures from 25 K to 200 K. As temperature increases, the peaks broaden due to the increased dephasing near equilibrium and move to lower energies due to the shrinking of the gap with increased temperature.

Low temperature absorption of GaAs show two peaks that correspond to excitons.

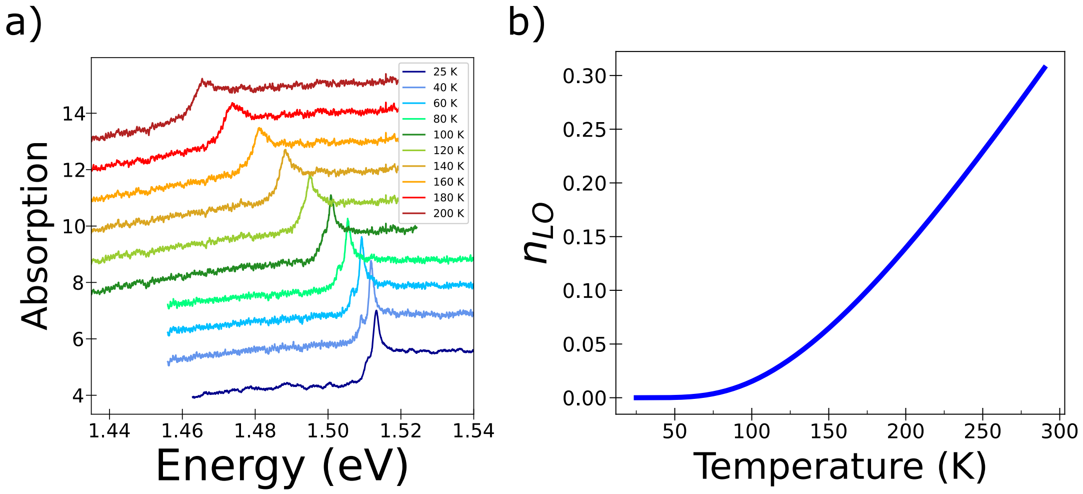

Figure 3.1: **Temperature dependent absorption and LO phonon occupation.** **a)** The absorption of our sample at different temperatures ranging from 25 K (blue) to 200 K (red) in dB. Each spectrum is by 1 dB for visibility. For HSG experiments, we absorption to locate the gap and tune the NIR to that energy. At low temperatures the separate peaks from HH and LH band are visible. At higher temperatures the peaks become broader due to increased dephasing near equilibrium. This increase is largely due to the increased phonon density due to higher temperature. **b)** Occupation number of the LO phonon as a function of temperature, as in Eq. 3.4. Below 100 K the LO phonon occupation is very small, but above 100 K the population grows rapidly.

Excitons are formed by a hydrogen-like bound state of electrons and holes. The two peaks are formed by E-HH and E-LH. They are split by strain in the system. We use these peaks to pick out the proper NIR wavelength for HSG experiments at each temperature.

We performed experiments at the following temperatures and wavelengths.

Temperature (K)	NIR Wavelength (nm)
25	820.0
100	826.8
120	830.2
140	834.2
160	839.6
180	842.5
200	848.0

Fig. 3.2 shows the sideband intensities at these temperatures as a function of sideband order when the NIR is polarized parallel to the THz. All sidebands were normalized to the $2nd$ order sideband at 25 K. These spectra were taken with the Stokes polarimeter while the QWP was aligned with the polarizer so only the component of sideband polarization parallel to the THz field is shown. As expected, lower temperatures are more intense. At higher temperatures fewer sidebands were detected.

There is a further experimental complication to this experiment, which is that the quantum efficiency of our detectors varies as a function of wavelength. This effect is negligible over a single sideband spectrum, but is significant over the wavelength ranges used here. This difference in sensitivity is part of the reason why fewer sidebands were measured at higher temperatures. Both detectors have higher sensitivity to shorter wavelengths, so the higher wavelengths used in the high temperature experiments had a higher noise floor, which is why in Fig. 3.2 weaker sidebands were measured at lower temperatures. To include the wavelengths of all sidebands measured in our experiment, we performed detector calibration from 790-848 nm for both the CCD and the PMT.

Calibration was performed using a halogen white light source that provided a very broadband source of light. We then used a small monochromator to select a small range of wavelengths from the white light spectrum. Moving in steps of five nm, we then measured the intensity of the light on each detector and integrated the total peak. The light after the monochromator was measured using a frequency-independent FieldMaster power meter from Coherent lasers. This allowed us to calculate the detector response per watt of incident light.

Once the detectors have been properly calibrated, we simply use a temperature controller with a PID feedback to stabilize the temperature of the sample and perform Stokes polarimetry as in Ch. 2. We repeat the measurement for four linear NIR polarizations $\alpha_{\mathrm{NIR}} = 90^\circ$, $\alpha_{\mathrm{NIR}} = 45^\circ$, $\alpha_{\mathrm{NIR}} = 0^\circ$, and $\alpha_{\mathrm{NIR}} = -45^\circ$.

Fig. 3.3 shows the sideband polarimetry measurements at each temperature shown in Fig. 3.2. The sideband polarization results show remarkable robustness to temperature. Up to 160 K the sidebands have very similar polarizations. Above 160 K reduced signal to noise ratio leads to more deviation in the higher orders, but even at 200 K the low orders have polarizations that are very similar to the other temperatures. Declining signal strength made measurements at higher temperatures difficult.

This consistency of polarization reinforces our understanding of the underlying quantum interference that sets the polarization state. The dynamical phase, defined in Eq. 2.28 does not depend on temperature. Other than the band gap, the energies of the electron-hole pair do not have much of a temperature dependence. Therefore the acceleration process is largely unchanged except for the dephasing which causes smaller signals. However, the electron-hole pairs that maintain coherence contain the same information at different temperatures and the polarizations of the sidebands that are created are the same. This is encouraging for applications of sideband polarimetry. In GaAs, sideband polarimetry can be done at liquid nitrogen temperatures with relatively small changes in signal intensity and negligible changes to sideband polarizations. In materials beyond GaAs this result is encouraging because it demonstrates that even in very strong

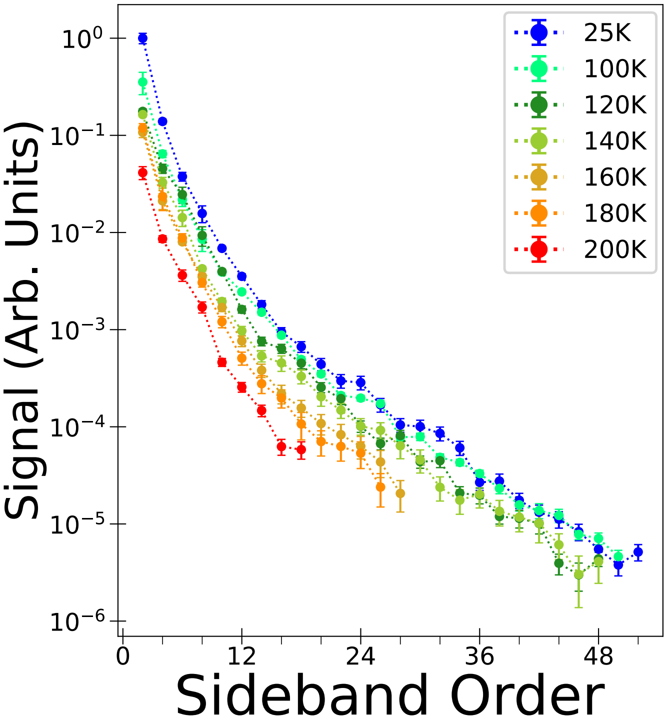

Figure 3.2: **Temperature dependent sideband intensity.** Sideband intensities as functions of sideband order for different temperatures. The temperatures are 25 K (blue), 100 K (blue-green), 120 K (green), 140 K (yellow-green), 160 K (yellow), 180 K (orange), and 200 K (red). The intensities are normalized to the 2nd order sideband at 25 K. The NIR is polarized parallel to the THz. These spectra were measured using the Stokes polarimeter, with the QWP aligned with the polarizer so only the component of sideband polarization parallel to the THz is shown. These sidebands were measured using THz pulses with a field strength of 65 ± 3 kV/cm and a frequency of 449 ± 1 GHz.

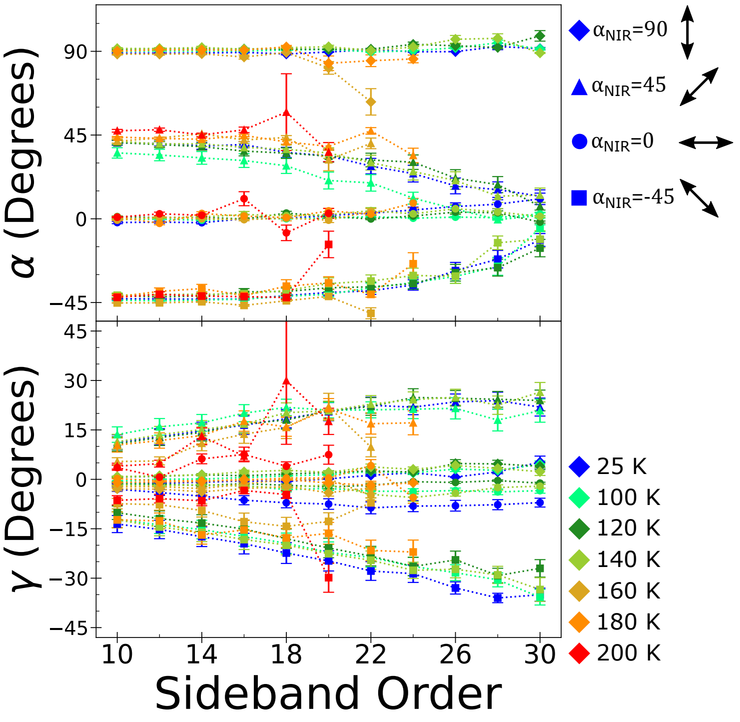

Figure 3.3: **Temperature dependent HSG polarimetry.** The linear orientation angle α (upper) and ellipticity angle γ (lower) of sidebands are plotted as functions of sideband order for temperatures ranging from 25 K (blue) to 200 K (red). The colors match those in Fig. 3.2. For each temperature data for four linear polarizations of the NIR laser ($\gamma_{\mathrm{NIR}} = 0°$) are shown, with $\alpha_{\mathrm{NIR}} = 90°$ (diamonds), $\alpha_{\mathrm{NIR}} = 45°$ (triangles), $\alpha_{\mathrm{NIR}} = 0°$ (circles), and $\alpha_{\mathrm{NIR}} = -45°$ (squares). Above 140 K fewer sidebands are measured. At 200 K no sidebands were measured for $\alpha_{\mathrm{NIR}} = 90°$ due to a lack of signal.

dephasing environments, sideband polarization is still set by quantum interference.

3.4 Extracting Temperature Dependent Dephasing via Sideband Polarimetry

Although the polarizations of the sidebands do not have a strong temperature dependence, we can use the intensities of the sidebands as functions of temperature to investigate the temperature dependent dephasing of the system. Since we took four polarimetry scans at each temperature we can extract the Jones matrix for each sideband at each temperature. Using Eq. 2.30 we can then calculate $\varsigma_{\mathrm{HH},n}$ and $\varsigma_{\mathrm{LH},n}$ for all temperatures. We focus on the intensity of these quantities to consider the effects of dephasing.

We use the form of dephasing specified in Eq. 3.5, and restate the relationship between the $\varsigma_{j,n}$ and dephasing as

$$\varsigma_{j,n} \propto e^{-\Gamma_j(T)\tau_j(n)/\hbar} \tag{3.6}$$

where we have made explicit that the temperature dependence is contained in the dephasing rate $\Gamma_j(T)$ and the sideband order dependence is contained in the acceleration time $\tau_j(n)$. We can calculate the acceleration time from experimental parameters, so the only unknown quantity in Eq. 3.6 is the dephasing rate.

Fig. 3.4 a) shows $|\varsigma_{\mathrm{HH},n}|$ and $|\varsigma_{\mathrm{HH},n}|$ as a function of sideband order. The lower temperatures have stronger signals, but the HH and LH have different falloffs as a function of sideband order. Fig. 3.4 b) shows each order of $|\varsigma_{\mathrm{HH},n}|$ and $|\varsigma_{\mathrm{HH},n}|$ as functions of temperature with each order normalized to the $T = 25$ K data. This normalization removes the Γ_0 dependence. This leaves only two free parameters Γ_{A} and Γ_{LO} for each hole species. We fit all sideband orders to Eq. 3.6 simultaneously The dotted lines in

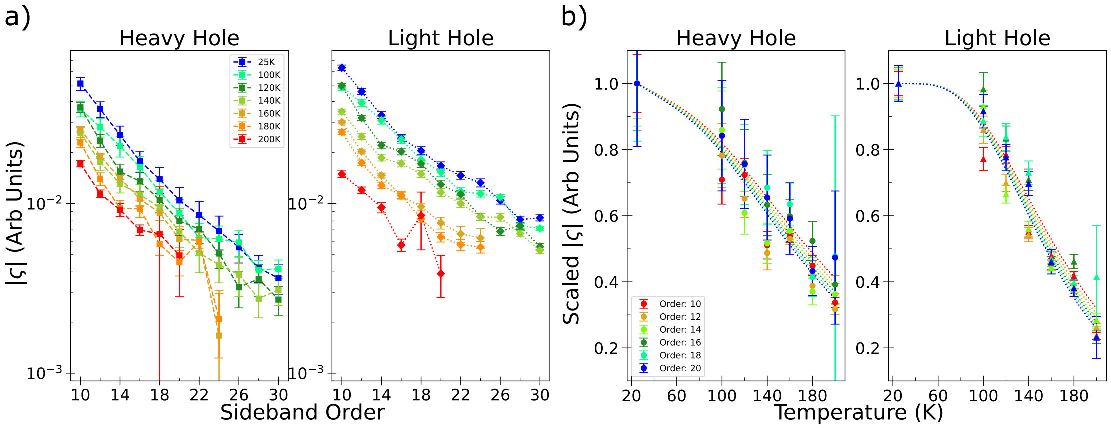

Figure 3.4: **Temperature dependent fall-offs of the E-HH and E-LH contributions to sideband polarizations. a)** The absolute value of the contribution for the E-HH and E-LH pairs, ς_{HH} (left, squares) and ς_{LH} (right, diamonds) for different temperatures running from 25 K (blue) to 200 K (red) as functions of sideband order. The colors match those in Fig. 3.3. **b)** The absolute value of ς_{HH} (left, circles) and ς_{LH} (right, triangles) of different sideband orders as functions of temperature. Each plot is normalized to the 25 K data to isolate the dependence of the falloff for each sideband on temperature. The dotted lines in each frame show the results from fitting all data for each hole species to Eq. 3.6. For each fit there are two free parameters, $\Gamma_{\mathrm{A},j}$ and $\Gamma_{\mathrm{LO},j}$ where j labels the hole species. Different sideband orders are associated with different $\tau_j(n)$ for the recollision processes, so the dotted lines for different orders are slightly different despite the dephasing function $\Gamma_j(T)$ being the same.

Fig. 3.4 b) correspond to the falloff using the results of this fit. All data for each hole species is used in the same fit, but due to small differences in the acceleration time as a function of sideband order, each order has a slightly different expected falloff and thus a slightly different dotted line.

The results of the fit are $\Gamma_{\mathrm{HH,A}} = 6.1 \pm 1.6\ \mu\mathrm{eV/K}$, $\Gamma_{\mathrm{LH,A}} < 1.5\ \mu\mathrm{eV/K}$, $\Gamma_{\mathrm{HH,LO}} = 14 \pm 3$ meV, and $\Gamma_{\mathrm{LH,LO}} = 30 \pm 3$ meV. Fig. 3.5 shows the fits for Γ_{A} and Γ_{LO} for both HH and LH. The fits using all data are shows using solid lines while the dots correspond to fits using each sideband order individually. The errors are the square root of the covariance of the fit. The fits are likely less sensitive to the acoustic phonon contribution because the LO phonon dominates for most of the temperature range we sampled. This result agrees with previous results that the LO phonon is the dominant source of dephasing in bulk GaAs.

3.5 Conclusion

The temperature dependent results reported here are important for two reasons. First, the robustness of polarization states to increased temperature and dephasing is encouraging for extending interferometry through sideband polarimetry to new systems with more intense dephasing. Second, our ability to probe dephasing mechanisms is exciting as another application of Bloch wave interferometry.

Our results are not the first to measure dephasing in GaAs, but our method based on sideband polarimetry represents a new way to measure dephasing. The ability of our method to distinguish the contributions of different Bloch wavefunctions is a key advantage. Although theory has long predicted differences between the HH and LH dephasing and scattering [65], this is to our knowledge the first experiment that differentiates the dephasing coefficients of these holes near the band gap. Other investigations of

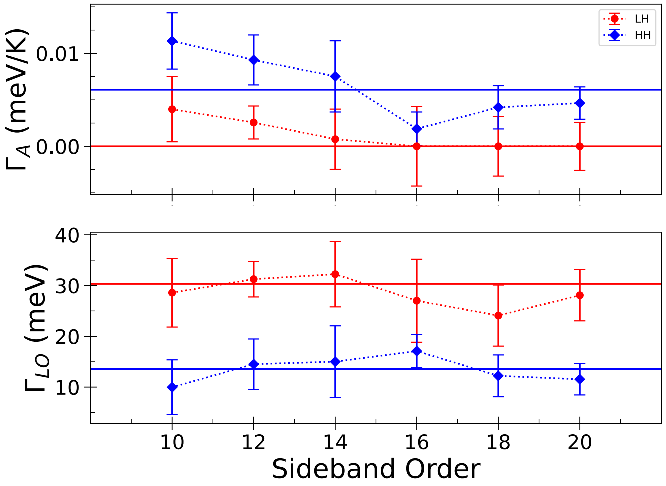

Figure 3.5: **Extracted coefficients for the temperature dependent part of dephasing rates.** The coefficients $\Gamma_{\mathrm{A},j}$ and $\Gamma_{\mathrm{LO},j}$ in the dephasing function 3.5 are extracted by fitting scaled $|\varsigma_{\mathrm{HH}}|$ and $|\varsigma_{\mathrm{LH}}|$ shown in Fig. 3.4b) to Eq. 3.6. The red (blue) solid horizontal lines represent the results from fitting all sideband orders to a dephasing function $\Gamma_{\mathrm{LH}}(T)(\Gamma_{\mathrm{HH}}(T))$ that is assumed to be independent of sideband order. The numerical values are $\Gamma_{\mathrm{HH,A}} = 6.1 \pm 1.6$ μeV/K, $\Gamma_{\mathrm{LH,A}} < 1.5$ μeV/K, $\Gamma_{\mathrm{HH,LO}} = 14 \pm 3$ meV, and $\Gamma_{\mathrm{LH,LO}} = 30 \pm 3$ meV, which produce the dotted lines in Fig. 3.4b). These confidence intervals give the standard deviation by taking the square root of the covariance of the fits.

dephasing in GaAs have used the linewidth of photoluminescence or absorption spectra [62, 61, 67, 68] or used four-wave mixing to probe dephasing [64]. These experiments are complicated by the degeneracy of the LH and HH band at the band gap and have particular difficulty at high temperatures, where strain-induced splittings of the HH and LH bands are washed out by broadened peaks.

In contrast to other methods which focus on the behavior of electrons and holes near equilibrium, our method probes the dephasing experienced by non-equilibrium electron-hole pairs in continuum states. These non-equilibrium states are different than the equilibrium case and have been studied in many situations, such as materials producing high-order harmonics [69, 70], quantum well superlattices [71], or Luttinger liquids [72, 73, 74]. However, to our knowledge the non-equilibrium dephasing rates in GaAs have not been previously measured. Our results pave the way to measuring the non-equilibrium dephasing rates of a large class of semiconducting materials.

A further advantage of our method is the possibility of crystal angle dependence by rotating the crystal with respect to the THz drive. By studying the angular dependence of sideband polarimetry it is possible to probe dephasing in different crystal directions. This sensitivity is not possible in linear optical methods like absorption. In systems that have large anisotropies, this sensitivity could be useful in characterizing the dephasing.

This analysis is missing information about the temperature independent part of the dephasing. There has been progress in theoretical analysis of extracting dephasing from analyzing THz field strength sweeps [52]. This analysis is able to extract the dephasing from individual sidebands and could lead to insight into $\boldsymbol{k}$ dependent dephasing. This more accurate model could then allow extraction of further information from polarimetry data.

Changing the THz field strength changes the acceleration time $\tau_j(n)$, and perhaps a relatively straightforward application of the methods developed here to field strength dependent data could yield some insight into the temperature independent dephasing.

It is also possible to push experiments in bulk GaAs to room temperature. In the experiments reported here, decreasing signal was a problem, but technical difficulties with the NIR laser contributed to the experimental difficulty. Furthermore, in these experiments we had to change the short pass filter and long pass filter as wavelengths changed. At higher wavelengths, the filters were not as sharp, which contributed to increased noise in the experiments.

Chapter 4

The Effect of Strain and Geometric Phases on Sideband Polarimetry

Sideband polarimetry is sensitive to the local physics experienced by electrons and holes during their acceleration by the THz. This sensitivity extends to strain, the constant deformation of the crystal away from the equilibrium position of crystal ions. In our experiments this strain is caused by the fact that our GaAs is mounted on a sapphire substrate, which has a different coefficient of thermal expansion than GaAs. As a result, strain occurs at the low temperatures where we normally perform experiments.

Historically this strain has been viewed as a nuisance. If strain variation in the sample is significant on distances similar to the NIR beamspot (diameter of roughly 1 mm), then the electron-hole pairs in different parts of the beam will experience different physics and produce different polarizations. This effect is expressed as a lowering of the degree of polarization of the sideband. We solved this problem by creating circular samples instead of rectangular samples. These samples still had strain, but the strain varied much less over the sample, and did not degrade the degree of polarization to the same degree.

We know that strain exists in the samples due to the splitting of the exciton peaks in absorption spectra, which is visible in the low temperature spectra in Fig. 3.1. However, in Ch. 2 and Ch. 3 we ignore the strain and model the sample with the Luttinger Hamiltonian. Here, we explore the role that strain holds in modifying the Hamiltonian and how this can affect the phases which are expressed in Bloch wave interferometry, including the possibility of measuring Geometric phases. Unlike the other chapters of this dissertation, the work presented in this chapter was not successfully completed in experiments but future students could certainly produce exciting work by measuring strain effects in HSG polarimetry.

4.1 Strain in Gallium Arsenide

Consider a crystal that is subject to some external force that causes it to change shape and volume. Each point in the solid is then deformed. The unstrained position is given by the vector $\boldsymbol{x}$ and the strained position is given by the vector $\boldsymbol{x}'$. We define the change between these positions using the displacement vector

$$\boldsymbol{\epsilon} = \boldsymbol{x}' - \boldsymbol{x}. \tag{4.1}$$

We now consider two points that are very close to each other, separated by the infinitesimally small distance

$$\mathrm{d}l^2 = \sqrt{\mathrm{d}x^2 + \mathrm{d}y^2 + \mathrm{d}z^2} \tag{4.2}$$

where $\mathrm{d}x_i$ are the distances in each dimension, which we label using a subscript i and $x_i = x, y, z$. After deformation, this distance becomes $\mathrm{d}l'$ which is related to the undeformed distance by $\boldsymbol{\epsilon}$

$$\mathrm{d}l'^2 = \sum_i (\mathrm{d}x_i + \mathrm{d}\epsilon_i)^2 \tag{4.3}$$

where $\mathrm{d}\epsilon_i$ is the ith component of the differential displacement. We use the chain rule to write this as

$$\mathrm{d}\epsilon_i = \frac{\partial \epsilon_i}{\partial x_j}\mathrm{d}x_j \tag{4.4}$$

where we have used the Einstein sum notation to suppress a sum over j. We assume that displacements from small deformations are in turn small, so we can expand Eq. 4.3 using Eq. 4.4 and ignore terms quadratic in derivatives of the displacement vector. This gives

$$\mathrm{d}l'^2 = \mathrm{d}l^2 + 2\frac{\partial \epsilon_i}{\partial x_j}\mathrm{d}x_i\mathrm{d}x_j \tag{4.5}$$

where there are implicit sums over the indexes i and j in the second term. We introduce the strain tensor, defined as

$$\epsilon_{ij} = \frac{1}{2}\left(\frac{\partial \epsilon_i}{\partial x_j} + \frac{\partial \epsilon_j}{\partial x_i}\right). \tag{4.6}$$

This allows us to write the final form of the deformed length differential,

$$\mathrm{d}l'^2 = \mathrm{d}l^2 + 2\epsilon_{ij}\mathrm{d}x_i\mathrm{d}x_j. \tag{4.7}$$

The strain tensor ϵ_{ij} gives the change in an element of length due to deformation. The two indexes can be thought of as the displacement along the ith direction due to a deformation along the jth direction. The strain tensor is symmetric, so $\epsilon_{ij} = \epsilon_{ji}$ so there are in general six independent components. For further discussion of the derivation of these equations and the fundamentals of strain, see Landau and Lifshitz *Theory of Elasticity* [75].

We reiterate that the strain is small compared to the crystal as a whole, so we can treat the strain as a perturbation to the Luttinger Hamiltonian. We can write the entire Hamiltonian as

$$\hat{H} = \hat{H}_{\mathrm{Lutt}} + \hat{H}_{\epsilon} \tag{4.8}$$

where $\hat{H}_{\text{Lutt}}$ is the Luttinger Hamiltonian and $\hat{H}_\epsilon$ is the strain Hamiltonian. The form of the strain Hamiltonian can be found by considering symmetry of the crystal. The full derivation of this Hamiltonian is beyond the scope of this work, but the full treatment can be found in Lew Yan Voon and Willatzen's *The $k \cdot p$ Method* [33]. We will quote the result for the four band model of zincblende crystals like GaAs using the same angular momentum basis we used earlier,

$$\hat{H}_\epsilon = \begin{pmatrix} a\text{Tr}\epsilon + bq(\epsilon) & d(\epsilon_{xz} - i\epsilon_{yz}) & \frac{\sqrt{3}}{2}b\delta(\epsilon) - id\epsilon_{xy} & 0 \\ d(\epsilon_{xz} + i\epsilon_{yz}) & a\text{Tr}\epsilon - bq(\epsilon) & 0 & \frac{\sqrt{3}}{2}b\delta(\epsilon) - id\epsilon_{xy} \\ \frac{\sqrt{3}}{2}b\delta(\epsilon) + id\epsilon_{xy} & 0 & a\text{Tr}\epsilon - bq(\epsilon) & -d(\epsilon_{xz} - i\epsilon_{xy}) \\ 0 & \frac{\sqrt{3}}{2}b\delta(\epsilon) + id\epsilon_{xy} & -d(\epsilon_{xz} + i\epsilon_{yz}) & a\text{Tr}\epsilon + bq(\epsilon) \end{pmatrix} \tag{4.9}$$

where a, b, and d are material constants called deformation potentials, $\text{Tr}\epsilon = \epsilon_{xx}+\epsilon_{yy}+\epsilon_{zz}$ is the trace of the strain tensor, and $q(\epsilon)$ and $\delta(\epsilon)$ are functions of strain defined as

$$\begin{aligned} q(\epsilon) &= \epsilon_{zz} - \frac{1}{2}(\epsilon_{xx} + \epsilon_{yy}) \\ \delta(\epsilon) &= \epsilon_{xx} - \epsilon_{yy}. \end{aligned} \tag{4.10}$$

If we assume that time reversal symmetry is not broken by the strain, then $\epsilon_{xz} = \epsilon_{yz} = 0$. In this case, the strain Hamiltonian breaks down into the same block-diagonal components that the Luttinger Hamiltonian does as long as we stay in the $k_z = 0$ plane. These blocks are

$$\hat{H}_\epsilon = \begin{pmatrix} a\text{Tr}\epsilon + bq(\epsilon) & \frac{\sqrt{3}}{2}b\delta(\epsilon) - id\epsilon_{xy} \\ \frac{\sqrt{3}}{2}b\delta(\epsilon) + id\epsilon_{xy} & a\text{Tr}\epsilon - bq(\epsilon) \end{pmatrix} \tag{4.11}$$

with the basis states corresponding to the basis states of the Luttinger block diagonal components. It is in general difficult to calculate the form of the strain, but we can make some approximations. A common approximation for cylindrical crystals with a stress applied at one vertical interface is the bi-axial strain approximation. In this case we assume that

$$\epsilon_{xx} = \epsilon_{yy} = -\frac{C_{11}}{2C_{12}}\epsilon_{zz} \tag{4.12}$$

where C_{11} and C_{12} are elements of the stiffness tensor which are generally known for GaAs, and off-diagonal elements of the strain tensor are assumed to be zero. With this assumption, the Hamiltonian becomes

$$\hat{H}_\epsilon = \begin{pmatrix} 2a(\epsilon_{xx} - \mathcal{C}\epsilon_{xx}) - b(\epsilon_{xx} + 2\mathcal{C}\epsilon_{xx}) & 0 \\ 0 & 2a(\epsilon_{xx} - \mathcal{C}\epsilon_{xx}) + b(\epsilon_{xx} + 2\mathcal{C}\epsilon_{xx}) \end{pmatrix} \tag{4.13}$$

where $\mathcal{C} = C_{12}/C_{11}$. This Hamiltonian is diagonal, so the energy eigenvalues are the diagonal entries. The difference between these represents the splitting between the light hole and heavy hole due to strain,

$$\delta\varepsilon_\epsilon = 2b(\epsilon_{xx} + 2\mathcal{C}\epsilon_{xx}). \tag{4.14}$$

This splitting corresponds to the splitting in the absorption spectrum, so if the biaxial strain approximation is valid then the strain can be characterized by measuring the splitting of the HH and LH absorption peak. In our samples this splitting is usually on the order of 2-4 meV at low temperatures (roughly 20-30 K). The relative heights of the absorption peaks correspond to the dipolar coupling of their angular momentum state, so the ordering of the peaks can differentiate between compressive and tensile strains. In our samples the strain appears to be compressive.

It is possible that there is some shearing strain present in the sample, which means $\epsilon_{xy} \neq 0$. In this case, the strain Hamiltonian is still block diagonal, but these blocks now

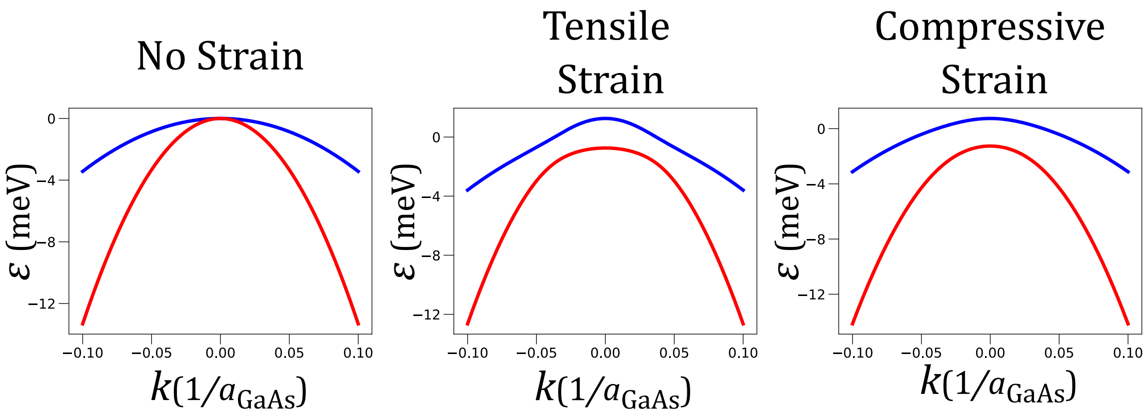

Figure 4.1: **Band structure of strained GaAs.** The band structure of the Luttinger Hamiltonian experiencing bi-axial strain according to Eq. 4.13. The left plot shows the unstrained band structure, the center plot shows the band structure under tensile strain, and the right plot shows the band structure under compresssive strain. The amount of strain in the middle and right plots corresponds to a sample where the absorption peaks are split by 2 meV, which is typical of our samples. The k axis is along the [010] direction and is given in units of inverse GaAs lattice constant ($a_{\mathrm{GaAs}} = 5.653$ Å)[49]. The energy axis is given in units of meV.

take the form

$$\hat{H}_\epsilon = \begin{pmatrix} 2a(\epsilon_{xx} - \mathcal{C}\epsilon_{xx}) - b(\epsilon_{xx} + 2\mathcal{C}\epsilon_{xx}) & -id\epsilon_{xy} \\ id\epsilon_{xy} & 2a(\epsilon_{xx} - \mathcal{C}\epsilon_{xx}) + b(\epsilon_{xx} + 2\mathcal{C}\epsilon_{xx}) \end{pmatrix}. \tag{4.15}$$

In this case, the Hamiltonian is not totally known even if the absorption peak splitting is measured. It is possible that this free parameter could be dealt with using sideband data of some sort, but the method to accomplish this is not clear.

The effects of strain are important to the shape of the bands and the form of the Bloch wavefunctions. The band structure of GaAs is shown for three different values of strain in Fig. 4.1, zero strain, tensile strain and compressive strain. The tensile and compressive cases correspond to the amount of strain necessary to split the absorption peaks by 2 meV. Since the Luttinger Hamiltonian is quadratic in $\boldsymbol{k}$, at $\boldsymbol{k} = 0$ the Luttinger Hamiltonian is a matrix of zeros which causes the degeneracy at this point. However, the strain Hamiltonian is constant in $\boldsymbol{k}$, so near $\boldsymbol{k} = 0$ the strain Hamiltonian dominates the Luttinger term. This lifts the degeneracy at $\boldsymbol{k} = 0$ and makes the bands non-parabolic, as can be seen in the middle and right plots of Fig. 4.1. The tensile strain is more clearly non-parabolic because of the avoided crossing which causes a bump feature in the higher energy band near $\boldsymbol{k} = 0$, but the compressive case is also non-parabolic. This logic also implies that the form of the wavefunctions is different, since the eigenfunctions of the strain Hamiltonian are not the same as the Luttinger Hamiltonian. At different points in $\boldsymbol{k}$ space the Bloch wavefunctions are different depending on the relative strengths of the strain and Luttinger Hamiltonian.

4.2 Phases Accumulated by Strained Carriers

In unstrained GaAs, HSG produces quantum interference through the differences in accumulated dynamical phases between E-HH pairs and E-LH pairs. In the strained case, there are three differences. First, the strain causes changes to the effective masses of the holes, which in turns changes the creation and annihilation times for the electron-hole pairs and therefore the dynamical phase accumulated. Second, the strain deforms the band structure, so the energies which determine the accumulation of the dynamical phase change. Third, the strain causes change to the wavefunctions which now change as a function of $|\boldsymbol{k}|$. This means that geometrical phases can now be accumulated by electron-hole pairs. Furthermore, this change leads to the emergence of the non-Abelian Berry connection as an important quantity in sideband generation.

The first two differences can be dealt with theoretically with numerical calculations. The formulas used to calculate the creation and annihilation times can no longer be used because the effective mass now changes with $|\boldsymbol{k}|$. Instead, using numerical methods with discrete time steps allows the trajectory to be calculated. This trajectory then allows the straightforward calculation of the dynamical phase. It should be noted that these calculations can be tricky and computationally intensive.

We will now consider the geometric phase effects. In the unstrained Luttinger Hamiltonian, the Berry connection is a divergence-less vector field. This is due to the fact that the wavefunctions do not change as a function of $|\boldsymbol{k}|$, but as a function of the angle θ in the $k_x - k_y$ plane. Fig. 4.2 shows the Berry connection element $\boldsymbol{\mathcal{A}}_{\mathrm{HH,HH},+}$ in the $k_z = 0$ plane. Recall from Eq. 1.72 that the Berry connection is defined as

$$\boldsymbol{\mathcal{A}}_{n,m}(\boldsymbol{k}) = i \langle n| \nabla_{\boldsymbol{k}} |m\rangle \tag{4.16}$$

so the direction of $\boldsymbol{\mathcal{A}}_{n,m}$ will be the direction in which the wavefunctions change. Since the Berry curvature is the curl of the Berry connection, this produces a Berry curvature that is curl-less which corresponds to the monopole of Berry curvature at the degenerecy of the HH and LH bands. Our experiments are performed with linearly polarized THz fields and begin at $\boldsymbol{k} = 0$. The black arrow in Fig. 4.2 represents the path taken by a hole in a typical experiment, passing in a straight line through the center of the Brillouin zone. Recall that the relationship between the geometric phase and Berry connection is

$$\gamma_{n,m} = i \int_{\boldsymbol{k}_0}^{\boldsymbol{k}_f} \boldsymbol{\mathcal{A}}_{n,m}(\boldsymbol{k}) \cdot \mathrm{d}\boldsymbol{k} \tag{4.17}$$

so geometric phases are only accumulated when the trajectory through $\boldsymbol{k}$ space aligns with the Berry connection. As shown in Fig. 4.2 $\boldsymbol{\mathcal{A}}_{\mathrm{HH,HH},+}$ is perpendicular to the direction of the hole at every point, so no geometric phase will be accumulated. This is true for all linear $\boldsymbol{k}$ space trajectories starting at $\boldsymbol{k} = 0$ in unstrained GaAs.

In the strained case, the degeneracy at the center of the Brillouin zone is lifted and there is no longer a monopole of Berry curvature there. This means that the Berry

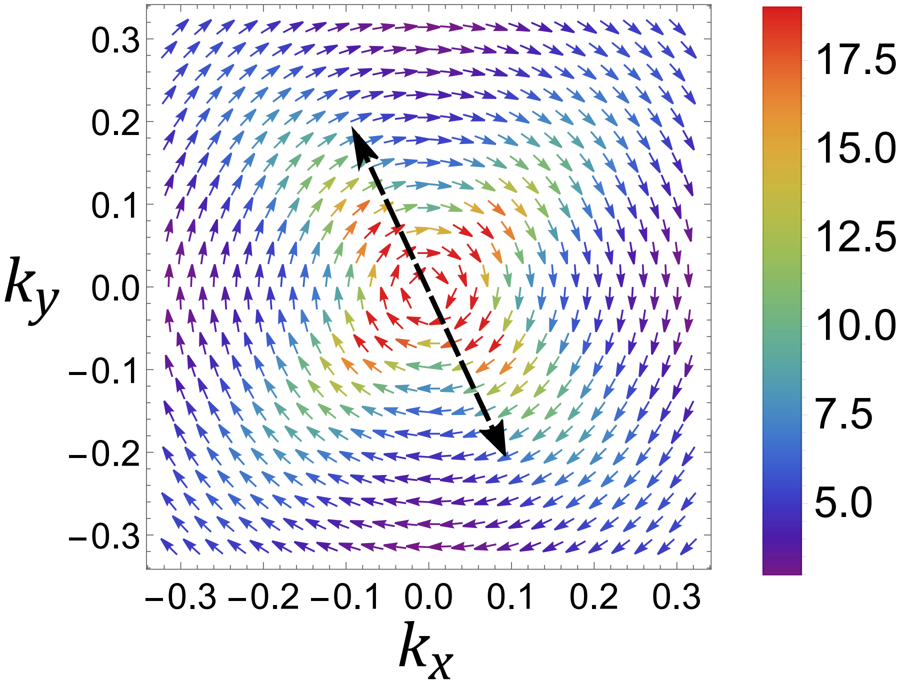

Figure 4.2: **Berry connection in unstrained GaAs**. The Berry connection element $\boldsymbol{\mathcal{A}}_{\mathrm{HH,HH},+}$ in the $k_z = 0$ plane. The double-headed black dotted arrow represents a path of a hole accelerated by a linearly polarized THz field. This arrow is perpendicular to the Berry connection (colored arrows) at all points so a hole following this trajectory would accumulate no geometric phase. The Berry connection is plotted in units of a_{GaAs} and the k parameters are given in units of inverse a_{GaAs}.

connection no longer divergence-less and

$$\boldsymbol{\mathcal{A}}_{n,m}(\boldsymbol{k}) \cdot \hat{k} \neq 0 \tag{4.18}$$

where $\hat{k}$ is the radial unit vector in $\boldsymbol{k}$ space. This means that even linear THz drives can produce geometric phases. Fig. 4.3 shows the magnitude of the radial component of the Abelian Berry connection element $\boldsymbol{\mathcal{A}}_{\mathrm{HH,HH},+}$ and the non-Abelian Berry connection element $\boldsymbol{\mathcal{A}}_{\mathrm{LH,HH},+}$ for the zero strain, tensile strain, and compressive strain cases. The tensile and compressive strain cases correspond to the amount of strain needed to split the absorption peaks by 2 meV. The radial component of the Berry connection is not everywhere in $\boldsymbol{k}$ space, it is localized to the parts of the Brillouin zone where the bands are the least parabolic. These areas correspond to the intermediate regime when neither the Luttinger Hamiltonian nor strain Hamiltonian dominates the physics. In this regime the wavefunctions are changing rapidly as a function of $|\boldsymbol{k}|$ which produces the radial Berry connection. In the tensile case, the top row of Fig. 4.3, there is an avoided crossing featuring a large amount of band mixing. This band mixing causes the largest radial Berry connections that we have considered here.

The system is complicated by the fact that radial non-Abelian Berry connection, shown on the right of Fig. 4.3, is non-zero in the strained cases. This component causes tunnelling between bands during acceleration, which will in turn result in changes in the polarization as the different holes interfere.

Mathematically, this coupling complicates our model and we can no longer use the $\varsigma_{j,n}$ to describe the evolution. Instead we write the electric polarization polarization as,

$$\mathbb{P}_n = \frac{1}{d^2} \sum_{s=\pm} \mathbb{D}_s^\dagger R_s \left(\frac{i\omega d^2}{2\pi V \hbar} \int_0^{2\pi/\omega} \mathrm{d}t e^{i(\Omega+n\omega)t} \int_{-\infty}^{t} \mathrm{d}t' e^{-i\Omega t'} \mathcal{S}_s(t',t) \right) R_s^\dagger \mathbb{D}_s \cdot \boldsymbol{E}_{\mathrm{NIR}} \tag{4.19}$$

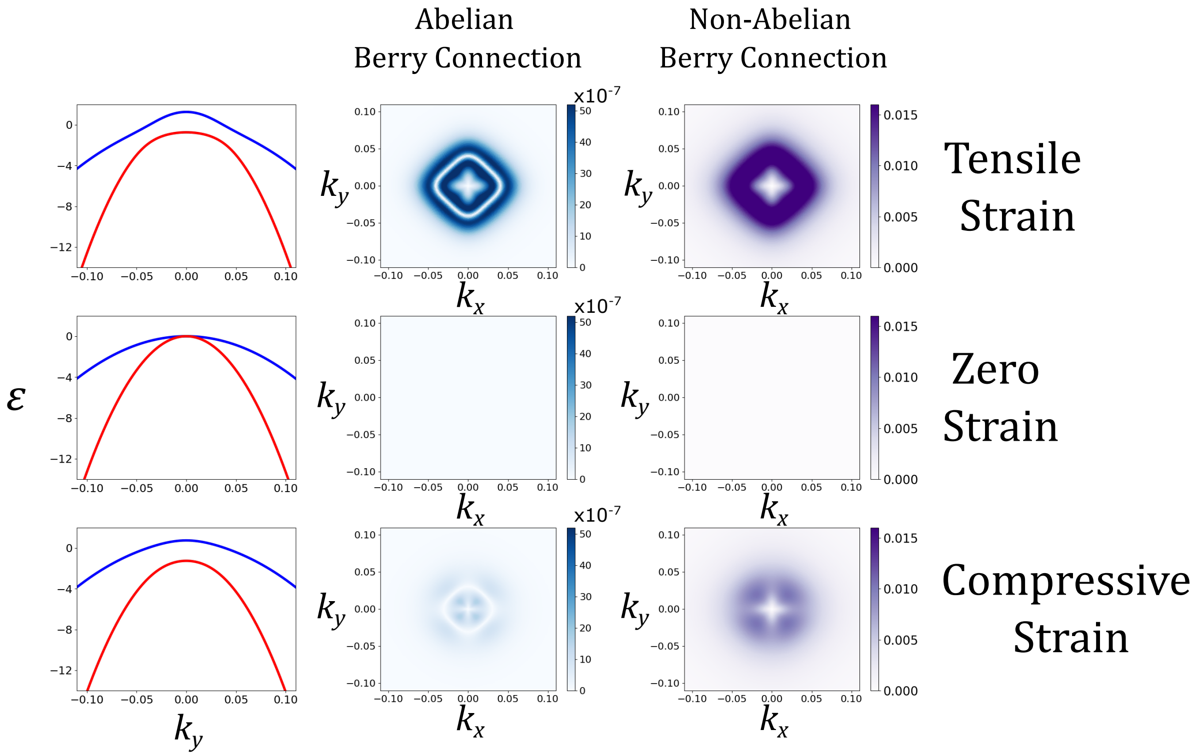

Figure 4.3: **Radial components of Berry connection in strained GaAs.** The band structure along [010] (left), the magnitude of the radial component (along $\hat{k}$) Abelian Berry connection element $\boldsymbol{\mathcal{A}}_{\mathrm{HH,HH,+}}$ (center), and the magnitude of the radial component of the Non-Abelian Berry connection element $\boldsymbol{\mathcal{A}}_{\mathrm{HH,LH,+}}$ (right) for tensile strain (upper), zero strain (middle), and compressive strain (right). The units of energy are meV. The units of k are inverse GaAs lattice constant, and the units of the Berry connection are GaAs lattice constant. In the unstrained case, the radial component is universally zero across the Brillouin zone, as we expect from 4.2. In the case of non-zero strain the bands are deformed, as seen on the left, which results in deformation of the Berry connection and non-zero radial Berry connection. The strains in the top and bottom rows correspond to absorption peak splitting of 2 meV. For strains of this size the magnitude of the Abelian Berry connection is on the order of $10^{-7}a_{\mathrm{GaAs}}$ and the magnitude of the non-Abelian Berry connection is on the order of $10^{-2}a_{\mathrm{GaAs}}$. For both strained cases the radial Berry connection is localized to areas where the Bands are most deformed due to strain. In the tensile strain case, there is an avoided crossing which produces the largest Berry connection.

where R_s is the rotation matrix that diagonalizes the total strained block Hamiltonian and $\mathcal{S}_s$ is the matrix,

$$\mathcal{S}_s = \exp\left\{ -\frac{i}{\hbar} \int_{t'}^{t} \mathrm{d}t'' \left[\begin{pmatrix} \varepsilon_{\text{E-HH}}(\boldsymbol{k}(t'')) & 0 \\ 0 & \varepsilon_{\text{E-lH}}(\boldsymbol{k}(t'')) \end{pmatrix} + e\boldsymbol{E}_{\text{THz}}(t'') \cdot \hat{\boldsymbol{\mathcal{A}}}_s(\boldsymbol{k}(t'')) \right] \right\} \tag{4.20}$$

where ε_j is the energy of the strained E-HH or E-LH pair and $\hat{\boldsymbol{\mathcal{A}}}_s(\boldsymbol{k}(t''))$ is the matrix of Berry connections associated with the s block of the Hamiltonian

$$\hat{\boldsymbol{\mathcal{A}}}_s(\boldsymbol{k}(t'')) = \begin{pmatrix} \boldsymbol{\mathcal{A}}_{\text{HH,HH},s}(\boldsymbol{k}(t'')) & \boldsymbol{\mathcal{A}}_{\text{LH,HH},s}(\boldsymbol{k}(t'')) \\ \boldsymbol{\mathcal{A}}_{\text{HH,LH},s}(\boldsymbol{k}(t'')) & \boldsymbol{\mathcal{A}}_{\text{LH,LH},s}(\boldsymbol{k}(t'')) \end{pmatrix}. \tag{4.21}$$

Note that we choose the eigenstates of the block Hamiltonians to be related by time-reversal and inversion symmetry such that they are pseudo-spin partners and the Berry connection components are related by $\hat{\boldsymbol{\mathcal{A}}}_+ = -\hat{\boldsymbol{\mathcal{A}}}_-^{\,*}$.

Importantly, we have neglected the role of dephasing here. The form of the electric polarization in Eq. 4.19 makes the role between the geometric and dynamical phases clear and should provide good information about what the polarization state of the sidebands will be. This is because the E-HH and E-LH experience fairly similar dephasing so the relative difference in dephasing rates should not be a large effect on the polarization state. However, this does obscure relevant information about how strain affects the sideband intensity. Further work could incorporate dephasing into this analysis.

4.3 Effects of Strain on HSG Experiments

With Eq. 4.19 we can in principle calculate the sideband polarizations produced in strained GaAs. The question is, what effects do we expect to see in strained samples that are not present in unstrained samples? And how different would these spectra be compared with the unstrained case? To answer this, we perform numerical calculations to understand the relative size of the dynamical phase in the strained and unstrained case, as well as the size of the Berry connection term in Eq. 4.20.

Performing these calculations we see that in our samples the effects of the geometric phase are not measurable compared to the dynamical phase. The dynamical phase accumulated by electron-hole pairs in our experiments is of order 10. In contrast, the radial component of the Berry connection, which is plotted for different strain cases in Fig. 4.3, is much smaller. A hole traveling on a straight trajectory in strained GaAs would accumulate Abelian geometric phase of order 10^{-8} and non-Abelian geometric phase of order 10^{-3}. Furthermore, although there is some difference between the strained and unstrained dynamical phases, in our samples the difference is less than the experimental error. It is possible that strain effects cause the variation in γ_3/γ_2 we extracted at different angles in Ch. 2. If true, this would suggest that the bi-axial strain approximation is not valid and it is unclear what a good model of strain for our samples would be.

A further complication is that because the two terms in Eq. 4.20 do not commute, they cannot be simultaneously measured. Rather, what is measured is a combination of the total effects of dynamical and geometric phases. It will take careful consideration of what the exact measurable is in a given experiment in order to extract meaningful information.

For these reasons, we have not been able to experimentally extract any information about strain or the resulting phases from sideband polarimetry.

4.4 Proposed Experiments to Measure a Geometric Phase via Sideband Polarimetry

Although we have not been able to perform conclusive experiments in strained GaAs samples, there is some excitement and hope that such experiments could be done and lead to interesting physics. Perhaps the most exciting result would be to measure a geometric phase using sideband generation. This type of geometric phase would be different than the closed loop phases discussed in Ch. 1.2.1. To my knowledge, this type of open path geometric phase has never been measured. In our case, it would only be possible to measure because the interferometric nature of sideband polarimetry gives access to the relative geometric phases of the E-HH and E-LH pairs.

The largest barrier to measuring strain induced phases is a lack of samples with diverse strain. Strain does slightly vary across our samples, but these differences are not enough to test strain dependence. The most promising option is to engineer samples with different strain, especially higher strain. One option is to invest in a piezoelectric strain cell. These cells allow the strain in a sample to be finely tuned, but they are quite expensive and would require significant redesign of our current cryostat system.

Another option is to continue using our current experimental setup but change the samples. The strain in our current samples comes from the interface between the epitaxial layer of GaAs and the substrate, in our case sapphire. We believe that the difference in thermal expansion between GaAs and sapphire is largely responsible for the strain at low temperatures. Looking at temperature dependent absorbance spectra does seem to suggest that the peak splitting gets lower as temperature increases, but the increasing width of the peaks makes it difficult to be sure. By changing the substrate to a material with a thermal expansion coefficient that is more different to GaAs than sapphire could lead to larger strain. Optical quartz is a promising material that can be easily obtained and is transparent to NIR and THz frequencies. The difference in thermal expansion coefficients between quartz and GaAs is also significantly larger than GaAs and sapphire so samples made with quartz should have significantly higher strain. The magnitude of the strain could be characterized with a straightforward use of absorption spectra.

Our current samples have compressive strain, which produces less deformation and strain effects than the tensile case. Using a different substrate, such as quartz, with a smaller coefficient of thermal expansion could lead to tensile strain which would be more measurable.

Once highly strained samples are produced, there are several different possible experiments. The basic idea is that the bigger the strain, the larger the radial Berry connection and therefore the larger the geometric phase. One idea is to see if geometric phase effects turn on after some sideband order. Because the radial component of the Berry connection tends to be strongest in the regime of $\boldsymbol{k}$ space where the Hamiltonian is transitioning from being dominated by the strain term to being dominated by the Luttinger term. As strain increases this area becomes a distorted ring in the $k_x - k_y$ plane with a larger radius. The hypothesis is that sideband orders which do not reach this ring will not feel any geometric phase effects, but those that do will experience the Berry connection.

An extreme version of this experiment is when the hole bands have a large splitting, allowing the possibility of preferentially exciting one hole band over the other with the NIR. In this case, there should be no quantum interference since there will be only one species of hole. Without quantum interference, there can still be some changes to the linear polarization angle α, but there should not be any changes to the angular momentum and therefore there should be no changes to γ. However, if the hole reaches a part of the Brillouin zone with non-Abelian Berry connection then there will be some tunneling to the other hole band. The holes in each band can create sidebands that then interfere. This interference will cause both α and γ to change. In the data, this situation would express itself as the polarization of low order sidebands having a constant γ, that then begins to change after a certain sideband order is reached. The rate of change of γ as a function of sideband order would give insight into the strength of the tunnelling and therefore the size of the non-Abelian Berry connection.

The difficulty with this kind of experiment is that we have never shown that we are able to preferentially excite one band over the other, even with strain splitting. There is a process called adiabatic stabilization, where absorption peaks are broadened when the crystal is subject to a strong THz drive [76]. It is possible that the THz pulse causes the absorption to broaden to the point where both bands are being excited by the NIR. If this is the case, then samples with very large strain, and therefore large splitting, might be able to mitigate this effect and allow for preferential excitation of hole bands.

A completely different type of experiment would involve using elliptically polarized THz drive. This would allow the accumulation of geometric phases even in the unstrained case by producing $\boldsymbol{k}$ space trajectories that are not purely along the radial k direction. There are several THz waveplates in the lab that could be used to induce this elliptical THz polarization. However, introducing non-linearly polarized THz adds several complications to the experiment. First, since ballistic recollision is necessary for sideband generation, fewer and fewer sidebands will be produced as ellipticity is increased. The effect from the Berry connection must be sufficiently large so the THz does not need to be highly elliptical. Second, the effects of the geometric phase will tend to be cancelled by the contributions from different bands.

This cancelletion is caused by two different mechanisms. First, bands that are related by time reversal symmetry, such as the HH_+ and the HH_- states from the two different blocks of the Hamiltonian, have opposite Berry connection. This is because under time reversal, the direction of a given $\boldsymbol{k}$ space trajectory is reversed. Furthermore, for a given Hamiltonian, the total Berry curvature must be zero for a given value of $\boldsymbol{k}$. Since we are working with 2 dimensional Hamiltonians, this means that the Berry curvature from the HH band is the opposite of that from the LH band.

All together, this means that in order to observe a geometric phase using elliptically polarized THz, it is necessary to preferentially excite a particular type of hole. The spin cancellation can be taken care of by using circularly polarized NIR, so as to only excite one pseudospin partner. In order to selectively excite HH or LH, strain again could be very helpful by introducing a significant splitting between the HH and LH.

A similar experiment could take advantage of the anomalous velocity, which is an additional velocity acquired by charged particles experiencing Berry curvature. The anomalous velocity is

$$\boldsymbol{v}_A(\boldsymbol{k}) = -\frac{q}{\hbar}\boldsymbol{E} \times \boldsymbol{\Omega}_n(\boldsymbol{k}) \tag{4.22}$$

where $\boldsymbol{E}$ is the driving electric field and $\Omega_n(\boldsymbol{k})$ is the Berry curvature of the relevant band. In the unstrained case the Berry curvature is always parallel to the electric field, so the cross product with $\boldsymbol{E}$ will be zero. However, deformations caused by strain can cause the Berry curvature to change direction, and in this case the holes can experience an anomalous velocity which points perpendicular to the electric field. The electron does not experience this velocity so this perpendicular anomalous velocity experienced by the hole will decrease the amount of recollisions and therefore a decrease in the sideband signal. Using elliptically polarized THz could counteract this deflection and cause more collisions. Experimentally this would be expressed by a maximum of sideband intensity with nonzero THz ellipticity. The amount of ellipticity that gives sideband signal could be used to determine the size of the Berry curvature. Since the Berry curvature has opposite sign for pseudospin partners and HH-LH partners, the anomolous velocity for pseudospin partners will be opposite. Therefore, for sufficiently large Berry connection the helicity of the THz polarization will increase the contributions from some holes and suppress the contributions from others.

A final point to consider is that it is very possible that the strain is not biaxial, and may have some preferred directions in the GaAs crystal. With increased strain effects from higher strained samples, it is possible that the strain could be extracted by examining the differences in sideband polarizations as the crystal is rotated with respect to the THz.

4.5 Conclusion

Experimental access into precisely how strain affects sideband polarimetry has so far remained elusive. We understand theoretically how strain can change the polarization of sidebands, but the increased complexity of the strained theory has resisted straightforward extraction of either strain information or geometric phases.

In order to successfully extract information from strained GaAs samples, the theory of strained sideband generation must be developed further. At the moment, we lack an understanding of what behavior would indicate smoking gun evidence of geometric phases or strain effects. More work is required so that we have a straightforward quantity to extract, as in Ch. 2 and Ch. 3, or a robust theory that can be directly applied to experimental data without a large numbers of free parameters. At the moment our theory has several free parameters including Luttinger parameters, elements of the strain tensor, the gap of the sample under THz drive, and the total dephasing.

Experimentally, there is also work to do. Perhaps the most important step is to fabricate samples with different strains. Using quartz as a substrate could be a good first step that produces high strain samples. Comparing samples with quartz and sapphire substrates would be a reasonably achievable experiment that allows comparisons for qualitatively different strain environments.

Either way, understanding how the introduction of geometric phases affects sideband polarimetry is a key step in the development of Bloch wave interferometry. Applying sideband polarimetry to condensed matter systems beyond GaAs is exciting in part because of the large number of different types of phases that could be measured. Understanding geometric phases is the next step in developing sideband polarimetry as a powerful Bloch wave interferometer.

Appendix A

Experiment Details

Here I will discuss details relating to our experimental setup and how to run HSG experiments. The experimental apparatus is discussed in greater detail in the dissertations of Hunter Banks and Darren Valovcin [77, 78]. If you are especially interested in the software used to take data, focus on Darren's thesis. I will focus on the equipment that is most often interacted with for experiments.

A.1 Experiment Overview

A.1.1 Beamline Overview

HSG experiments use two beamlines simultaneously, one for the terahertz (THz) and one for the near-infrared (NIR). The THz beamline comes from a pipe from the FEL optical transport system. Immediately after this port, a beam splitter takes a small part of the FEL pulse and sends it to a pyroelectric detector, which we call the pyro. The pyro allows us to measure the power of each THz pulse while simultaneously performing experiments. After the beam splitter we have a pair of wiregrid polarizers, which are used to set the THz field strength. The first polarizer is free to rotate and the second

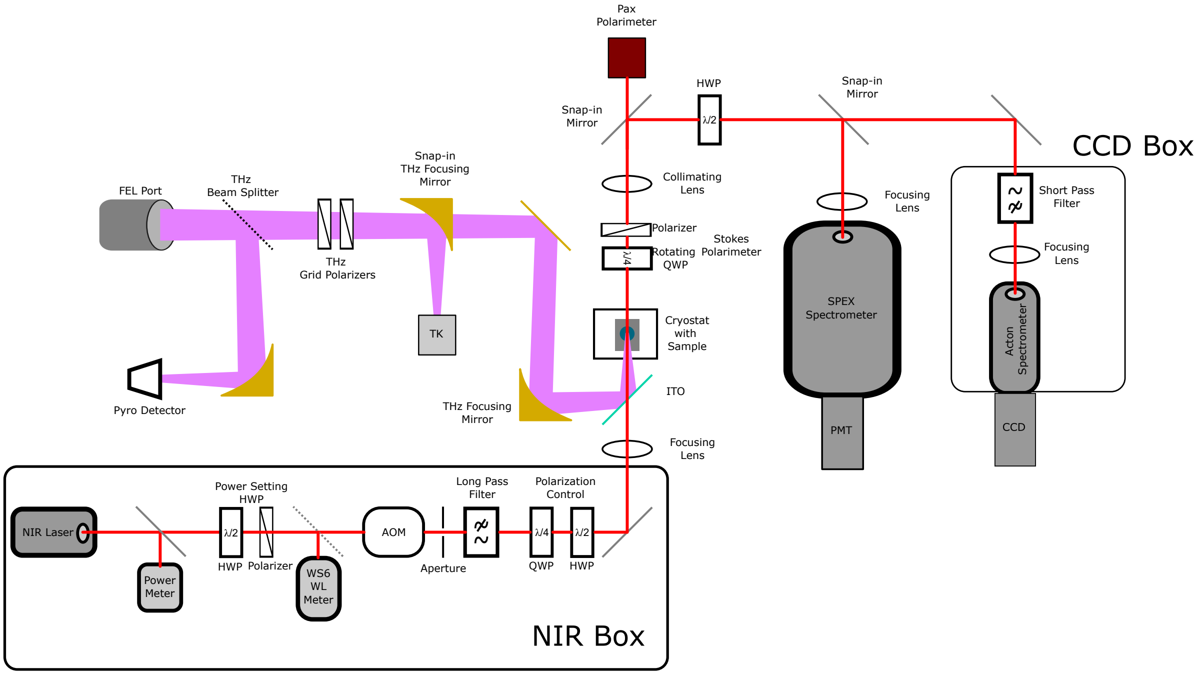

Figure A.1: **HSG Experiment Beamline.** A simplified version of the optics used in HSG experiments. This is not to scale and does not include all optical elements, but I have included the most important ones. The actual physical layout is more complicated, but this cartoon has the general layout.

is fixed with horizontal polarization. By rotating the first polarizer, the intensity of the THz can be tuned. After the wiregrids there is a snap-in off-axis parabolic mirror that focuses the THz pulse onto a Thomas Keating (TK) power meter. The TK is a calibrated detector that gives the amount of energy in the THz pulse and is placed after the wiregrid polarizers so that the amount of measured power corresponds to the amount that will be incident on the sample. Importantly, the Thz pulse should never be directly focused on the TK, it should always be placed away from the focus. In our current setup, the TK is placed behind the focus of the THz. In order to do HSG experiments, the FEL pulse needs to be focused on the sample, not the TK, so the TK focusing mirror must be taken out. Once the TK mirror has been removed, the THz will be reflected off a flat mirror, a focusing off-axis parabolic mirror, and a glass slide with ITO. The ITO slide is transparent to NIR, so after the THz is reflected off of it, the THz and NIR are collinearly focused onto the sample. The sample also has an ITO layer on the back, so the THz does not propagate further in the beamline.

The NIR beamline begins with our M Squared laser, which has two parts. The first is a 7 W green pump laser called the Sprout, made by Lighthouse photonics. The Sprout is used to pump a SolsTiS laser, which takes the green light from the Sprout and converts it to NIR. The NIR wavelength is tunable, and theoretically stable to within 1 pm. In practice we have not been able to lock the wavelength effectively, and have instead tuned it manually to within 10 pm. As the SolsTiS has aged, it has become necessary to tune the coupling between the Sprout and the SolsTiS to top up power. At peak performance, we should expect more than 1 W of NIR power but that has steadily degraded. We keep a paper with the factory tested power ratings as a function of wavelength with the Sprout console.

Immediately after the NIR output is a flip mirror that leads to a power meter. This power meter is protected by an OD 3 neutral density filter, so the real power is 1000 times the measured power. We use a mobile power meter elsewhere in the beamline, but at this point the power is too high and we have to use this fixed filter. After this mirror is a half wave plate and a polarizer. The half wave plate can be rotated to change the amount of light that passes through the polarizer, which is fixed. After these elements, a small beamsplitter picks off a small amount of light that is sent to a WS6-600 wavemeter which monitors the wavelength in real time.

The NIR is then sent through an acousto-optic modulator (AOM). When the AOM is off, the NIR transmits through unimpeded. When the AOM is on, it acts like a diffraction grating. After the AOM an aperture is placed that blocks the 0^{th} order laser peak and allows the first order diffraction peak to pass. This means that by controlling the AOM via an electrical signal we can turn the NIR on and off further down the beamline. We use this to ensure that the NIR is only on the sample when the THz is on. Because the NIR frequency is so fast compared to the timing of the AOM, the NIR still operates in a quasi-CW mode even when the NIR is being pulsed.

After the AOM a long pass filter is used to remove high frequency noise that would otherwise affect sideband signal. This can be tuned by rotating the angle of the filter.

In order to set the polarization state as we like, it is necessary to use a quarter waveplate (QWP) and a half waveplate (HWP). These are located after the long pass filter and are both free to rotate. The polarization is set by removing the cryostat and snap-in mirror after the cryostat to allow the NIR to go into a Thorlabs Pax polarimeter. The Pax provides real time feedback on the polarization state, so you can watch it as you rotate the QWP and HWP. The Pax allows tuning the polarization to within $< 1^\circ$ in α and γ. The full power incident on the sample saturates the Pax, so it's important to use a filter to accurately measure the polarization state. The Pax is quite sensitive to alignment, which can be checked using the alignment assistance tool in the Pax program.

All of the optics up to the polarization control are contained in a box, which I call the

NIR box. This is for safety reasons, since the un-attenuated NIR laser is very powerful. There is a shutter for the box, which is normally closed but can be opened via electronics.

After the NIR box, there is a focusing lens, which focuses the NIR on the sample and the ITO slide which allows the NIR and THz to be colinear. The diameter of the spot is around 500 μm at the sample but can be changed by changing the focus length of the focusing lens. A collimating lens is placed after the sample and the Stokes polarimeter which collimates the now diverging NIR and sideband beam.

Directly after the cryostat is the Stokes polarimeter. Our Stokes polarimeter is home-built, and is capable of measuring much weaker signals than the Pax. It is important that no optical elements are placed in between the cryostat and the Stokes polarimeter when measuring polarizations as other optical elements change the polarization state. The QWP must be plugged in for it to rotate, and offset by 6.6° for proper results. This offset should be set in the softwre. The polarizer should be set to be horizontal. The entire polarimeter is built on a magnetic stage and can be snapped in and out relatively reproducibly. However, over time the polarizer can become misaligned so it is good to periodically check the polarizer by checking the polarization after the polarizer on the Pax. The QWP can also become misaligned, and this usually is shown by rotation angles that are 180° apart having different intensities. The way to align the QWP is to measure the laser line using the CCD (heavily filtered), and look at the polaragrams (intensity vs. QWP angle) produced. When the Stokes polarimeter reproduces the results of the Pax, it is well aligned.

We have two different detectors, with two different spectrometers that use diffraction gratings to select frequencies. The first is a photo-multiplier tube (PMT). The second is a electron-multiplying charge coupled device (CCD). We select them using a snap-in mirror after the snap-in for the Pax. However, the two different gratings have different preferred polarizations. The PMT grating prefers vertical polarization, and the CCD prefers horizontal polarization. A HWP is placed after the Pax mirror that allows changes to the polarization after the Stokes polarimeter. Because the Stokes polarimeter normally has a horizontal polarizer, if you are using the CCD the HWP should be horizontal and if you are using the PMT the HWP should be diagonal. The precise values for the angle on the rotating stage are marked on the stage. If you ever forget this you can look at the laser line in the PMT with the Stokes polarimeter inserted and rotate the HWP. The correct rotation is the one which maximizes signal on the PMT.

With the PMT snap-mirror in, the NIR and sidebands will be directed to the PMT. Our PMT is a Hamamatsu R7400U-20. The PMT is a time resolved detector, and is quite fast with response times of roughly 1 ns. The PMT is attached to the end of the SPEX monochromater, which has resolution of roughly 1 cm^{-1}. The PMT is only able to measure one wavenumber at a time, and measures sideband signal by a boxcar integration. This works by specifying the time when the signal is on in the PMT software, which is compared to the background when the signal is off. For most measurements, we average over ten FEL pulses at each wavenumber. The PMT has a voltage of -700 V or -1000 V applied to it using an SRS high voltage source. Going to -1000 V from -700 V gives a gain of 10. The output from the PMT is sent to a fast preamp to amplify the signal, and then to an oscilliscope. The NIR laser line is strong enough to damage the PMT, so it is necesarry to either block or filter the laser when the SPEX is tuned to the laser line. Low order sidebands can also saturate the PMT, although they are less likely to damage the device it is still important to filter them for accurate data collection. Saturation looks like a flat line on the oscilliscope trace. We have three filters that have been characterized and can be used for PMT measurements, called the white, blue, and triplet filters. The blue filter has cracked and we have replaced it with a red filter. Moonsuk Jang characterized it, but it has yet to be implemented in the software.

Without the PMT snap-mirror, the NIR is sent into the CCD box. This box is helpful because it helps reduce stray light into the CCD. Inside the box is a short pass filter and a focusing lens. The purpose of the short pass filter is to block light from the laser line and low order sidebands that can cause noise in CCD images or saturate the detector. The CCD is an Andor NewtonEM electron-multiplying CCD. This detector is very sensitive and can measure many sidebands simultaneously. This is because the CCD measures a relatively wide range of wavelengths at once by integrating the signal over time. Therefore, the CCD gives no time dependent information. In this way, the CCD and PMT can complement each other experimentally. The CCD must be cooled, usually to $-90°$ C. The wavelengths measured can be tuned using the CCD software to tune the spectrometer settings. The CCD has a gain setting that is usually set to 110. The CCD is extremely sensitive and can be easily damaged by the NIR laser. If the CCD is set to the NIR wavelength it is imperative that you filter the laser before taking an image.

A.1.2 Using the FEL in HSG Experiments

The FEL is of course the key to HSG experiments, and an entire dissertation could be written about it. I will not talk about tuning the FEL here, but I will discuss how to use the FEL during HSG experiments. The FEL pulses on a 1.07 Hz rep-rate. The trigger for the FEL is used to trigger most of the electronics in the HSG experiment. The length of the THz pulse is usually 40 ns because we use the cavity dump mode. The hole-coupler can be used to get long pulses that are several μs long, but the field strength is significantly lower.

We have two ways to measure the strength of the FEL. The first is the fast pyro detector that is always detecting. The second is the TK detector. The TK is calibrated, although it probably should be calibrated more often, and thus can be used to measure the absolute power of the FEL pulse. However, the TK only works if essentially all of the

FEL pulse is directed onto it and therefore cannot be used while also taking data. The way we work with both detectors is to regularly, ideally daily, calibrate the pyro using the TK. The pyro gives measurements in mV and the TK gives measurements in mJ. The pyro calibration software gives a mJ/mV number that can be plugged into the pyro software, which then records the FEL energy with each pulse. The pyro is linked to the same oscilloscope that the PMT uses, and the TK is connected to a different oscilloscope, which normally rests on the ground. It is important to put the frequency of the THz into the TK software, because the sensitivity is different for different THz frequencies. There is a FEL monitoring software that plots the energy of each pulse in real time as it is recorded. This is useful as it allows the user to visually monitor the FEL and know when it's starting to freak out or misfire.

We normally record the FEL energy in mJ, but in theory we are usually working with FEL field strength. The two are related by the equation

$$F_{\mathrm{THz}} = E_{\mathrm{eff}} \sqrt{\frac{2 R_{\mathrm{ITO}} T_{\mathrm{Win}} \varepsilon_{\mathrm{THz}}}{A c \epsilon_0 t_{\mathrm{THz}}}} \tag{A.1}$$

where F_{THz} is the THz field strength, E_{eff} is the enhancement from the ITO layer on the back of the sample, R_{ITO} is the reflectence of the ITO slide that combines the THz and NIR, T_{Win} is the transmission through the cryostat window, $\varepsilon_{\mathrm{THz}}$ is the energy measured by the TK, A is the area of the THz spot (usually a circle with roughly 0.6 mm diameter at 450 GHz), t_{THz} is the length of the THz pulse, and c and ϵ_0 are the standard constants. The ITO has roughly 70% reflectance, and the transmission of the cryostat window is roughly 0.9. It is usually good practice to take an average of the measured field strengths over the length of an experiment, with the standard deviation giving a good uncertainty interval.

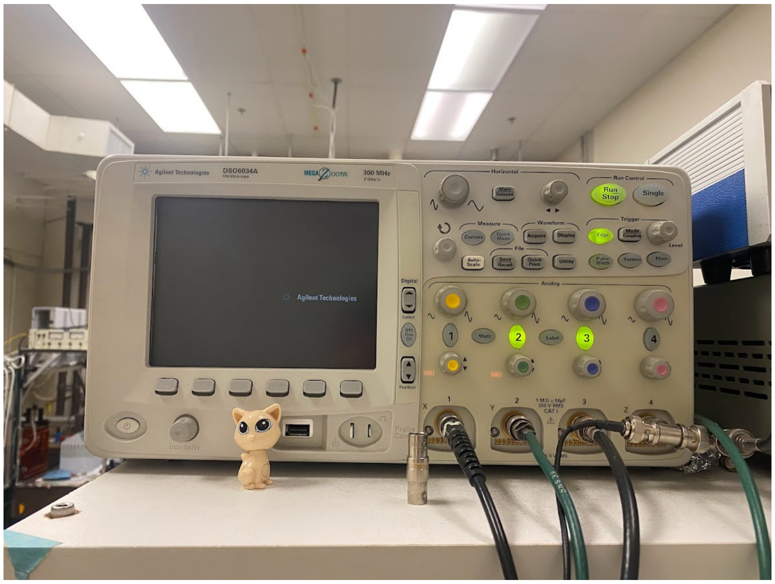

Figure A.2: **Oscilloscope.** The oscilloscope used in HSG experiments. The four inputs correspond to the AOM trigger from the delay generator in channel 1, the PMT output in channel 2, the pyro output in channel 3, and the FEL trigger in channel 4. We trigger off of channel 4.

A.1.3 Electronics

There are several pieces of electronics that we routinely use in experiments. Perhaps the most important is the oscilloscope, shown in Fig. A.2. This oscilloscope is used in data acquisition for the PMT and for monitoring the FEL via the pyro detector. During data aquisition the screen will flash at each trigger, which makes it hard to watch on the screen. You can either keep tabs on it via the oscilloscope software or pause the software, which will make the scope display as normal. If the software has a communication error the scope can get stuck. To fix this, press the Run/Stop button until normal triggering resumes.

The NIR shutter is controlled by the Model SD-10 shutter drive timer, shown in the top of Fig. A.3. Once it is turned on, the shutter has two modes. Normally open (N.O.) mode keeps the shutter open, unless the driver receives a TTL signal. Normally closed (N.C.) mode keeps the shutter closed unless the driver receives a TTL signal. During

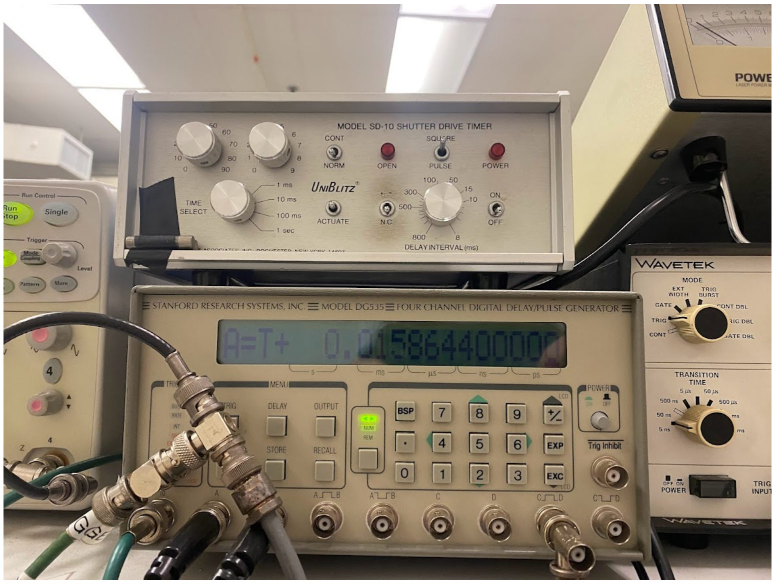

Figure A.3: **Shutter Driver and Delay Generator.** Top: The shutter driver for the NIR box. When closed, no NIR will come out of the box. In normally closed (N.C.) mode the shutter will be closed unless a trigger is received. In normally open (N.O.) mode the shutter will be open unless a trigger is received. The shutter takes several ms to open fully. Bottom: The delay generator used to synchronize the FEL cavity dump laser and NIR. The delay generator is triggered by the FEL trigger. Outputs A and B go to the FEL cavity dump laser. Output C to D goes to the AOM during HSG experiments, so that the NIR is only shining on the sample close to when the THz is on.

alignment, it is better to keep the shutter open, which makes it easier to see the laser. During experiments, it's better to keep the shutter closed, except for the time when the THz is on. This prevents the accumulation of noise from the NIR in our detectors when there are no sidebands because there is no THz. This is done by putting the driver in N.C. mode and turning on the trigger for the driver, which is controlled by a switch hanging near the computer. The shutter is loud, so it's easy to tell when it is on.

The SRS four channel digital delay generator, shown in the bottom of Fig. A.3, makes sure the timing of the FEL and and NIR align. The delay generator is triggered off of the FEL trigger. Delay A is the delay between recieving the trigger and starting the process of firing the cavity dump laser. Tune this delay, which is usually around 15.8 ms, to change when the cavity dump fires with respect to the FEL electron pulse. Delay B is the delay between priming and firing the cavity dump laser, and should never be changed. Delay C to D goes to the AOM, and controls when the NIR is on. Delay C is the time when the AOM turns on and delay D is when the AOM turns off. Using the pyro signal on the oscilloscope, you can adjust C and D such that the NIR turns on when then the FEL arrives and turns off a few hundred ns later.

The Wavetek 2 MHz function generator is used to drive the AOM when a quasi-CW signal is desired, and is shown in the top of Fig. A.4. This is usually done during alignment, as the quasi-CW laser spot looks like it is constantly on. We normally use a square wave with a frequency of roughly 100 kHz, but this frequency is not very important. The square wave has a duty cycle of 50% so any measured powers will be half of the true NIR power. Make sure the power is on and square wave is selected when you want to use the quasi-CW mode.

The bottom of Fig. A.4 shows the AOM driver. This is used to activate the AOM, and let the first order diffraction peak of the AOM propagate through the rest of the beamline. To turn the box on, press the line button, an orange light will turn on when

Figure A.4: **AOM driver and function generator.** Top: The Wavetek function generator used to trigger the AOM in quasi-CW mode. We use a square wave of roughly 100 kHz for a functionally CW NIR signal. Note that because this is a square wave the NIR will have a 50% duty cycle and any measured power will be half of the true power. Bottom: The AOM driver. The driver is turned on by pressing the line button, and the carrier level controls the strength of diffraction. At zero, no signal transmits through the system. At ten, maximum strength transmits. Put the electronic signal on the video input BNC connector. This signal is either from the function generator or the delay generator. The RF output connects the driver to the AOM.

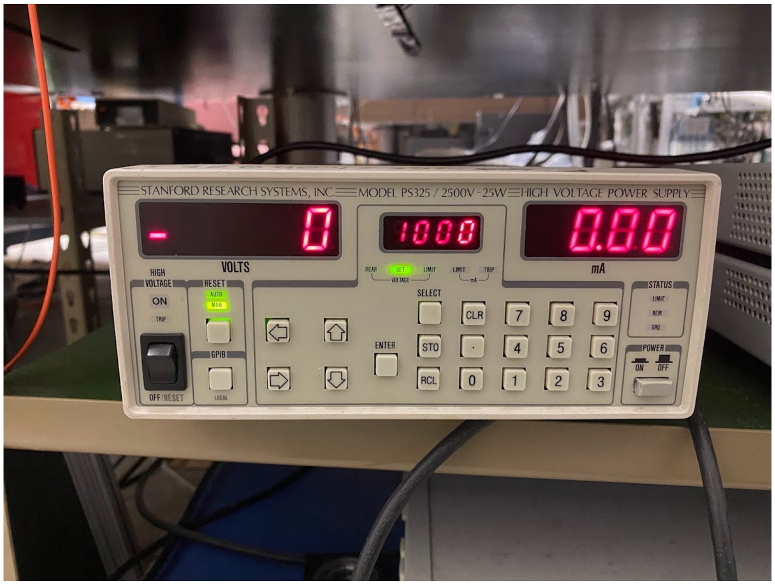

Figure A.5: **High voltage PMT power supply.** The high voltage power supply for the PMT. The left display shows the current output in volts. The central display shows the set voltage. The right display shows the current. In order to change the voltage, press the CLR (clear) button, then push the desired voltage, then hit enter. We use voltages of -700 V and -1000 V during normal operation.

the driver is operational. The carrier level knob adjusts the power deflected. A carrier level of 0 corresponds to the minimum power and a carrier level of 10 corresponds to maximum power. The video input connector is used for the trigger input. For pseudo-CW operation, connect the output of the Wavetek function generator to the video input. For pulsed operation appropriate for HSG experiments, connecct the C to D output of the delay generator to the video input. The RF output connects the driver to the AOM itself.

While using the PMT, we use a Stanford Research Systems model PS325 high voltage power supply, shown in Fig. A.5. In order to use the PMT it is necessary to turn on the power, ensure the correct voltage is set in the center display, and turn the voltage switch (left) on. The volts display on the left should go to the desired voltage. It is also important that the preamp connected to the PMT is powered. The buttons on the power supply are not very responsive, so it might take some effort to set the voltage. In order

Figure A.6: **Temperature controller.** The LakeShore 330 temperature controller. The top left display shows the measured temperature, and the the bottom left display shows the set temperature. When heating is active, the percentage of heater power is shown on the right.

to set the voltage, you first hit the CLR button, then enter the desired voltage, and then hit enter.

The last piece of electronics commonly interfaced with during HSG experiments is the LakeShore 330 temperature controller, shown in Fig. A.6. We mostly interface with this piece of equipment via software, but if the software is malfunctioning you can directly use it with the control panel on the front of the box. The box is connected to a diode thermometer and a heating element that allows PID feedback control of the temperature. This feedback only works when the system is being actively cooled by the cryopump. The procedure for tuning the PID values can be found in the manual for the controller, but I will give a quick set of tips. The PID values stand for proportional, integral, and derivative. The P value corresponds to how much current is provided to the heater for a given difference between the set and measured temperautre. The I value corresponds to the integrated value of the difference between set and measured temperature. Changing the I value changes how far back the feedback loop looks. The D value corresponds to how quickly the feedback responds to the rate of change of the measured Temperature. The PID values will depend on the temperature you want to stabilize at since the time constants of the system depend on the heat capacity of the system.

A.1.4 Cryostat

The sample is housed in a vacuum chamber cryostat. We have two pumps, a rough pump and a turbo pump. The rough pump takes the vacuum chamber from atmosphere to low vacuum, and the turbo takes it from low vacuum to high vacuum. It is important that the rough pump is left to pump for at least an hour before turning on the turbo because exposing the turbo to high pressure will certainly damage it. The turbo pump should be left on for at least 45 minutes before turning on the cryopump, but for best results it is best to leave the turbo on overnight. The turbo cart we use has two different types of pressure gauges. The first is safe to use at high pressure, but bottoms out at 10^{-2} Torr. The rough can easily get below that, but the detector does not show it. The second pressure sensor is an ion gauge, which can measure much lower pressures but is damaged by high pressure. Do not use the ion gauge without the turbo pump being on. With the turbo pump on, the pressure should be around low 10^{-6} or high 10^{-7} Torr.

Once the turbo has been running for a while, it is safe to turn on the cryopump. The cryopump is water cooled, so it is important to open the supply and return valves to Broida water before turning on the pump. The cryopump will cool the sample over a time period of about an hour or two. The better the vacuum the quicker the cooling and the lower the base temperature. In my experience, the base temperature in the best circumstances is around 12 K, but we have been running with base temperatures around 20 K recently. During cooling, once the sample is colder than 77 K, cryopumping becomes more efficient than the turbo. In order to prevent backflow, it is good practice to close the valve between the turbo and the sample once the sample is below 77 K. The cryostat is capable of running overnight if necessary, but this will wear out the pump quickly.

During warmup, the pressure in the cryostat will spike once the temperature is above 77 K and the frozen air begins to sublimate. It is important that the turbo has been spun down for at least an hour before re-opening the valve between the sample and the turbo cart. I usually wait until the temperature is around 100 K.

We have a Lakeshore temperature control box which is hooked up to a diode thermometer and a heating element. The temperature control box has a built in PID control which can be used to stabilize the temperature at any point between room and base temperature. For temperatures below 60 K, I recommend using the medium setting on the temperature controller. For temperatures above 60 K, I recommend using the high setting. These settings control how much current is supplied to the heating element.

A.2 Experiment Procedure

Here I will describe the steps to perform an HSG polarimetry experiment. The day before performing an experiment the cryostat should be loaded with the appropriate sample, assuming it is not already under vacuum. The cryostat should be put under turbo pump overnight. If possible, tuning the FEL to the desired frequency to ensure you have a good file will be helpful.

A.2.1 First Steps

The first thing to do is to turn on the cryopump, assuming that the pressure is ok. This is done by opening the supply and return valves for the cryopump water supply and then turning on the cryopump. Next, you open the temperature monitor software on the computer to monitor the cooling process. The next step is to start the CCD cooler. To do this turn on the chiller, the blue box above the sprout. Next, open the CCD software and set the temperature to $-90°$ C. This should take about 20 minutes to cool, but this is a good opportunity to get things started.

The next step is to turn on the NIR laser and tune it to the appropriate wavelength. This procedure goes as

1. Turn the key on the Sprout to on
2. Press the dial on the Sprout to turn it on
3. Let the Sprout ramp to 7 W (or desired power)
4. On the computer open the M Squared software using Firefox
5. Verify that the M Squared is lasing by checking the Photodiode (PD) voltage
6. Open the WS6 wavemeter and turn it on, making sure you measure NIR
7. Coursely adjust the wavelength setting until you are close to the desired wavelength
8. Finely tune the wavelength by adjusting the etalon.

Note that while adjusting the wavelength setting (Target λ), the wavelength will jump in steps of about 0.5 nm, while the etalon can be used to tune to much higher precision. Ideally the etalon should be left between 30% and 70% to allow tuning throughout the day. When the laser first starts up, the wavelength will drift for the first half hour or so, but after that it shouldn't require too much tuning to maintain stability within 10 pm.

Once this has been done, it is time to tune the FEL and make some coffee. After about an hour, it's good to check on the cryo, closing the sample valve and turning the turbo off once the sample temperature drops below 77 K.

A.2.2 FEL Preparation

Once the FEL is lasing, with the cavity dump laser turned on in Room C, it is time to verify detection of the THz on the pyro. The pyro will show a logistic-like curve if the FEL is lasing but not cavity dumping, and a large jump with oscillations if the FEL is cavity dumping. Adjust the time delay between the FEL trigger and the cavity dump on the delay generator (delay A) until the cavity dump is saturated. Ideally the cavity dump will contribute 90% of the signal. The logistic rise before the cavity dump is called the front porch, and comes from some initial THz light leaking through the cavity before being dumped. Ideally, this is only 10% of the signal. This timing depends sensitively on when the FEL starts lasing. If that changes throughout the day, then the timing will need to be adjusted.

Once the cavity dump is ideally timed, the pyro should be calibrated using the TK. Insert the TK mirror and turn on the TK. Verify that the TK is getting the signal by checking the TK oscilloscope. Then, start the pyro calibration software and enter the frequency of the FEL in wavenumber in the TK part of the program. Set the timings on the pyro part of the program, with red corresponding to backgroun (no signal), blue corresponding to the front porch, and green corresponding to signal peak. Once this is done, hit calibrate and let the program average over several pulses. I usually let it average for a minute or two. Then, take note of the calibration factor in mJ/mV and enter it in the pyro oscilloscope section of each program you take data with.

Whenever you take data using the PMT or CCD software, go into the oscilloscope section and make sure that FEL pulses are being saved. Open the FEL pulse monitor file and load the FEL pulses file to keep an eye on field strengths. Remove the TK mirror and turn off the TK so the THz is incident on the sample.

A.2.3 NIR Preparation

The next step is to set the NIR to the desired polarization. The first thing to do is to set the NIR shutter to be always open and set the AOM to a 50% duty cycle using the function generator and a square wave with a high frequency. Next, insert a filter after the AOM. Using an IR card ensure that the filter is not at an angle by making sure the back reflection goes straight back.

Then, open the Pax software, and make sure that the alignment is good using alignment assistance. Then, using the polarization control waveplates, set the polarization to the desired polarization. Remove the filter and use the power control waveplate to set the desired power at the sample using the handheld power meter. Keep in mind that because this is a 50% duty cycle the true power is twice the displayed number. We usually perform experiments at 100 mW, well within the linear response of the NIR.

A.2.4 Sample Alignment

After fixing the NIR polarization and power, insert the sample, the Stokes polarimeter, and the snap-in mirror before the Pax. Ensure that the HWP after the polarimeter is properly rotated. Then, turn on the optical camera and illumination light. Reduce the AOM intensity to roughly 2 out of 10 so the NIR doesn't overpower the camera. Ensure that the NIR is at the appropriate spot and take a picture, noting the NIR polarization or experimental run in the title of the picture. Then turn off the camera, turn off the illumination light, and reutrn the AOM to 10. Ensure that the NIR is aligned into the proper spectrometer using an IR card. Then, switch the triggering of the AOM to the delay generator from the function generator.

A.2.5 PMT Data Collection

Coarsely align the NIR into the PMT using the irises and an IR card. Make sure the beam block is in before the PMT. Turn on the high voltage power supply, displayed in Fig. A.5, by pressing power and flipping the voltage switch. Then, make sure the preamp is powered. The second channel of the oscilloscope in Fig. A.2 should jump to a nonzero value and should display some noise.

Start the PMT software, called SPEX. In settings, make sure the oscilloscope and SPEX spectrometer are connected to the appropriate hardware address. The spectrometer commonly gets disconnected so it's critical to make sure the proper value is entered. If the spectrometer was disconnected it's a good idea to initialize the SPEX. To do this open the SPEX menu and then go to options and initialize SPEX. A dialogue box will pop up asking for the reading on the side of the SPEX. Walk over and check the number, then enter it into the box exactly as you see it. There will be a 4 wavenumber difference between the software and hardware reading. Next, make sure the NIR and FEL frequencies have been entered into the settings, as well as the voltage on the PMT.

Go into the SPEX menu, and set the SPEX to go to around 4 wavenumber above the NIR frequency. Set the AOM carrier level to 0, make sure that the filters are inserted, and change the AOM triggering to the C to D signal from the delay generator. The supported filters are the white, blue, and triplet filters. Remove the beam block, and slowly ramp up the AOM carrier level until you see a strong signal. If you see no signal, reduce the carrier level to 0, move down 1 wavenumber and repeat this process. It is better to move down wavenumber instead of up because of backlash correction that makes moving up take much more time. If you sweep to 4 wavenumber below the expected NIR frequency and still see nothing, remove a filter and start over. Once you see the NIR, which should look like a bar of raised signal on the oscilloscope, tune the mirrors before the PMT to maximize signal. It is best to use the mirror directly after the polarimeter and the second to last mirror before the PMT to maximize signal. Once signal has been topped out, move a few wavenumbers around to find what your measured peak signal is. Take this wavenumber and set it as the NIR frequency in the settings.

Now, turn the FEL on and move the SPEX to the location of the $n = 2$ sideband. This sideband is usually strong enough that one or two filters will be needed. You may need to move one or two wavenumbers to see the peak of the sideband. Once the peak of the sideband has been found, tune the ITO slide to maximize signal. This ensures that the THz and NIR are maximally overlapping. This is usually good enough to maximize signal, but if you want to be sure the THz and NIR spots are well aligned you can repeat this on the $n = 8$ or $n = 10$ sidebands. These sidebands should be weak enough that you don't need to filter.

To measure a sideband, first create a folder for the data and select it with the choose directory button. After this, put in a save name and a series name. The save name creates a folder, the series name puts a tag in the file. If you want the code to process the sidebands together, it is necessary for all sidebands to have the same series name.

Then, make sure the pyro time regions are properly placed, with the red area on the background, the blue area on the front porch, and the green area on the signal. Make sure you are saving THz pulses. Tune the SPEX to a sideband, usually the 2nd order, and initialize the PMT regions using the Init PMT button. Put the red area on a background time, usually before the NIR has fired, and put the green area where the sideband is. Don't change these areas for later sideband measurements unless you have changed the timing of the delay generator. Then, making sure the PMT voltage and filter settings are correct, enter the sideband number you want to measure and hit start.

Once you hit start, a dialogue box will pop up asking for the sideband number, the plus/minus wavenumber (usually 4), the step (usually -1), and the number of scans to average over (usually 10). Once these values have been confirmed, the program will start a scan, moving to the first wavenumber and recording the signal at each wavenumber the appropriate amount of times. The scan tab of the software lets you watch the data collection progress. It is important that the sideband number entered next to the choose directory button and after you hit start are the same. The former controls the labelling of the file and the latter controls the wavenumbers scanned.

After scanning a sideband, you can simply change the sideband number parameters and scan the next one. One thing to keep in mind is that as you move to higher order sidebands you will be removing filters or changing the voltage on the PMT. It is important that these changes are also changed in the settings because the software automatically takes this into account when scanning, so if they're wrong the scan will be improperly scaled.

It is sometimes desirable to measure the lase line directly. In this case, you usually want to measure with the sample out. Whenever you remove the sample, it is necessary to double check that the sample was returned to the correct spot upon reinsertion. To do this, follow the procedure for aligning the sample again. The PMT takes the average value of the signal over the green area, so it's ok to spread it out for the NIR measurements, which will have signal for longer than sideband measurements. Just be sure to use filters to avoid saturating the detector. When labeling the NIR laser line scan, use sideband number 0.

A.2.6 CCD Data Collection

First, ensure the CCD has cooled to the proper temperature. Sometimes it has trouble getting there and you need to set the temperature to something like -88 degrees. Then open, the slits on the entrance of the CCD. It is standard to open them to around 6 ticks on the micrometer. Each tick corresponds to 10 μm of opening. Next, ensure the oscilloscope part of the CCD program is working. If you have several programs trying to use the oscilloscope they will disconnect so it's always important to check and make sure the one you want is connected. Make sure you're saving FEL pulses.

Next it's time to bin your pixels. For alignment, it's fine to keep your binning at one, but the fewer pixels the quicker the program will respond. There are 400 vertical pixels, but usually only around 180 to 380 are actually useful. The rest are blocked by internal components of the spectrometer. Note that when binning you need to hit apply or nothing will change. If you want to bin multiple pixels together, you need to make sure the vertical start and vertical end match up or it won't set it. If you want to bin 10 and have 4 pixels you would start at something like 201 and end at 240.

Choose a directory and pick a name for the image. Usually we label the image by the polarization state (for example a00 for $\alpha = 0°$) and the polarizer direction. We normally use a horizontal polarizer so we end the image with "HAna" for horizontal analyzer. Then, plug in the rotator for the Stokes polarimeter go to the Misc Tools tab. Hold shift and press the open button, then go to set offset, and set the offset to be 6.6°. You may have already done this during setup.

Next, set NIR paremeters in the image tab. The most important parameters are the NIR wavelength and polarization angles. If you don't put that in later analysis will be all messed up, but it's good to fill all the information. Once you've input the wavelength of the NIR, assuming you've filled out the THz frequency in the oscilloscope tab, you can set the spectrometer and see what sideband orders you will be sensitive to. Never set the spectrometer to be sensitive to the laser line without having filters in. Usually we have the first sideband be the 8th order. Remember to hit set on the spectrometer interface or nothing will happen.

Once the spectrometer has been set, make sure the binning is set to 1, the FEL is on, the AOM is turned up to 10 and triggering off the delay generator, and the NIR shutter is opening on the FEL trigger. Turn the room lights off and take a 0.5 sec exposure with gain 110. If you're worried about noise you can set the gain to 1 first. You should see sidebands. If you don't, you can increase the exposure time. If this still doesn't work, then bin your image in big pixels to increase the speed at which the software processes images. Then change the external shutter to permanently open (being sure to hit apply) and use the take continuous option in other settings. Once continuous images are being taken, try to tune the mirror in front of the CCD box and the mirror directly after the polarimeter until you see sidebands. It is reccomended to use the continuous image mode when tuning the coupling into the CCD, but you must be careful to not saturate the detector. When done, turn off continuous images and set the shutter back to automatic. Since this is done with the polarimeter inserted, it can be helpful to rotate the QWP to 45° if the NIR $\alpha = 90°$, since so little light will get through the polarimeter otherwise.

Once you see sidebands, take an exposure of several seconds with binning of 1. Do not save the image. Then inspect the image, and see how many pixels the sidebands take up. Now, bin the camera such that you have two pixels, one that contains the sideband and one that is dark. For example if the sideband images take up 15 pixels starting at pixel 200, you can bin starting at 200, ending at 229, and binning 15. In the HSG experiment tab, go to settings and make sure the y_min and y_max correctly correspond to your sideband pixel. For example, if you have two pixels, the first one containing sidebands and the second one dark, then y_min should be 0 and y_max should be 1. These numbers control which pixels are saved to the final spectra file.

Once you are properly binned, you can touch up the alignment to maximize signal. If you find yourself tuning the vertical component, you will need to redo the binning procedure.

Next, while in continuous image mode, tune the short pass filter such that the first sideband in your spectrum is roughly the same intensity as the second. This makes sure the maximum amount of noise is removed while ensuring only the first sideband is attenuated. If there is a lot of noise in the wavelengths with sidebands, it is probably a good idea to tune the low pass filter in the NIR box.

Now you are ready to take background. We normally do 10 second integrations. When taking background turn the NIR shutter off, so no NIR is incident on the sample. If there is a lot of noise from the NIR itself, it is sometimes better to do a background measurement with the NIR on and THz off. Take four background images and save each image. You can do this automatically by enabling extra settings in the other settings tab and pressing shift while clicking on the multiple exposures option. Then press the arrow to the right of the take background button to process the background.

With a valid background you can take images. With the NIR and THz firing, press take image. The settings for the image and the background should be identical. After an image the spectra formed from summing the pixels from y_min to y_max is shown on the bottom. Take four images, and press the arrow to the right of the take image button to process them. Processed images subtract the background and average the signal over the four images. This processed image should show on the bottom of the program.

The processed spectrum is saved in the save directory in the spectra folder, and the individual images and backgrounds are saved in the images folder. I have rarely needed to use these, but it's good practice to keep them around in case there's ever any irregularities.

To do a polarimetry scan, we use a functionality called Do HWP Sweep. This is misnamed, since we are sweeping the QWP. To do this, specify a starting angle, a step size, an ending angle, and the number of images to be taken at each angle. We normally do starting angle 0, step size 22.5, ending angle 360, and 4 images. Angles are given in degrees here. The program will take the appropriate number of images at each QWP angle, automatically processing them before moving to the next angle. Normally, this produces 16 images that can be used to extract the polarization state of the measured sidebands.

A.2.7 Shutdown

The CCD must warm up before being turned off. Luckily, the program knows this so pressing close will automatically cause the program to set the camera to warm up. Once the CCD is above 0° you can close the program. Then close the CCD slits and turn off the blue chiller.

The sample must also warm up. Turn the cryopump off and close the water supply and return. Then, set the heater temperature set to 270 K with the medium setting. This will warm up the sample over about 30 minutes to an hour. Once the sample is well above 70 K (I usually wait for 100 K), you can open the valve to the rough pump. The pressure will spike, wait to make sure the rough brings the pressure down again. After about 15-30 minutes you can turn the turbo on again.

While this equipment is warming up, you can do the rest of shutdown. Press the Sprout power button to turn it off, then turn the key away from on. Turn the PMT high voltage off. Turn the shutter driver, AOM drive, and Wavetek function generator off.

Close any unwanted programs on the computer, and be sure to complete the FEL shutdown procedure. Then enjoy the rest of your day!

Appendix B

Python Software

The software we use to analyze data and perform experiments is, for the most part, written in python. When I began my PhD Darren Valovcin had already led an effort to write the data acquisition software in python, instead of labview. He had also written a great deal of code focused on performing polarimetry experiments and extracting Jones matrices.

However, a great deal of HSG code, called HSG-turbo, was contained in a single file called newhsganalysis. This made it difficult to track and find functions. Cameron Cannon and I added a few functions and reorganized the code into a new package called stele. Stele splits up the various functions and objects into different folders and files to allow easier understanding of where different parts of analysis are being done. It is designed to be run in a virtual environment, which ensures that the proper package versions are used.

This appendix details the structure of stele, including how to install the package, as well as some notes on the state of other HSG software and possible projects for the future. I recommend that any students working with HSG to have some familiarity with python.

The HSG code repositories can be found on the Sherwin group github page, `https://github.com/SherwinGroup`. The repositories used in HSG are

- HSG-turbo: An older collection of HSG analysis and processing code, kept for backwards compatibility.
- Stele: The new and preferred package for HSG data analysis and processing.
- InstrumentLibrary-yolo: A collection of programs used to operate miscellaneous equipment in the HSG lab.
- EMCCD-psychic: Code to run the CCD for HSG experiments.
- SPEXSidebands-fuzzy: Code to run the PMT for HSG experiments.

Of these repositories, I will focus on stele because I helped develop it. The thesis of Darren Valovcin goes into more detail on how the various instrumentation programs work [78].

B.1 Installing Stele

The first step to install stele is to get access to stele from GitHub. This is possible by joining the SherwinGroup GitHub group or by forking the package for personal development. The stele code can be found at `https://github.com/SherwinGroup/Stele`.

Once this has been accomplished, the next step is to make a virtual enviroment to run stele in. To do this on Windows, create a folder to house the virtual environment and then, using the command prompt, run the command

```
python -m venv Path
```

to create the virtual environment. Here, Path is the filepath of the folder hosting the virtual environment. This command creates a fresh installation of python in this folder. You then activate the virtual environment by running the command

```
Path\Scripts\activate
```

from command line. This activates the virtual environment, and the name of the virtual environment should appear in parentheses to the left of the file location on the command line. The next step is to use pip to install stele with the command,

```
pip install GitHubPath\Stele
```

where GitHubPath is the folder containing your GitHub files and Stele is the folder containing the stele files. This should install stele, you can test this by running python from within the virtual environment and trying to import some functions from different files.

There appears to be some outdated methods used in the pip installation and this may require some attention in the future. It is important that the legacy versions of some packages are used, since some have had updates which break the package. Of specific interest is PyQt5, which is used for several data visualization and GUI applications but breaks the package upon updating. It would probably be good to go through and use a different package instead of PyQt5, but this is a significant undertaking especially for the instrumentation libraries.

There are many text editors that are used for running and developing code, but I recommend using one that has built in virtual environment support. I use Atom text editor with the virtualenv package.

B.2 Using Stele

The purpose of stele is to take the data files output by the CCD and PMT programs, process them in a variety of ways, and perform analysis of these spectra. Most of these programs deal with sideband experiments, but code for other experiments such as absorption also exists.

Fig. B.1 shows the structure of stele. I have not used all files or folders, and I have marked these objects in red. Altough they could be useful in the future they are not currently used in sideband analysis. Folders I have used are marked by purple rounded rectangles and python files I have used are represented by green rectangles with sharp corners.

At the highest level, stele can be organized into three different folders called analysis, processing, and UI. Processing takes data directly from the instrument output and converts it into useful quantities. For example, processing functions can take a CCD image, which is signal counts as a function of wavelength, and convert it to sideband intensity as a function of sideband order or energy. The next major folder is called analysis, which takes this sideband information and performs analysis on them. Examples of analysis functions include stitching together different scans into a single image or combining PMT and CCD data together. The last major folder is called UI and has to do with data visualisation. This is leftover from Darren's custom plotting software, but I prefer to use other plotting software so I don't have a good understanding of how the UI code works.

B.3 Processing

We begin with the processing code since it is the beginning of our data pipeline. This folder can be broken down into three folders, processing_hsg, processing_jones, and

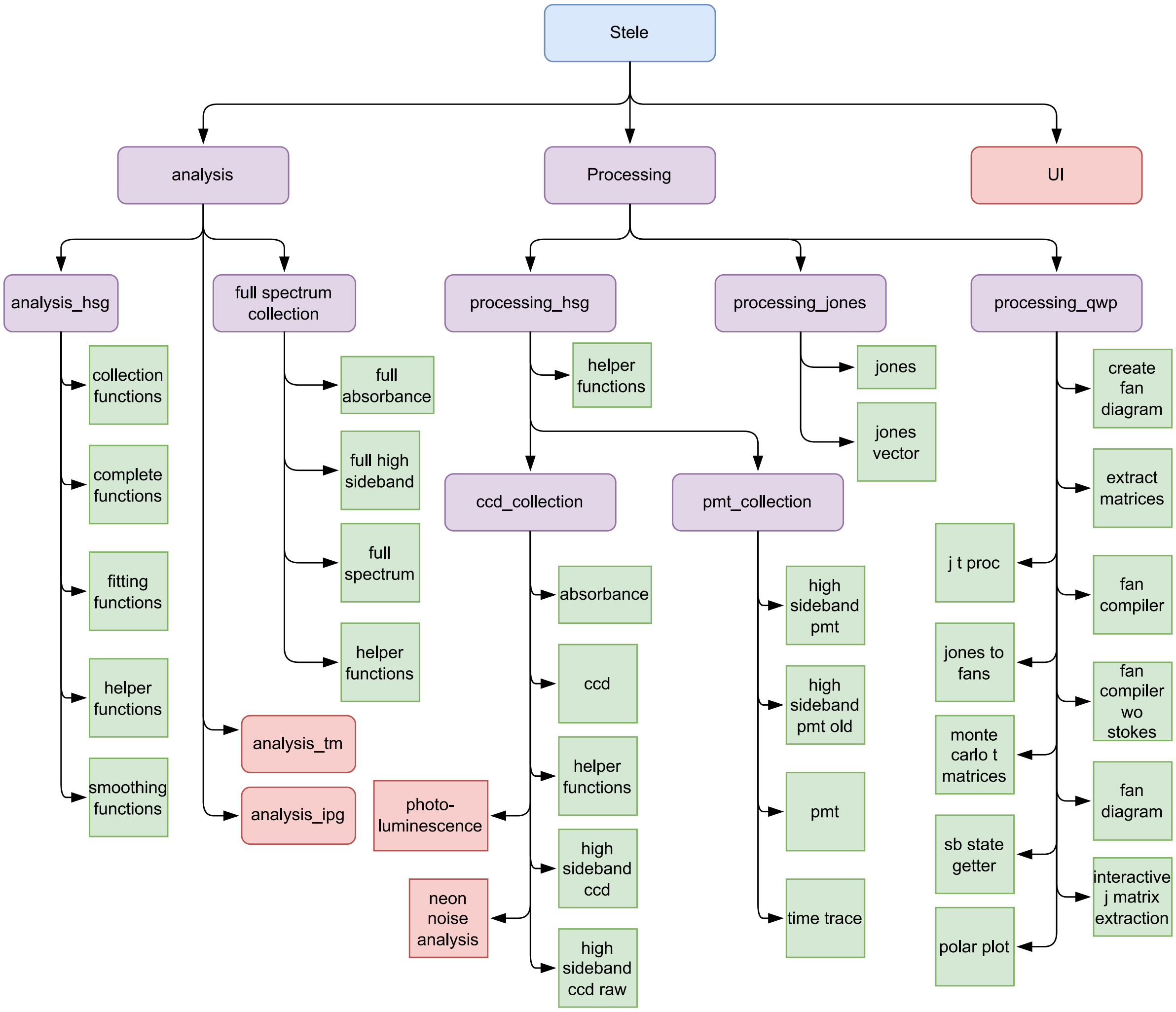

Figure B.1: **Stele package.** The file structure of the stele code package. The blue rounded corner rectangle represents the full package. Purple rectangles with rounded edges correspond to folders. Green recteangles with sharp corners correspond to python files. Red rectangles with rounded edges correspond to folders containing code that I have never used, and red rectangles with sharp corners correspond to python files I have never used. Arrows point from folders to the contents of that folder.

processing_qwp.

B.3.1 Processing HSG

Processing_hsg contains the code most directly related to to detecting sidebands from raw spectra. This is divided into three categories, a folder dealing with CCD spectra called ccd_collection, a folder dealing with PMT spectra called pmt_collection, and a file of miscellaneous helper functions called helper_functions. There are several files called helper_functions, so it is important to pay attention to which file you need. This particular helper_functions file contains a variety of miscellaneous functions used elsewhere in the processing code.

The ccd_collection folder contains the files used for interacting with CCD files. The fundamental object we use is defined in the ccd.py file, called CCD. This is the basic object for all CCD processing, and mostly covers the task of importing images from the camera. The output of this is an array of wavelength, data at that wavelength, and error at that wavelength. This error is usually calculated as the standard deviation between multiple image acquisitions. Note that this code deals mostly with the spectra files produced by the CCD software, not the more fundamental image files. Spectra files are the result of multiple image files. A further difference is that spectra files record data and error for each wavelength, while image files record intesity at each pixel and provide a two-dimensional image.

For HSG experiments, we use a sub-object of CCD called HighSidebandCCD which is defined in the high_sideband_ccd.py file. This file covers the task of taking a sideband spectra and finding the sidebands. The actual process of doing this is complex, but the general idea is that the program looks for peaks where we expect sidebands to be. This results in the creation of the array sb_results which gives the processed sideband spectra with 6 columns, [sideband order, frequency (eV), frequency error (eV), Gaussian area, area error, Gaussian linewidth, linewidth error].

Another sub-object of HighSidebandCCD is HighSidebandCCDRaw, which does some processing for image files, so that you know the wavelengths of the image along with the image data. This object is defined in the high_sideband_ccd_raw.py file.

For absorbance experiments (sometimes also called absorption), we use the Absorbance object which is defined in the absorbance.py file. Absorbance is a sub-object of CCD, but not HighSidebandCCD. Absorbance experiments compare spectra taken with and without the sample in the beampath for a broad spectrum white light. The data without the sample present is called the reference or ref data, and the data with the sample present is called the raw data. The processed data is calculated via the equation

$$\text{Proc} = -10 * \log 10\left(\text{Raw}/\text{Ref}\right). \tag{B.1}$$

There is also code to save the processed data, and perform some smoothing via Fourier transform to remove high frequency components.

There are also objects for neon noise analysis and photoluminescence. I haven't performed these experiments, so my knowledge of the code is rudimentary. Neon calibration is an experiment to characterize the diffraction grating, comparing the measured frequency of various neon lines to the known value. Supposedly the NeonNoiseAnalysis function in the neon_noise_analysis.py file does something to the noise to help processing. There are some interesting notes here, but what is actually going on is not clear to me. The Photoluminescence object, defined in the photoluminescence.py file just normalizes the data to exposure times.

The last file in the ccd_collection folder is another helper_functions file. This file contains a dictionary called photon converter to help with unit conversion between nm, eV, and wavenumber, and two functions. The first function is called calc_laser_frequencies that claculates the NIR and FEL frequencies for a given sideband spectrum. The second function is called low_pass_filter and removes high frequency noise, usually in absorbance spectra.

We now move to the pmt_collection folder. The basis of this set of code is the PMT object, defined in the pmt.py file. This file is very short, it just adds various parameters into a dictionary called parameters that can be inherited and referenced later.

Most of the processing for PMT experiments is done with the HighSidebandPMT object, a sub-object of PMT, which is defined in the high_sideband_pmt.py file. The object has functions that add sidebands to its results, as well as integrating the data to get the full sideband strength, or fitting them to a Gaussian. There is also a function that can scale all of the data to a laser line, if the laser line has been measured and included in the file. There is also a function, not part of the object, which sorts a folder of PMT files into a list of HighSidebandPMT objects called pmt_sorter. Since each pmt file can hold only one sideband this is useful to obtain a full sideband spectrum. The key output of this object is the sb_results array, which is similar to the CCD version. The columns are [sideband order, frequency (eV), frequency error, integrated area, area error, linewidth (eV), linewidth error (eV)].

There is also an older version of this object, called HighSidebandPMTOld defined in high_sideband_pmt_old.py. This was replaced in 2017 and I've never used it, but its still here if the new object ever breaks for some reason.

The last file in the pmt_collection folder is called time_trace but it currently has no real implementation. I think the idea is to take the raw data from the PMT time traces and do something with it.

B.3.2 Processing Jones

Now that we have discussed the processing_hsg folder, we move to the processing_jones folder. This folder is relatively small, and has only two files, jones.py and jones_vector.py. We first consider jones.py, which contains various functions to help with Jones calculus. These functions are usually called in other places.

The file jones_vector.py is where the JonesVector object is defined. This object contains various ways to work with polarization states. There are three different ways to define a polarization state using this object. First, you can specify the E_x and E_y of the electric field. This vector is normalized such that the E_x component is real. The second way that the polarization state can be defined is by specifying ϕ and δ. The corresponding Jones vector is

$$\boldsymbol{E} = \begin{pmatrix} \cos\phi \\ e^{i\delta}\sin\phi \end{pmatrix} \tag{B.2}$$

. Geometrically, ϕ is the angle between the linear polarization angle and the x direction, and δ is the phase delay between the x and y components. The final way to define the polarization state is to use α and γ from Ch. 1. The functions in the jones_vector.py allow you to switch between these representations, as well as performing various transformations to the polarization.

B.3.3 Processing QWP

The final folder in the processing folder is processing_qwp. This folder is named after the quarter wave plate in the polarimeter, and is largely concerned with processing polarimetry scans and extracting Jones matrices. Note that these functions do not primarily deal with the extraction of polarization, but the compilation of different polarization scans and the extraction of Jones matrices from these scans.

The first step in extracting Jones matrices is to collect the data from different polarization scans together. This is done through the FanCompiler object, defined in the fan_compiler.py file. The two functions commonly used are the addSet function, which adds the fit dictionary from a polarization scan to the set of scans, and the build function which gives an array of alpha, gamma, and the intensity Stokes parameter S_0 for all sidebands and NIR polarization states. There is also the buildAll function, which returns all of the Stokes parameters, not just S_0. The build functions return two dimensional arrays where rows correspond to sideband order and columns correspond to a NIR polarization run. These polarization runs are usually denoted by the NIR α, since we usually use linear NIR polarizations. Error in these values are sometimes also stored as their own column.

There is also a version of the FanCompiler called FanCompilerWithoutStokes, defined in the fan_compiler_wo_stokes.py file. This file is very similar to FanCompiler but it doesn't use any Stokes parameters. This file is mostly deprecated.

Once the polarimetry data has been collected in a FanCompiler, the Jones matrices can be extracted using the functions in the extract_matrices.py file. The function findJ extracts the Jones matrix given the α and γ arrays produced by FanCompiler. This extraction is done by minimizing a function defined in the solver function that compares the NIR state mapped by the Jones matrix to the measured sideband state. An important note here is that the Jones matrix is normalized such that J_{xx} is always equal to 1. We can do this because we are working with normalized Jones vectors, and therefore the polarization state is always arbitrary up to an overall complex number. The other important function in this file is makeJfromT, which rotates the Jones matrix to the circular basis. This rotation is done via a unitary matrix defined in the function makeU. Our notation is that J refers to a Jones matrix in the $x-y$ basis and T refers to a Jones matrix in the circular basis. Other functions in this file allow the saving and loading of

Jones matrices, and the ability to go back to J from T.

The analysis and processing of a polarimetry scans is contained in the file j_t_proc.py with the function J_T_proc. This function takes the set of polarimetry scans, the sidebands you want the code to find, and the crystal angle from the [010] crystal face. The function then does everything necessary to get the α and γ for each sideband, the J matrix, the T matrix, the magnitude of T_{++}/T_{--} and T_{+-}/T_{-+}, the argument of T_{++}/T_{--} and T_{+-}/T_{-+}, and the degree of polarization for each sideband. This file is great for understanding the general flow of how the code handles polarimetry. Many of the functions used in j_t_proc.py are from the analysis folder.

The file monte_carlo_t_matrices.py contains a partially developed error calculation mode. This code was updated and eventually used as function not in the package itself. It would perhaps be smart to update this file to host the newest Monte Carlo code, which can be found in my folder on the Sherwin Group shared drive in the Processed Data folder. Error analysis of Jones matrices is tricky, and the error in α and γ do not cleanly propagate into the Jones matrix elements. There probably is a way to do this analytically, but we have decided to use a monte carlo simulation to perform the error analysis. This is done by randomly sampling Gaussian distributions of α and γ, with the standard deviation of these distributions set by the error in α and γ. Each random sampling is used to extract a Jones matrix, and repeated several thousand times. The full extracted Jones Matrix in this case is the average of all these elements, and the error is the standard deviation. This error can then be propagated through to the circular basis or the ς formulation.

The file sb_state_getter.py contains an object called SbStateGetter. This object produces a dictionary of sideband polarization states and has a function getSBState that makes it easy to get a given sideband polarization.

The remaining files in the folder are designed to produce fan diagrams. These fan diagrams are designed to portray different polarization states of sideband spectra as polar plots. For more information, see the dissertation of Darren Valovcin [78]. These files were probably broken by PyQt5, but could potentially be made to work in the future. We no longer use fan diagrams at all, so I haven't taken the trouble to fix this code. The files involved in fan diagrams are create_fan_diagram.py, fan_diagram.py, interactive_j_matrix_extraction.py, jones_to_fans.py, and polar_plot.py.

B.4 Analysis

The other primary folder in stele is the analysis folder. This folder has four subfolders, analysis_hsg, full_spectrum_collection, analysis_tm, and analysis_ipg. Of these, I have used analysis_hsg and full_spectrum_collection, so I will only cover these folders. The folder analysis_tm hosts the theory matrix code. This was written by Seamus O'Hara, but has largely been replaced by other codes mostly written by Qile Wu. The last folder, analysis_ipg contains code having to do with the in-house plotting software devloped by Darren Valovcin, but I have never used it.

B.4.1 Analysis HSG

analysis_hsg contains five files, dealing with a variety of useful analysis scripts. The first is collection_functions.py, which contains various functions that collect different types of sideband spectra. The function hsg_combine_spectra allows multiple HighSidebandCCD objects together. Notably this function does not work with PMT spectra, it is used to stitch together CCD scans taken at different wavelengths. This allows the measurement of more sidebands than normally fit in a single spectrometer scan. A similar function, hsg_combine_spectra_arb_param allows for different scans over things like field strength, instead of just sideband order. A copy of pmt_sorter is in this file as well, this is most likely an oversight but it does the same thing as the other instance of this function. The function hsg_combine_qwp_sweep processes a list of polarimetry scans into a matrix of sideband strength at different QWP angles. This output should be passed directly into fitting. The function proc_n_fit_qwp_data fits the results of hsg_combine_qwp_sweep using the curve defined in the function makeCurve, or by using Fourier analysis. The fits from these functions give the Stokes parameters, α, and γ.

The next file is called complete_functions.py. This file contains functions which process PMT and CCD data, and then combines the two. The first function in the file is called proc_n_plotPMT, which takes a folder of PMT files and processes it completely using pmt_sorter and the integrate_sidebands function from HighSidebandPMT. The next file is called proc_n_plotCCD, which takes a list of CCD files and process it completely. This function creates a list of HighSidebandCCD objects and uses the functions guess_sidebands and fit_sidebands to process them. This list doesn't do any combining of CCD spectra, each spectra is processed seperately. These proc n' plot functions are the workhorses for looking at individual spectra. They contain everything needed to find and fit sidebands. The last function in this file is create_full_spectra, which combines PMT and CCD data. The data needs to be contained in a folder that has the CCD spectra and a sub-folder called PMT that contains the PMT data. The stitching is done with the function stitch_hsg_dicts from the full_spectrum_collection folder's helper_functions.py.

The file fitting_functions.py contains a variety of functions used in fitting. These functions are usually quite general, and used with the Scipy optimize package.

The file smoothing_functions.py contains a variety of functions that smooth functions. Examples include band pass filters that use Fourier transforms to remove either high or low frequency noise and a Savitzky-Golay filter. I haven't deeply investigated this code, but it can be useful for smoothing in some contexts.

The last file in analysis_hsg is helper_functions.py. This file contains several miscellaneous functions. The most important function here is natural_glob, a useful collection function that sorts files more naturally than the built in glob function. For example python would sort the numbers 1, 2, 10, 20 as 1, 10, 2, 20. Our natural_glob sorts files in the more natural way. The other noteworthy function in this file is fvb_crr, which is some sort of cosmic ray removal. I do not know how this function works and I believe this is adapted from much older code.

B.4.2 Full Spectrum Collection

The other important folder in analysis is the full_spectrum_collection folder. This folder contains five files. Most of these files are based on the FullSpectrum object in the full_spectrum.py file. The idea is that this object provides the structure for full spectrum objects that take different spectra and stitch them together in different ways. However, this functionality has not been implemented fully and FullSpectrum contains no functional code. The file full_absorbance.py contains a sub-object of FullSpectrum called FullAbsorbance but is not currently implemented. The next file is called full_high_sideband.py and contains the FullHighSideband object. The idea of this object is that the object starts with a CCD spectra and then expands to stitch together other CCD spectra and PMT spectra. This file has the ability to add PMT and CCD spectra to the overall data using the add_PMT and add_CCD functions. Importantly, there is a function called remove_sp_sb which removes the lowest energy sideband from a CCD spectra. This is usually done because the lowest energy sideband is usually heavily damped by the short pass filter before the CCD. The final file in this folder is another helper_functions.py. This folder contains two versions of the stitch_hsg_dicts, the function that does most of the legwork in actually stitching together different HSG spectra.

B.5 Conclusion

This overview of stele should give the reader a decent overview into the structure of the package, but ultimately practice is the best way to see how these things are done. I reccomend going through my Processed Data folder to see how various analyses were done. In the future, it will probably be important to update the package with additional code, and a good understanding of how the package currently works is critical to this task.

Bibliography

[1] P. Hariharan, *Optical Interferometry (2nd Edition).* Elsevier, London, 2nd edition ed., 2003.

[2] L. de Broglie, *The reinterpretation of wave mechanics*, *Foundations of Physics* **1** (Mar., 1970) 5–15.

[3] L. De Broglie, *Waves and Quanta*, *Nature* **112** (Oct., 1923) 540–540.

[4] G. P. Thomson and A. Reid, *Diffraction of Cathode Rays by a Thin Film*, *Nature* **119** (June, 1927) 890–890.

[5] C. J. Davisson and L. H. Germer, *Reflection of Electrons by a Crystal of Nickel*, *Proceedings of the National Academy of Sciences* **14** (Apr., 1928) 317–322. Publisher: Proceedings of the National Academy of Sciences.

[6] Y. Hasegawa and P. Avouris, *Direct observation of standing wave formation at surface steps using scanning tunneling spectroscopy*, *Physical Review Letters* **71** (Aug., 1993) 1071–1074.

[7] M. F. Crommie, C. P. Lutz, and D. M. Eigler, *Imaging standing waves in a two-dimensional electron gas*, *Nature* **363** (June, 1993) 524–527.

[8] E. J. Heller, M. F. Crommie, C. P. Lutz, and D. M. Eigler, *Scattering and absorption of surface electron waves in quantum corrals*, *Nature* **369** (June, 1994) 464–466.

[9] B. G. Briner, P. Hofmann, M. Doering, H.-P. Rust, E. W. Plummer, and A. M. Bradshaw, *Observation of interfering Bloch waves*, *Europhysics Letters* **39** (July, 1997) 67.

[10] I. Neder, N. Ofek, Y. Chung, M. Heiblum, D. Mahalu, and V. Umansky, *Interference between two indistinguishable electrons from independent sources*, *Nature* **448** (July, 2007) 333–337.

[11] J.-Z. Jin, H. Liang, X.-R. Xiao, M.-X. Wang, S.-G. Chen, X.-Y. Wu, Q. Gong, and L.-Y. Peng, *Michelson interferometry of high-order harmonic generation in solids*,

Journal of Physics B: Atomic, Molecular and Optical Physics **51** (July, 2018) 16LT01.

[12] T.-Y. Du, D. Tang, and X.-B. Bian, *Subcycle interference in high-order harmonic generation from solids*, *Physical Review A* **98** (Dec., 2018) 063416.

[13] M. Hohenleutner, F. Langer, O. Schubert, M. Knorr, U. Huttner, S. W. Koch, M. Kira, and R. Huber, *Real-time observation of interfering crystal electrons in high-harmonic generation*, *Nature* **523** (July, 2015) 572–575.

[14] O. Schubert, M. Hohenleutner, F. Langer, B. Urbanek, C. Lange, U. Huttner, D. Golde, T. Meier, M. Kira, S. W. Koch, and R. Huber, *Sub-cycle control of terahertz high-harmonic generation by dynamical Bloch oscillations*, *Nature Photonics* **8** (Feb., 2014) 119–123.

[15] Y. W. Kim, T.-J. Shao, H. Kim, S. Han, S. Kim, M. Ciappina, X.-B. Bian, and S.-W. Kim, *Spectral Interference in High Harmonic Generation from Solids*, *ACS Photonics* **6** (Apr., 2019) 851–857.

[16] C. Eisele, A. Y. Nevsky, and S. Schiller, *Laboratory Test of the Isotropy of Light Propagation at the 10ˆ-17 Level*, *Physical Review Letters* **103** (Aug., 2009) 090401.

[17] LIGO Scientific Collaboration and Virgo Collaboration, *Observation of Gravitational Waves from a Binary Black Hole Merger*, *Physical Review Letters* **116** (Feb., 2016) 061102.

[18] D. H. Goldstein, *Polarized Light.* CRC Press, Boca Raton, 3 ed., Jan., 2017.

[19] R. Shankar, *Principles of Quantum Mechanics.* Springer, New York, second edition ed., 2014.

[20] F. Schwabl, *Quantum Mechanics.* Springer, New York, fourth edition ed., 2007.

[21] M. V. Berry, *Quantal phase factors accompanying adiabatic changes*, *Proceedings of the Royal Society of London. A. Mathematical and Physical Sciences* **392** (Jan., 1997) 45–57.

[22] R. G. Littlejohn, *Adiabatic Invariance, the Geometric Phase, and the Bohrn-Oppenheimer Approximation*, 2021.

[23] F. Bloch, *Über die Quantenmechanik der Elektronen in Kristallgittern*, *Zeitschrift für Physik* **52** (July, 1929) 555–600.

[24] N. W. Ashcroft and N. D. Mermin, *Solid State Physics.* Cengage Learning, 1976.

[25] D. Xiao, M.-C. Chang, and Q. Niu, *Berry phase effects on electronic properties*, *Reviews of Modern Physics* **82** (July, 2010) 1959–2007.

[26] J. L. Skinner, *Theory of Pure Dephasing in Crystals*, *Annual Review of Physical Chemistry* **39** (1988), no. 1 463–478.

[27] D. Hsu and J. L. Skinner, *Nonperturbative theory of temperature-dependent optical dephasing in crystals. I. Acoustic or optical phonons*, *The Journal of Chemical Physics* **81** (Dec., 1984) 5471–5479.

[28] D. Hsu and J. L. Skinner, *Nonperturbative theory of temperature-dependent optical dephasing in crystals. III. Comparison with experiment*, *The Journal of Chemical Physics* **83** (Sept., 1985) 2107–2115.

[29] D. Hsu and J. L. Skinner, *Nonperturbative theory of temperature-dependent optical dephasing in crystals. II. Pseudolocal phonons*, *The Journal of Chemical Physics* **83** (Sept., 1985) 2097–2106.

[30] Q. Ficheux, S. Jezouin, Z. Leghtas, and B. Huard, *Dynamics of a qubit while simultaneously monitoring its relaxation and dephasing*, *Nature Communications* **9** (May, 2018) 1926.

[31] I. Neder, M. Heiblum, D. Mahalu, and V. Umansky, *Entanglement, Dephasing, and Phase Recovery via Cross-Correlation Measurements of Electrons*, *Physical Review Letters* **98** (Jan., 2007) 036803.

[32] J. M. Luttinger and W. Kohn, *Motion of Electrons and Holes in Perturbed Periodic Fields*, *Physical Review* **97** (Feb., 1955) 869–883.

[33] L. C. Lew Yan Voon and M. Willatzen, *The k·p Method.* Springer, New York, 2009.

[34] P. Y. Yu and M. Cardona, *Fundamentals of Semiconductors.* Graduate Texts in Physics. Springer, New York, fourth edition ed., 2010.

[35] M. Kasevich and S. Chu, *Measurement of the gravitational acceleration of an atom with a light-pulse atom interferometer*, *Applied Physics B* **54** (May, 1992) 321–332.

[36] C. Solaro, C. Debavelaere, P. Cladé, and S. Guellati-Khelifa, *Atom Interferometer Driven by a Picosecond Frequency Comb*, *Physical Review Letters* **129** (Oct., 2022) 173204. Publisher: American Physical Society.

[37] I. Neder and F. Marquardt, *Coherence oscillations in dephasing by non-Gaussian shot noise*, *New Journal of Physics* **9** (May, 2007) 112.

[38] I. Neder, F. Marquardt, M. Heiblum, D. Mahalu, and V. Umansky, *Controlled dephasing of electrons by non-gaussian shot noise*, *Nature Physics* **3** (Aug., 2007) 534–537.

[39] S. Ghimire and D. A. Reis, *High-harmonic generation from solids*, *Nature Physics* **15** (Jan., 2019) 10–16.

[40] H. Liu, Y. Li, Y. S. You, S. Ghimire, T. F. Heinz, and D. A. Reis, *High-harmonic generation from an atomically thin semiconductor*, *Nature Physics* **13** (Mar., 2017) 262–265.

[41] G. Vampa, T. J. Hammond, N. Thiré, B. E. Schmidt, F. Légaré, C. R. McDonald, T. Brabec, and P. B. Corkum, *Linking high harmonics from gases and solids*, *Nature* **522** (June, 2015) 462–464.

[42] G. Ndabashimiye, S. Ghimire, M. Wu, D. A. Browne, K. J. Schafer, M. B. Gaarde, and D. A. Reis, *Solid-state harmonics beyond the atomic limit*, *Nature* **534** (June, 2016) 520–523.

[43] G. Vampa, C. McDonald, G. Orlando, D. Klug, P. Corkum, and T. Brabec, *Theoretical Analysis of High-Harmonic Generation in Solids*, *Physical Review Letters* **113** (Aug., 2014) 073901.

[44] B. Zaks, R. B. Liu, and M. S. Sherwin, *Experimental observation of electron–hole recollisions*, *Nature* **483** (Mar., 2012) 580–583.

[45] H. B. Banks, Q. Wu, D. C. Valovcin, S. Mack, A. C. Gossard, L. Pfeiffer, R.-B. Liu, and M. S. Sherwin, *Dynamical Birefringence: Electron-Hole Recollisions as Probes of Berry Curvature*, *Physical Review X* **7** (Nov., 2017) 041042.

[46] J. B. Costello, S. D. O'Hara, Q. Wu, D. C. Valovcin, L. N. Pfeiffer, K. W. West, and M. S. Sherwin, *Reconstruction of Bloch wavefunctions of holes in a semiconductor*, *Nature* **599** (Nov., 2021) 57–61.

[47] D. C. Valovcin, H. B. Banks, S. Mack, A. C. Gossard, K. West, L. Pfeiffer, and M. S. Sherwin, *Optical frequency combs from high-order sideband generation*, *Optics Express* **26** (Nov., 2018) 29807–29816.

[48] G. Ramian, *The new UCSB free-electron lasers*, *Nuclear Instruments and Methods in Physics Research Section A: Accelerators, Spectrometers, Detectors and Associated Equipment* **318** (July, 1992) 225–229.

[49] I. Vurgaftman, J. R. Meyer, and L. R. Ram-Mohan, *Band parameters for III–V compound semiconductors and their alloys*, *Journal of Applied Physics* **89** (June, 2001) 5815–5875.

[50] P. Lawaetz, *Valence-Band Parameters in Cubic Semiconductors*, *Physical Review B* **4** (Nov., 1971) 3460–3467. Publisher: American Physical Society.

[51] M. S. Skolnick, A. K. Jain, R. A. Stradling, J. Leotin, and J. C. Ousset, *An investigation of the anisotropy of the valence band of GaAs by cyclotron resonance*, *Journal of Physics C: Solid State Physics* **9** (July, 1976) 2809.

[52] Q. Wu and M. S. Sherwin, *Explicit formula for high-order sideband polarization by extreme tailoring of Feynman path integrals*, *Physical Review B* **107** (May, 2023) 174308.

[53] S. D. O'Hara, J. B. Costello, Q. Wu, K. West, L. Pfeiffer, and M. S. Sherwin, *Bloch-Wave Interferometry of Driven Quasiparticles in Bulk GaAs*, May, 2023.

[54] B. Zaks, H. Banks, and M. S. Sherwin, *High-order sideband generation in bulk GaAs*, *Applied Physics Letters* **102** (Jan., 2013) 012104.

[55] M. Borsch, C. P. Schmid, L. Weigl, S. Schlauderer, N. Hofmann, C. Lange, J. T. Steiner, S. W. Koch, R. Huber, and M. Kira, *Super-resolution lightwave tomography of electronic bands in quantum materials*, *Science* **370** (Dec., 2020) 1204–1207.

[56] F. Langer, M. Hohenleutner, C. P. Schmid, C. Poellmann, P. Nagler, T. Korn, C. Schüller, M. S. Sherwin, U. Huttner, J. T. Steiner, S. W. Koch, M. Kira, and R. Huber, *Lightwave-driven quasiparticle collisions on a subcycle timescale*, *Nature* **533** (May, 2016) 225–229.

[57] F. Langer, C. P. Schmid, S. Schlauderer, M. Gmitra, J. Fabian, P. Nagler, C. Schüller, T. Korn, P. G. Hawkins, J. T. Steiner, U. Huttner, S. W. Koch, M. Kira, and R. Huber, *Lightwave valleytronics in a monolayer of tungsten diselenide*, *Nature* **557** (May, 2018) 76–80.

[58] H. Banks, B. Zaks, F. Yang, S. Mack, A. C. Gossard, R. Liu, and M. S. Sherwin, *Terahertz Electron-Hole Recollisions in GaAs/AlGaAs Quantum Wells: Robustness to Scattering by Optical Phonons and Thermal Fluctuations*, *Physical Review Letters* **111** (Dec., 2013) 267402.

[59] C. J. Hwang, *Lifetimes of Free and Bound Excitons in High-Purity GaAs*, *Physical Review B* **8** (July, 1973) 646–652.

[60] P. C. Becker, H. L. Fragnito, C. H. B. Cruz, R. L. Fork, J. E. Cunningham, J. E. Henry, and C. V. Shank, *Femtosecond Photon Echoes from Band-to-Band Transitions in GaAs*, *Physical Review Letters* **61** (Oct., 1988) 1647–1649.

[61] A. V. Gopal, R. Kumar, A. S. Vengurlekar, A. Bosacchi, S. Franchi, and L. N. Pfeiffer, *Photoluminescence study of exciton–optical phonon scattering in bulk GaAs and GaAs quantum wells*, *Journal of Applied Physics* **87** (Feb., 2000) 1858–1862.

[62] S. Rudin, T. L. Reinecke, and B. Segall, *Temperature-dependent exciton linewidths in semiconductors*, *Physical Review B* **42** (Dec., 1990) 11218–11231.

[63] V. L. Alperovich, V. M. Zaletin, A. F. Kravchenko, and A. S. Terekhov, *The influence of phonons and impurities on the broadening of excitonic spectra in gallium arsenide*, *physica status solidi (b)* **77** (1976), no. 2 465–472.

[64] H. Wang, K. Ferrio, D. G. Steel, Y. Z. Hu, R. Binder, and S. W. Koch, *Transient nonlinear optical response from excitation induced dephasing in GaAs*, *Physical Review Letters* **71** (Aug., 1993) 1261–1264.

[65] R. Scholz, *Hole–phonon scattering rates in gallium arsenide*, *Journal of Applied Physics* **77** (Apr., 1995) 3219–3231.

[66] A. V. Gopal, R. Kumar, A. S. Vengurlekar, T. Mélin, F. Laruelle, and B. Etienne, *Exciton-phonon scattering in GaAs/AlAs quantum wires*, *Applied Physics Letters* **74** (Apr., 1999) 2474–2476.

[67] D. Gammon, S. Rudin, T. L. Reinecke, D. S. Katzer, and C. S. Kyono, *Phonon broadening of excitons in GaAs/AlGaAs quantum wells*, *Physical Review B* **51** (June, 1995) 16785–16789.

[68] Y. Zhang, M. D. Sturge, K. Kash, B. P. van der Gaag, A. S. Gozdz, L. T. Florez, and J. P. Harbison, *Temperature dependent time-resolved exciton luminescence in GaAs/AlGaAs quantum wires and dots*, *Superlattices and Microstructures* **17** (Mar., 1995) 201–212.

[69] G. Wang and T.-Y. Du, *Quantum decoherence in high-order harmonic generation from solids*, *Physical Review A* **103** (June, 2021) 063109.

[70] T.-Y. Du and C. Ma, *Temperature-induced dephasing in high-order harmonic generation from solids*, *Physical Review A* **105** (May, 2022) 053125.

[71] N. Sekine, Y. Shimada, and K. Hirakawa, *Dephasing mechanisms of Bloch oscillations in GaAs/Al0.3Ga0.7As superlattices investigated by time-resolved terahertz spectroscopy*, *Applied Physics Letters* **83** (Dec., 2003) 4794–4796.

[72] D. A. Bagrets, I. V. Gornyi, A. D. Mirlin, and D. G. Polyakov, *Relaxation processes in a disordered Luttinger liquid*, *Semiconductors* **42** (Aug., 2008) 994–1007.

[73] D. B. Gutman, Y. Gefen, and A. D. Mirlin, *Nonequilibrium Luttinger Liquid: Zero-Bias Anomaly and Dephasing*, *Physical Review Letters* **101** (Sept., 2008) 126802.

[74] I. V. Gornyi, A. D. Mirlin, and D. G. Polyakov, *Dephasing and Weak Localization in Disordered Luttinger Liquid*, *Physical Review Letters* **95** (July, 2005) 046404.

[75] L. D. Landau and E. Lifshitz, *Theory of Elasticity.* Pergamon Press, New York, 3 ed., 1986.

[76] R.-B. Liu and B.-F. Zhu, *Adiabatic stabilization of excitons in an intense terahertz laser*, *Physical Review B* **66** (July, 2002) 033106. Publisher: American Physical Society.

[77] H. B. Banks, *Electron-Hole Recollisions in Driven Quantum Wells*. PhD Dissertation, University of California Santa Barbara, Santa Barbara, Dec., 2016.

[78] D. C. Valovcin, *High-Order Sideband Generation for Creating Optical Frequency Combs and Probing Bloch Wavefunctions*. PhD Dissertation, University of California Santa Barbara, Santa Barbara, Mar., 2019.